

Arsenic migration and water uptake in multilayer painting systems

Ana Sacristán Civera



Delft University of Technology

MASTER THESIS

Arsenic migration and water uptake in multilayer painting systems

Ana Sacristán Civera

*A thesis submitted in fulfillment of the requirements
for the degree of*

MSc Materials Science and Engineering

Supervisors:

Dr. Yaiza Gonzalez-Garcia	TU Delft
Dr. Katrien Keune	Rijksmuseum
Prof.dr. Joris Dik	TU Delft
Laura-Lynn Fockaert	TU Delft



RIJKS MUSEUM

November 15, 2017

"There is a theory which states that if ever anyone discovers exactly what the Universe is for and why it is here, it will instantly disappear and be replaced by something even more bizarre and inexplicable.

There is another theory which states that this has already happened."

Douglas Adams

Abstract

Orpiment and realgar are yellow and red arsenic sulphide pigments that have been used since antiquity in works of art until the 19th century, when their use was restricted due to their toxicity. With time, these pigments degrade to form colourless arsenic oxide. Different oxidation states of arsenic (+3 and +5) in the degradation products have been recently found. Moreover, they have been identified throughout the whole painting layout from the panel until the varnish, suggesting the migration of degradation products through the paint layers. Besides changing the aspect, they might change the stability of the painting or painted object. Furthermore, they might represent a potential hazard for conservators when dealing with the work of art. Since a painting is in equilibrium with its environment, there is always water in motion inside the painting. It is therefore believed that the degradation products are migrating via water. However, the migration mechanism is still not well understood. This thesis aims to provide a better insight into the diffusion process of arsenites (As^{+3}) and arsenates (As^{+5}) in materials commonly found in paintings. For this, two different approaches were followed:

In one hand, light aged painting reconstructions were analysed with FTIR microscopy and SEM-EDS to assess the effect of different grounds and relative humidity on the migration of arsenic. In all the samples, degradation products were found in the orpiment layer based on the As-O vibration, detected with FTIR microscopy. It was possible to identify arsenic in the ground layer close to the orpiment-ground interface for all samples with both techniques. However, due to the low intensity and the proximity to the interface of the arsenic found in the grounds, no conclusions could be drawn about its migration.

On the other hand, in-situ ATR-FTIR spectroscopy and EIS measurements were performed on a set of samples to analyse the water, arsenates and arsenites diffusion through oil and two varnishes (dammar and mastic). The diffusion coefficients of water in oil, dammar and mastic were determined with both techniques. It was found that the water diffuses faster in oil than in the two varnishes. Despite being similar, mastic was found to be less stable than dammar since a decrease in its barrier properties with time was found. The diffusion of arsenates and arsenites in dammar and mastic was studied by EIS and the diffusion coefficients were calculated for the first time. It was found that the diffusion of arsenites in the coatings is faster than arsenates, which is in accordance to the diffusion of these species in water. EIS resulted in a promising technique in the study of diffusion of ions in coatings. Although further research is needed to fully understand the migration mechanism of arsenic in painting systems, this thesis provides a useful insight and a methodology with which the water and ion transport in coatings can be studied.

Acknowledgements

I would like to thank all of the members of my thesis committee. Firstly to Yaiza González, for your amazing guidance and help. Thank you for always having time for me, encouraging and keeping me going until the end. To Katrien Keune for giving me the incredible opportunity to work in this field, all your help and valuable insights. To Joris Dik for being part of this committee, for your feedback in this thesis and your inspiring lectures. And last but not least, to Laura-Lynn Fockaert for your help in the experimental part of this thesis, for always supporting my ideas and helping me to realize them.

I would like to acknowledge CONACyT for the sponsorship of this master, without which it wouldn't have been possible.

I would like to express my gratitude to Ton Riemslag, Sander van Asperen, Lambert Baij and all the people of the Corrosion Technology and Electrochemistry group, for your valuable help in this thesis. Also to Elise de Boer for making this beautiful cover.

A special thanks to Agnieszka Kooijman. Not only for helping me survive the arsenic and supporting me in the lab but also (as if it was not enough) for your friendship. You made my days in the lab happy and cheerful.

To all my friends from the master and not from the master for making this an extraordinary experience. I wish you all the best and I hope we will meet again. I will miss you!

I would like to thank my wonderful boyfriend Jorge, for sharing this amazing experience with me. Thank you for all your love, patience and support and making me smile every day.

Finally, I would like to thank all my family for staying close despite of the distance. To my mother, father and sister for all your love and support, you are always in my heart.

Contents

1	Introduction	1
1.1	Case studies	2
1.2	Research question and objectives	2
1.3	Thesis outline	3
2	Painting systems	5
2.1	Painting build-up	5
2.2	Ground	6
2.3	Pigment	6
2.3.1	Chalk	7
2.3.2	Lead white	7
2.3.3	Earth pigments	8
2.3.4	Orpiment and realgar	8
2.4	Binder	10
2.4.1	Animal glue	10
2.4.2	Linseed oil	11
2.5	Varnish	12
2.5.1	Mastic and dammar	12
3	Arsenic compounds	17
3.1	Properties of arsenic	17

3.2	Arsenic sulphides	18
3.2.1	Photo-oxidation of realgar	18
3.2.2	Oxidation of orpiment and realgar	19
3.3	Arsenite and arsenate	20
3.3.1	Adsorption reactions	21
3.3.2	Mobility	21
4	Methodology	23
4.1	Ex-Situ experiments	24
4.1.1	FTIR microscopy	24
4.1.2	SEM-EDS	26
4.2	In-situ experiments	27
4.2.1	Materials	27
4.2.2	ATR-FTIR spectroscopy	27
4.2.3	Electrochemical Impedance Spectroscopy	30
5	Results ex-situ	43
5.1	Analysis of the cross-section of orpiment and chalk	44
5.2	Analysis of the cross-section of orpiment and earth ground	48
5.3	Analysis of the cross-section of orpiment and lead white	52
5.4	Discussion	56
6	Results in-situ	57
6.1	Coatings characterization by ATR-FTIR spectroscopy	57
6.2	Water diffusion studied by ATR-FTIR spectroscopy	59
6.2.1	Dammar	63
6.2.2	Mastic	65
6.2.3	Oil	67

6.2.4	Discussion	69
6.3	Water diffusion studied by EIS	71
6.3.1	Dammar	71
6.3.2	Mastic	78
6.3.3	Oil	83
6.3.4	Discussion	87
6.4	Arsenates diffusion studied by ATR-FTIR spectroscopy	88
6.4.1	Aluminium in D ₂ O	88
6.4.2	Aluminium in D ₂ O + Arsenates	89
6.4.3	Aluminium coated with dammar in D ₂ O + Arsenates	90
6.5	Arsenic diffusion studied by EIS	91
6.5.1	Arsenites in dammar	92
6.5.2	Arsenates in dammar	98
6.5.3	Arsenites in mastic	102
6.5.4	Arsenates in mastic	105
6.6	Discussion	109
7	Conclusions and recommendations	115
7.1	Conclusions	115
7.2	Recommendations	116
A	ATR-FTIR spectroscopy D₂O diffusion.	119
B	EIS water diffusion	121

List of Figures

2.1	Typical structure of a painting. A: canvas, B: ground, C: paint, D: varnish [4].	6
2.2	Electromagnetic spectrum showing the visible light region and schematic of selective wavelength absorption [5, 6].	7
2.3	Orpiment and realgar pigments [13, 14].	9
2.4	Orpiment and realgar structures. Arsenic is represented by orange and sulphur by blue.	9
2.5	(a) Glycine, alanine and hydroxyproline and a typical amino acid sequence found in collagen. (b) Collagen network showing the triple helix molecules [15].	11
2.6	(a) Triglyceride composed of black: glycerol, red: linolenic, blue: oleic, green:linoleic acids. (b) Fatty acids found in linseed oil [18].	12
2.7	Polymeric fractions found in (a) mastic and (b) dammar [20].	14
3.1	Structures of the realgar polymorphs. Arsenic is represented by orange and sulphur by blue.	18
3.2	Structures of arsenite and arsenate. Arsenic is represented by orange and sulphur by blue.	20
3.3	E-pH diagram of the As-O-H system at 25 °C and 1 bar [26].	21
4.1	FTIR spectra of hexanoic acid [30].	25
4.2	Main vibrational modes [32].	25
4.3	Schematic representation of electron interactions in SEM [33].	26
4.4	Representation of the evanescent wave in the ATR-FTIR configuration.	28
4.5	ATR-FTIR cell configuration.	29

4.6	Voltage vs current curve showing a range where the relation can be considered linear.	30
4.7	Voltage and current as a function of time showing the phase shift between them [40].	31
4.8	Typical Nyquist and Bode plots of impedance data [39].	33
4.9	Relation between alternating voltage and current across a (a) pure resistance and (b) pure capacitance [40].	34
4.10	Randles equivalent circuit model, Nyquist and Bode plots.	35
4.11	Representation of the double layer formation in the electrode-electrolyte interface.	36
4.12	Nyquist and Bode plots of mass transfer and total impedance for <i>a</i> : semi-infinite, <i>b</i> : transmissive, and <i>c</i> : reflective boundary [39].	38
4.13	Nyquist and Bode plots of a simplified Randles circuit showing the behaviour of a CPE [39].	40
4.14	Electrical cell configuration for EIS experiments.	42
5.1	SEM images of the chalk and orpiment cross-section kept at 43% relative humidity.	45
5.2	Line profile at the interface of orpiment and chalk.	46
5.3	(a): FTIR spectra and (b,c): FTIR microscopy images (red is representative of higher intensity) of the chalk and orpiment cross-section kept at 43% relative humidity for 10 months.	47
5.4	Line profile location and result of the chalk and orpiment cross-section kept at 43% relative humidity for 10 months.	47
5.5	SEM image of the earth ground and orpiment cross-section	48
5.6	SEM images of the earth and orpiment cross-section kept at 43% relative humidity.	49
5.7	Line profiles of arsenic (blue), silicon (pink) and sulphur (green) at the interface of orpiment and the earth ground.	50
5.8	(a): FTIR spectra and (b,c): FTIR microscopy images (red is representative of higher intensity) of the earth and orpiment cross-section kept at 43% relative humidity for 10 months.	51
5.9	Line profile location and result of the earth and orpiment cross-section kept at 43% relative humidity for 10 months.	51

5.10	SEM images of the lead white and orpiment cross-section kept at 43% relative humidity.	53
5.11	Arsenic line profile at the interface of orpiment and lead white.	54
5.12	(a): FTIR spectra; (b,c): FTIR microscopy images (red is representative of higher intensity); and (d): line profile; of the lead white and orpiment cross-section kept at 43% relative humidity.	55
5.13	Line profile location and result of the lead white and orpiment cross-section kept at 43% relative humidity for 10 months.	55
6.1	ATR-FTIR spectra of dammar, mastic, linseed oil, glue and D ₂ O.	58
6.2	Time-resolved ATR-FTIR spectra of dammar, mastic and oil in D ₂ O. The time step for taking the spectra is 30 minutes.	61
6.3	Baseline corrected spectra of dammar, mastic and oil showing the CH ₂ , CH ₃ and D ₂ O peaks.	62
6.4	(a) ATR-FTIR time resolved spectra of dammar in the 2800-2200 cm ⁻¹ region and (b) normalized integrated absorbance of the D ₂ O peak as a function of time.	64
6.5	Concentration profiles of the C=O and D ₂ O peaks in dammar.	64
6.6	(a) ATR-FTIR time resolved spectra of mastic in the 2800-2200 cm ⁻¹ region and (b) normalized integrated absorbance of the D ₂ O peak as a function of time and fitted curves of Fickian diffusion (dotted) and considering a SC (solid).	65
6.7	Concentration profiles of the CO and D ₂ O peaks in mastic.	67
6.8	(a) ATR-FTIR time resolved spectra of Oil in the 2800-2200 cm ⁻¹ region and (b) normalized integrated absorbance of the D ₂ O peak as a function of time and fitted curves of Fickian diffusion (dotted) and considering a SC (solid).	68
6.9	CO peak and concentration profiles of the CO and D ₂ O peaks in oil.	69
6.10	Normalized D ₂ O concentration profiles of dammar, mastic and oil.	70
6.11	EIS plots of dammar at 2, 4, 6, 12 and 24 h in a Na ₂ SO ₄ solution.	72
6.12	Equivalent circuits proposed to fit the EIS data of dammar.	73
6.13	Fitting curve with models A and B to the EIS data of dammar taken at 2h.	74
6.14	High frequency region of the EIS plots of dammar at 2, 4, 6, 12 and 24 h in Na ₂ SO ₄	74

6.15	Plots of the results from fitting the EIS data of dammar as a function of time.	75
6.16	Effective coating capacitance of dammar as a function of time.	77
6.17	Water uptake and fitting curve for the diffusion coefficient calculation of water in Dammar.	78
6.18	EIS plots of mastic at 2, 4, 6, 12 and 24 h in a Na_2SO_4 solution.	79
6.19	Low frequency region of the Bode plots of mastic at 2, 4, 6, 12 and 24 h.	79
6.20	Equivalent circuit proposed to fit the EIS data of mastic.	80
6.21	Fitted curves of the EIS data of mastic taken at 2 and 24 hours with models B and C.	80
6.22	Plots of the results from fitting the EIS data of mastic as a function of time.	81
6.23	Effective coating capacitance and water uptake of mastic.	83
6.24	EIS plots of oil at 2, 4, 6, 12 and 24 h in a Na_2SO_4 solution.	84
6.25	Equivalent circuits proposed to fit the data of mastic.	84
6.26	Fitted curves of the EIS data of oil taken at 2 and 24 hours with model A.	85
6.27	Plots of the results from fitting the EIS data of oil as a function of time.	86
6.28	Water uptake and fitting curve for the diffusion coefficient calculation of water in Oil.	87
6.29	ATR-FTIR spectra and concentration profile of aluminium in D_2O	89
6.30	ATR-FTIR spectra of aluminium in Na_2HAsO_4 and concentration profile of arsenates.	90
6.31	ATR-FTIR spectra of dammar in Na_2HAsO_4	91
6.32	EIS plots of dammar at 2, 4, 6, 12 and 24 h in a NaAsO_2 solution.	92
6.33	Equivalent circuit C proposed to fit the EIS data of dammar in NaAsO_2	94
6.34	Equivalent circuit D proposed to fit the EIS data of dammar in NaAsO_2	94
6.35	EIS data of dammar in NaAsO_2 taken at 4 hours and fitted curve with models C and D.	95
6.36	Nyquist and Bode plot of dammar in NaAsO_2 at 5.5 hours.	98
6.37	EIS plots of dammar at 2, 4, 6, 12 and 24 h in a Na_2HAsO_4 solution.	99

6.38	EIS data of dammar in Na_2HAsO_4 taken at 7 hours and fitted curve with model C.	100
6.39	Nyquist and Bode plot of dammar in Na_2HAsO_4 at 7 hours.	101
6.40	EIS plots of mastic at 2, 4, 6, 12 and 24 h in a NaAsO_2 solution.	103
6.41	EIS data of mastic in NaAsO_2 taken at 4 h and fitted curve with model D simplified.	104
6.42	Calculated CPE_c and R_c of mastic in NaAsO_2	105
6.43	EIS plots of mastic at 2, 4, 6, 12 and 24 h in a Na_2HAsO_4 solution.	106
6.44	EIS data of mastic in Na_2HAsO_4 taken at 4 hours and fitted curve with model C.	106
6.45	EIS plots of mastic at 4 hours in a Na_2HAsO_4 solution.	107
A.1	(a) ATR-FTIR time resolved spectra of Dammar showing the D_2O peak in the 1200 cm^{-1} and (b) normalized integrated absorbance of the D_2O peak as a function of time.	119
A.2	(a) ATR-FTIR time resolved spectra of Oil showing the D_2O peak in the 1200 cm^{-1} and (b) normalized integrated absorbance of the D_2O peak as a function of time and fitted curves of Fickian diffusion (dotted) and considering a SC (solid).	120

List of Tables

1.1	Degradation and migration of orpiment, realgar and emerald green case studies.	2
2.1	Compounds identified in mastic [20].	15
2.2	Compounds identified in dammar [20].	16
3.1	Diffusion coefficients and molar volumes of arsenite and arsenate species in water [28, 29].	22
4.1	Circuit elements commonly used in the models	35
6.1	ATR-FTIR absorption peaks of dammar, mastic, glue and linseed oil. Frequencies are given in wavenumber [cm^{-1}]. ν : Stretching; δ : bending; ω : wagging; τ : twisting; γ : rocking; a: asymmetric.	59
6.2	Diffusion coefficients of D_2O calculated for dammar, mastic and oil.	70
6.3	Selected EIS data of dammar calculated with Model B.	75
6.4	Selected EIS data of mastic calculated with Model C.	81
6.5	Selected EIS data of oil calculated with Model A.	85
6.6	Selected EIS data of oil calculated with Model A.	88
6.7	Fitted parameters of the EIS data of dammar in NaAsO_2 taken at 5.5 hours calculated with Model D.	95
6.8	Calculated Warburg coefficients and diffusion coefficients of arsenites in dammar.	98
6.9	Fitted parameters of the EIS data of dammar in Na_2HAsO_4 taken at 7 hours calculated with Model C.	100

6.10	Calculated Warburg coefficients and diffusion coefficients of arsenates in dammar.	102
6.11	Fitted parameters of the EIS data of mastic in NaAsO_2 taken at 4 hours calculated with Model D.	104
6.12	Fitted parameters of the EIS data of mastic in Na_2HAsO_4 taken at 4 hours calculated with Model C.	107
6.13	Calculated Warburg coefficients and diffusion coefficients of arsenates in dammar.	108
6.14	Calculated water diffusion coefficients for dammar, mastic and oil. . . .	109
6.15	Calculated arsenite and arsenate diffusion coefficients for dammar and mastic in $\text{cm}^2 \text{s}^{-1}$	111
B.1	EIS data of water diffusion in Dammar.	122
B.2	EIS data of water diffusion in Mastic.	123
B.3	EIS data of water diffusion in Oil.	124

Chapter 1

Introduction

Orpiment and realgar are yellow and red arsenic sulphide pigments that have been used since antiquity in works of art such as paintings and furniture until the 19th century, when their use was restricted due to their toxicity. As any other pigment, orpiment and realgar degrade with time. Several case studies have been analysed in which degradation products have been identified. The degradation involves an oxidation reaction of the arsenic sulphides to form colourless arsenic oxide. Moreover, arsenic species with oxidation states of 5+ (arsenates) and 3+ (arsenites) have been found not only in the orpiment and realgar paint layers, but also in other paint layers, from the panel up until the varnish.

A painting is always in equilibrium with the surrounding environment, which means that there is always water, oxygen and other compounds in motion inside a painting. Therefore, it is believed that the arsenic is migrating via water throughout the paint layers [1, 2]. However, the mechanism behind the arsenic oxidation and transport inside the paintings is not well understood.

The degradation and migration of these pigments is important since it has a direct effect on the aspect of the painting or the painted object making it look dirty and whitish. Moreover, the degradation products can change the stability of the painting as new reactants are being produced. This could lead to changes of other components of the painting or painted object and worsen its state. Therefore, it is of great importance to understand the degradation and migration process to be able to design a solution and to try to stop and reverse it.

Furthermore, arsenic migration is a potential hazard for the conservators. The removal of old varnishes is a common practice in the conservation of paintings and, since arsenic has been identified even in the varnish layer, it can represent a potential risk to the conservator's health. It is for these reasons that the degradation and migration of orpiment and realgar are the subjects of this thesis.

1.1 Case studies

A summary of the objects previously studied is presented in [Table 1.1](#). The case studies include paintings and furniture. The pigments studied are orpiment, realgar and emerald green, which is also an arsenic containing pigment composed of copper acetoarsenite. Similar to orpiment and realgar, it was used until 19th century and discontinued due to its toxicity. The degradation products of this pigment are also arsenite and arsenate.

Table 1.1: Degradation and migration of orpiment, realgar and emerald green case studies.

Sample	Artist	Year	Pigment	Ref.
The dentist	Unknown	17th century	Orpiment, realgar	[1]
Cupboard Hl. Theresa		1824	Emerald green	[1]
Interior of a restaurant	Vincent Van Gogh	1887	Emerald green	[1]
Festoon of fruits and flowers	Jan Davidsz. de Heem	1660–1670	Orpiment	[1]
Descent of the cattle	Théodore Rousseau	1836	Emerald green	[1]
Saybrook chest	Charles Willam	1710–1727	Orpiment	[2]
Still life with five apricots	Adriaen Coorte	1704	Orpiment, realgar	[2]

As mentioned above arsenites and arsenates have been found all across the painting build-up. Moreover, it has been found that it is only arsenic compounds and not sulphur that are found throughout the layers. This suggests that the degradation products are the ones migrating, and not the original pigment.

An interesting observation made in the sample *Festoon of fruits and flowers* is that arsenic was concentrated in lead rich areas. Even the presence of As-Pb needles was observed. This is an indication of the affinity of arsenic towards lead and therefore, pigments such as lead white will have a important effect on the migration of arsenic compounds. This same trend was observed in the Saybrook chest.

Another important finding is that more oxidized products (arsenates) were found further away from the intact particle than less oxidized products, such as arsenites. However, the oxidation of the original pigments and the migration of its degradation products inside the painting is not well understood. The aim of this thesis is therefore to gain more insight into the mechanisms of this phenomena. The proposed main research question and particular objectives are presented in the next section.

1.2 Research question and objectives

The main research question is: How do the orpiment and realgar degradation products, namely arsenites and arsenates, migrate throughout the painting layers?

In order to answer the research question, the following particular objectives were proposed:

- Analyse the effect of different grounds in the oxidation of orpiment and in the mobility of the degradation species with different imaging techniques.
- Study the diffusion of water through binders and varnishes commonly used in paintings.
- Determine the diffusion coefficients of arsenites and arsenates in the binders and varnishes and compare them.
- Study the application of ATR-FTIR spectroscopy and EIS to the analysis of the previously mentioned phenomenons.

1.3 Thesis outline

This thesis contains 7 chapters. An overview of the content of each chapter is given below.

Chapter 2 describes how a painting looks like in terms of its materials. Firstly, a typical build-up of a painting is given in order to provide a general understanding of the system under study. And secondly, the materials used in this thesis, namely pigments, grounds, varnishes and binders are introduced.

Chapter 3 provides an overview of the arsenic chemistry, which includes the degradation reactions of orpiment and realgar, the absorption reactions of arsenite and arsenate in amorphous oxides and the mobility of this species in water.

Chapter 4 explains the proposed methodology. It is conformed by two parts: ex-situ measurements, in which cross-sections of painting reconstructions are studied by SEM-EDS, FTIR microscopy and in-situ measurements, where the diffusion of water and arsenic is studied by ATR-FTIR spectroscopy and electrochemical impedance spectroscopy. The principles of the techniques is given, as well as the experimental set up and the methods used to calculate the desired parameters.

Chapter 5 contains the results from the ex-situ measurements. It consists in three parts that belong to the three analysed grounds: chalk, earth pigment and lead white. Lastly, a discussion of the findings is presented.

Chapter 6 presents the results of the in-situ measurements in 6 different sections. First, the characterization of the dammar, mastic, glue and oil coatings by ATR-FTIR spectroscopy is given. The second and third parts contain the water diffusion results studied by ATR-FTIR spectroscopy and EIS, respectively. In the fourth and fifth parts, the results of the arsenic diffusion with the above mentioned techniques are presented. And lastly, a discussion of the results can be read in the sixth section.

Chapter finally states the final conclusions drawn from the experiments made in this thesis along with recommendations for future work.

Chapter 2

Painting systems

In this chapter, a brief introduction of the materials that constitute a painting is given. First, a typical structure of a painting is described. The general characteristics of the painting components (ground, pigment, binder and varnish) are individually given and a description of the materials used in this thesis is provided.

2.1 Painting build-up

A painting is a very complex system that is conformed by multiple layers and each layer has a wide variety of materials. The typical structure of a painting is presented in Fig. 2.1. The surface where the paint is applied is called *support*. It can be made of a rigid material like wood, metal, glass or plastic; or by a flexible material like a cotton or linen canvas stretched over a wooden frame. The canvas is covered by a diluted glue, called a *size*, to prevent the subsequent layers to be absorbed on the support and avoid the penetration of binders and vehicles that could affect the support material. In order to enhance this protection and create a reflective surface beneath the paint film, a *ground*, that consist normally in a glue, chalk and white pigment, is applied on top. Above the ground, several layers of paint are applied. The paint consists of a powdered material, *pigment*, which provides the colour dispersed in a liquid called *binder* that helps the paint to be spread out and keeps the individual pigment grains together and attached to the surface producing a stable paint film upon drying. The binder can be oil, egg, gum or a synthetic polymer. Sometimes, a *vehicle* is added to the paint to facilitate the application, make it more transparent and aid the drying of the film. The vehicle can be water, gums, acrylic polymers, turpentine or petroleum derivatives and they evaporate as the paint dries. Finally, a layer of *varnish* can be placed on top to protect the painting from pollutants, dirt, and moisture and to change the final appearance of the painting by making it more reflective [3].

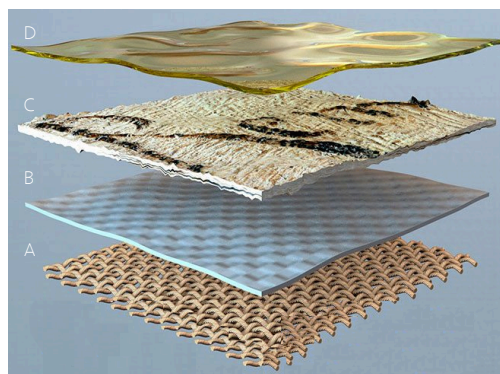


Fig. 2.1: Typical structure of a painting. A: canvas, B: ground, C: paint, D: varnish [4].

2.2 Ground

The ground is a thick coating that is applied to the the sized support. It prevents the penetration of binders and vehicles to the support and acts as a reflective surface as light penetrates through the paint as far as the ground. Traditionally for wooden panels and canvas, a mixture of animal glue and gypsum called *gesso* was used. From the renaissance, a hard gesso containing a mixture between animal glue, chalk (CaCO_3) and sometimes a white pigment (normally lead white) has been used used, although some artists add colour to create a base for subsequent colours. Nowadays the animal glue of traditional gesso is being replaced by an acrylic polymer. The most used pigment for building the ground is lead white, which brings luminosity to the following paint layers, although other colours are often used [3]. Besides protection, the ground is used to prepare the surface of the support and create a smooth, uniform and non porous surface to paint.

In this thesis, chalk, lead white and an earth pigment were studied as the grounds in the painting reconstructions for the ex-situ experiments. These are presented in the following section as they are pigments.

2.3 Pigment

A pigment is a fine powder that brings the colour to the paint and is dispersed in a liquid (binder). The colour of a pigment is produced by the selective absorption of wavelengths of visible light. Visible light comprises a range of the electromagnetic spectrum that the eye responds to by sensing different wavelength as different colours (Fig. 2.2a). A colour of a material will be given by the wavelengths that are not absorbed, but reflected. For example, a green object will absorb all wavelengths except those corresponding to green light Fig. 2.2b. Therefore, a pigment is a substance that absorbs a certain part of the electromagnetic spectrum providing colour [3].

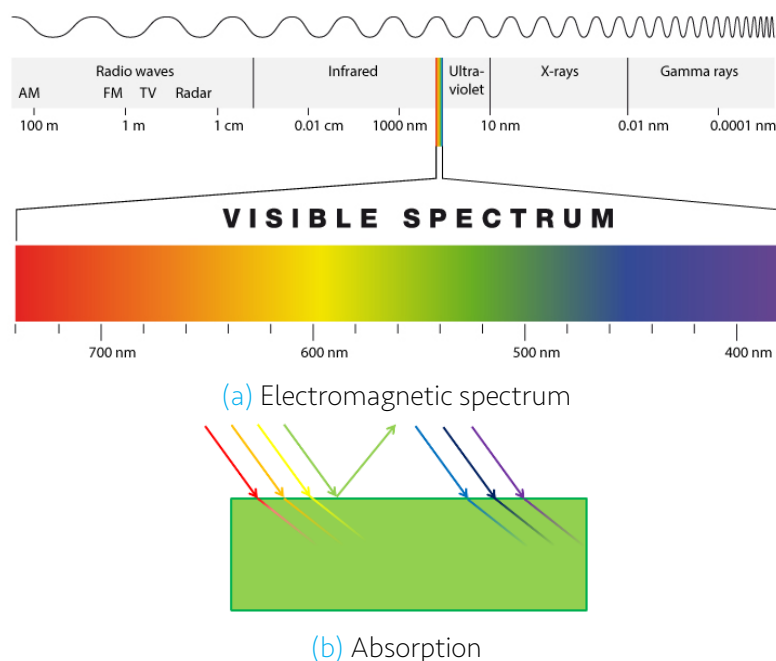


Fig. 2.2: Electromagnetic spectrum showing the visible light region and schematic of selective wavelength absorption [5, 6].

A pigment can be natural, from different sources of animals, plants or minerals, or synthetic. It is grounded as a fine powder and dispersed in a liquid to allow its application in the painting. Throughout history, the usage of different pigments has changed for several reasons such as availability, toxicity, or the finding or development of other pigments. Only the pigments studied in this thesis, namely chalk, lead white, earth, orpiment and realgar, are described in the following sections.

2.3.1 Chalk

Chalk is a white porous material composed of calcite, which is the most crystalline form of calcium carbonate CaCO_3 . Chalk occurs naturally in thick beds in many parts of the world and is formed from marine sediments that consist of skeletal remains of prehistoric invertebrate animals. It has been used as a white pigment since antiquity and is still in use. However, it has a poor covering quality when mixed with oil. Other uses include the production of lime and portland cement and as a pigment in ceramics, cosmetics, paper and paints. The mixture of chalk and glue is the most common ground in Northern European paintings from medieval times to the 18th century [7].

2.3.2 Lead white

The term lead white constitutes any lead-based pigment. However, it generally refers to basic lead carbonate [8]. It is one of the most important and used pigments of all times

and it has been used since antiquity until the 19th century, when its production was restricted due to its toxicity. It was preferred among artists because it can be applied in a very thin layer due to its high density and high degree of opacity. Another pigment, zinc white, was used as an attempt to replace it, but it could not match the great covering ability of lead white. It was not until 1921 when titanium white, which has a similar covering ability, began to be produced that lead white usage was substantially diminished. Chemically, it is a basic lead carbonate with formula $2\text{PbCO}_3 \cdot \text{Pb}(\text{OH})_2$. It has been used in combination with a wide variety of binders like water, linseed oil, animal glue, and tempera [9, 10].

2.3.3 Earth pigments

The earth pigments are a group of silicon and aluminium based minerals that contain oxides, principally of iron and magnesium, and are found throughout the world. They can be classified as:

- Ochres: the major components are iron oxide and clay. Their colour goes from yellow, produced by hydrated iron oxide, to red, given by anhydrous iron oxide. They are very durable and inert.
- Siennas: this pigments, named after the Italian city of Sienna, differ from the others because they contain minor amounts (approximately 5%) of manganese oxide. Their colour is yellow-brown and it forms a transparent paint that is used as a glaze.
- Umbers: this brown pigments contain iron hydroxide and between 5 and 20% manganese oxide. The name comes from the deposits found near the Italian city of Umbria, although it is also found in Turkey and Cyprus. They have a good hiding power and are used in oil and watercolour paints and in lithographic inks and wallpaper.
- Green earths: they are also called terre verte. This pigments due their green colour to the clay minerals celadonite and glauconite. They are stable and compatible with all media. With oil they form a translucent paint with a low hiding power.

These minerals have been used as pigments since ancient times throughout the world. They are used as such or modified by roasting the pigments to highlight the red colour. These roasted pigments are called burnt umber, burnt sienna, etc. [7, 8].

2.3.4 Orpiment and realgar

Orpiment and realgar are two natural occurring arsenic sulphide minerals that along with arsenopyrite, form the world's arsenic source. They have been used as pigments since ancient Egypt until the 19th century. They have been identified in egyptian objects

from the 31st century BC, indian paintings, asian wall paintings, norwegian folk art objects and 18th century American oil paintings, among others. Orpiment was not very common in European works of art but it was used from The Book of Kells (9th century) until the late 19th century impressionist paintings. It also appears in works from Jan Van Eyck (15th century) and Tintoretto (16th century) [11]. However, these pigments are highly toxic. In general, arsenic salts can cause bladder, skin, lungs and kidney cancer when ingested or inhaled [12]. For this reason, orpiment and realgar were replaced by other pigments such as cadmium and chrome yellow in the 19th century [2]. The pigments are presented in Fig. 2.3

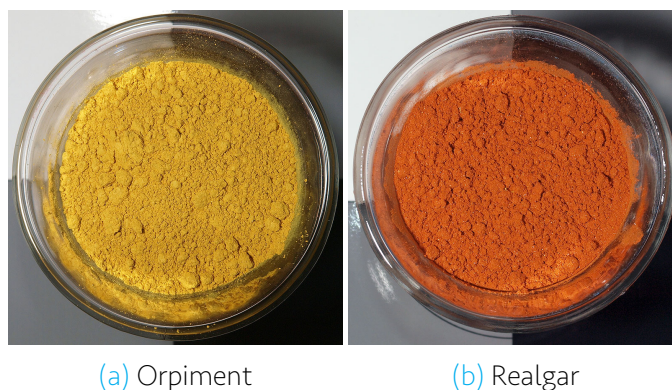


Fig. 2.3: Orpiment and realgar pigments [13, 14].

Orpiment is a yellow arsenic sulphide (As_2S_3) and realgar is a red arsenic sulphide (As_4S_4) and they can be found in natural or artificial form. Both orpiment and realgar have a monoclinic structure. However, they have different arrangements. In one hand, orpiment consists of covalently bonded $[\text{As-S}_3]$ chain units connected by sulphur atoms and held together by van der Waals forces. In the other hand, realgar (or α -realgar, which is the stable polymorph at room temperature) has cage-like units of $[\text{As}_4\text{S}_4]$, also connected by van der Waals forces. In this structure, arsenic atoms form a tetrahedron and the sulphur atoms form a square bisecting one of the tetrahedron axes [12]. Their correspondent structures are shown in Fig. 2.4.

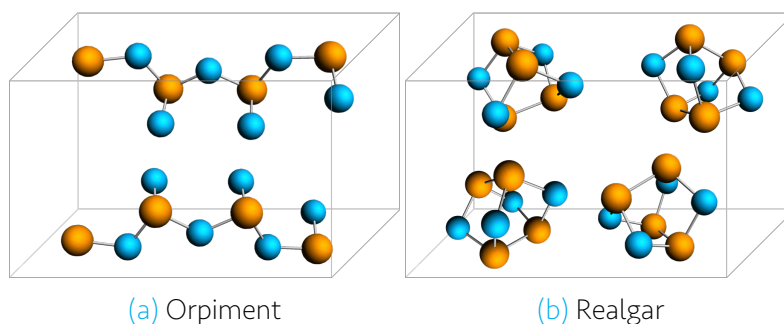


Fig. 2.4: Orpiment and realgar structures. Arsenic is represented by orange and sulphur by blue.

As many other pigments, orpiment and realgar degrade with time. There are two main oxidation reactions. The first one is a photo-oxidation only suffered by realgar that results in a transformation of its structure to form para-realgar, producing a yellow product that can be further oxidized to colourless arsenolite (As_2O_3). The second one, which is the process studied in this thesis, is an oxidation that involves a change in the oxidation state (from As^{3+} to As^{5+}) and occurs in both pigments [2]. The mechanisms of both processes are described in [Chapter 3](#).

2.4 Binder

A binder is a substance that together with the pigment, conforms the paint. It is necessary to keep the pigment particles together and adhered to the substrate. The binders can be either natural or synthetic and can be classified as soluble or insoluble in water. Another classification based on by their composition is as carbohydrate-containing binders, such as honey and plant gums; protein-containing binders like animal glues and egg white; and others that do not fall in these two categories such as oils, beeswax and natural resins.

2.4.1 Animal glue

Animal glue is an adhesive material made of protein. It results from breaking down and dissolving collagen by boiling connective tissues or bone from animals such as fish, goats, sheep, goats, horses, etc. It has the particularity that is soluble in hot water and tends to form a gel upon cooling. The gel goes back into solution when it is reheated. As water evaporates out of the gel, the glue becomes a stiff and glassy solid [3]. It is highly hygroscopic, it contains between 12-16% water at 50% relative humidity (RH) and 30% water at 84% RH at room temperature and becomes more flexible as it absorbs more water [15]. It has been used since ancient Egypt and is the most widely binding media in the world. It is used as a size in paper, in paint, textiles, manuscripts, furniture, etc.

Collagen is conformed by amino acids polymerized in a triple helix arrangement ([Fig. 2.5b](#)). The helix-shaped molecules are formed by over 1000 monomers and are packed together through hydrogen bonds [15]. The density of glue is 1.27 g cm^{-3} and its refractive index between 1.516 and 1.534 [7].

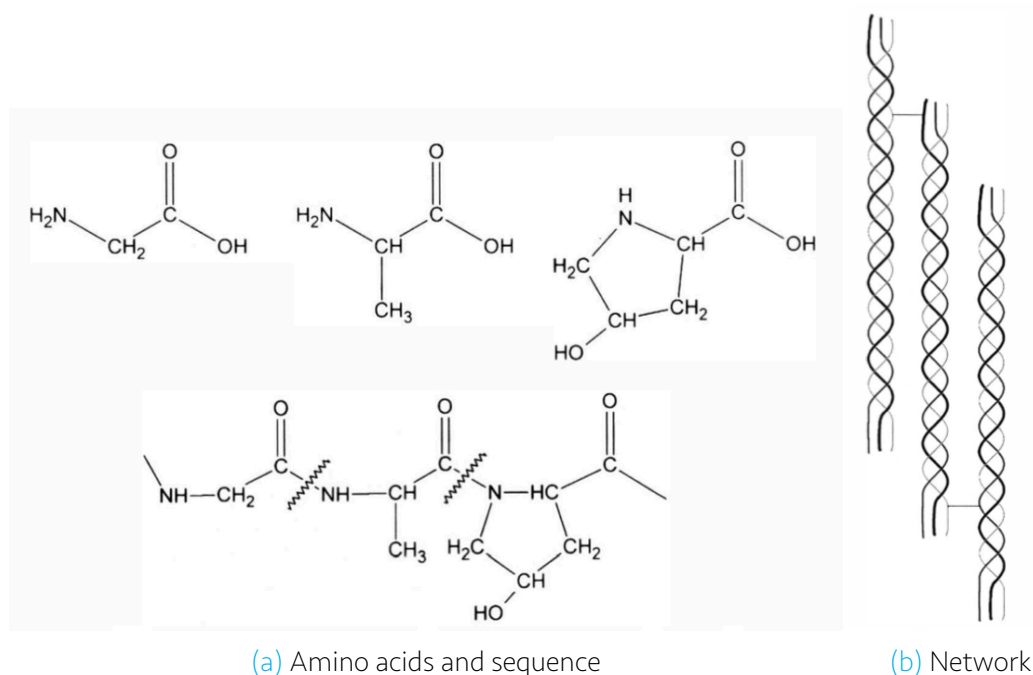


Fig. 2.5: (a) Glycine, alanine and hydroxyproline and a typical amino acid sequence found in collagen. (b) Collagen network showing the triple helix molecules [15].

2.4.2 Linseed oil

Linseed oil is one of the most common oils used in paintings as a binder and in varnishes since the 15th century until today. It is obtained from the seeds of the flax plant and it forms a hard, insoluble film when it dries. The importance of linseed oil in painting lies in its capacity to form a thin film when it dries that has good optical and mechanical properties and it dries relatively fast.

The oils are formed by triglycerides, which are esters made from one molecule of glycerol and three fatty acids (Fig. 2.6a). The fatty acids found in linseed oil are linolenic acid (48-60%), oleic acid (14-24%), linoleic acid (14-19%), palmitic acid (6-7%), and stearic acid (3-6%). Their structures are presented in Fig. 2.6b. It is a drying oil, which means that it dries by a chemical reaction called *autoxidation* and not by the evaporation of a solvent like the non-drying oils. The drying, or curing mechanism involves an exothermic reaction between an oxygen and one of the carbons adjacent to a double bond of a fatty acid to form a *hydroperoxide*. These hydroperoxides then react with another oil molecule to form an intra-molecular linkage. This is called *cross-linking* and it leads to the formation of a network that results in a solid film [16, 17].

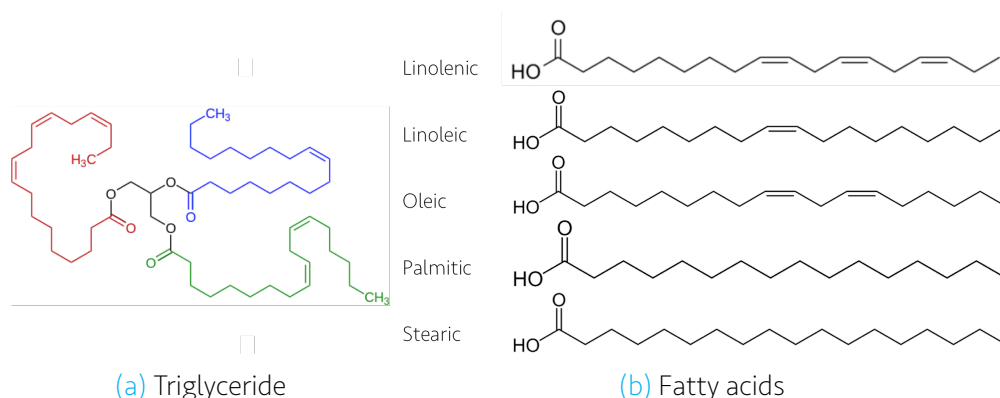


Fig. 2.6: (a) Triglyceride composed of black: glycerol, red: linolenic, blue: oleic, green: linoleic acids. (b) Fatty acids found in linseed oil [18].

In certain occasions, the cross-linking reaction does not take place completely and leads to the formation of low molecular weight degradation products like aldehydes that can be further oxidized to form carboxylic acids. This oxidation reaction can also take place after hardening, although the process is slow and takes long ageing times [17].

2.5 Varnish

A varnish is a material composed of a resin dissolved in a liquid that forms a hard glassy film upon drying. It is used as a coating applied over the paint layers. Besides protecting the painting from light, pollutants and dust it gives a uniform surface to the painting and enhances the optical properties, such as gloss, contrast and color saturation. The resin can be either dissolved in oil, called an *oil varnish*, or in turpentine or ethanol, called a *spirit varnish*. The resins can be either natural, such as dammar, mastic, shellac and sandarac, or synthetic like acrylic or alkyd resins [7]. In this thesis, the two most commonly used varnishes in painting, mastic and dammar, were studied and will be introduced in the next sections.

2.5.1 Mastic and dammar

Mastic and dammar are the two most commonly used varnishes in the 19th and 20th centuries in painting. They are classified as low molecular weight varnishes and are composed of a complex mixture of compounds, mostly triterpenoids. A triterpene is a compound that is formed by C₃₀ molecules containing ring systems and a number of functional groups. Their advantage against other varnishes is that they are less yellowing when applied and more soluble, hence a thin film is easier to apply and the decoloration is not very serious. Their disadvantages are that apart from yellowing, dammar and mastic become brittle when dried and can craze and become matt [16].

Mastic is obtained from the *Pistacia* tree of the *Anacardiaceae* family, which grows in the coasts of the Mediterranean mainly in the greek island of Chios. It has been used since antiquity as an oil varnish and since the 17th century as a spirit varnish diluted with turpentine, until dammar was introduced in the 19th century. It is also used as chewing gum and a flavouring agent in a liquor called mastica.

Dammar is obtained from the trees of the family *Dipterocarpaceae* from southeast Asia. It was introduced as a picture varnish in 1826 and been used extensively. Due to its optical qualities and resistance to yellowing, it has replaced mastic [19]. Nowadays, its principal use is as a spirit varnish for paintings. However, its use has declined because of the production of synthetic materials. It is also used in painting inks and as coatings for papers and textiles [7]. The role of dammar as a varnish for conservation treatment of oil paintings has been important. It is still considered a good option and fairly used by middle European conservators [19].

Mastic and dammar have similar properties. Their density is 1.074 g cm⁻³ for mastic and 1.04 to 1.12 g cm⁻³ for dammar. Their refractive index is 1.535-1.536 for mastic and 1.515-1.539 for dammar. They are both insoluble in water and soluble in turpentine, oil and chloroform. While mastic is soluble in alcohol, dammar has an insoluble polymeric fraction which makes it only slightly soluble [7]. Another difference is the lower polarity of dammar compared to mastic [19].

In chemical composition, both varnishes share some compounds. The chemical compounds in dammar have been found quite constant no matter the source, only the proportions is what changes, contrary to mastic where its components are more varied.

As mentioned above, these varnishes are formed by a complex mixture that consist mainly in triterpenoid compounds. These triterpenoids tend to form a flat sheet-like structure connected by van der Waals interactions creating weak cross-links. The triterpenoids found in mastic are presented in Table 2.1, while those encountered in dammar are presented in Table 2.2 [20]. Besides the triterpenoid compounds, both materials have a polymeric fraction. In mastic, it has been identified as cis-1,4-poly- β -myrcene (Fig. 2.7a) and in dammar as policadyene (Fig. 2.7b). The polimeric fraction in fresh dammar has been found to be compose between 10 and 16% of the total mass [15]. Additionally, dammar contains a fraction of sesquiterpenoid (C15) compounds and in mastic, approximately 2% of essential oil has been found as well as bicyclic and tricyclic triterpenoids. Even in fresh dammar and mastic, the compounds are oxidized to some degree. Up to 6 oxygens have been found to be incorporated to the initial components [20].

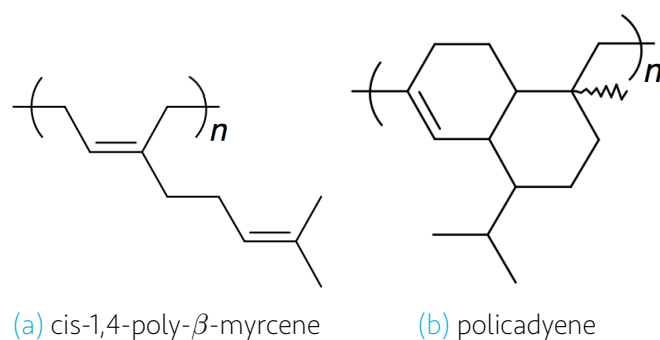


Fig. 2.7: Polymeric fractions found in (a) mastic and (b) dammar [20].

The degradation of these varnishes involves a photo-oxidation of the triterpenoid fraction. This increases the abundance of polar groups, which makes the varnish more hydrophilic because of the presence of hydroxyl groups (-OH) and increases the acidity since carboxylic groups (-COOH) are formed. At the same time, this increases the dipolar and hydrogen bonding interactions making the varnish stiffer and more brittle with a higher degree of cross-linking.

Table 2.1: Compounds identified in mastic [20].

Name	R1	R2	Structure	Name	R1	R2	Structure
Masticdienonic acid	O			Tirucallol			
Isomasticdienonic acid	O						
Masticdienonic acid	OH, H						
3-epi-isoasticdienonic acid	OH, H						
3-O-acetyl-2-epi-masticdienonic acid	CH3COO						
3-O-acetyl-2-epi-isomasticdienonic acid	CH3COO						
beta-amyrin	OH, H	CH3		nor-lupeone	O	H	
beta-amyrone	O	CH3		lupeol	OH, H	CH3	
nor-beta-amyrin	OH, H	H					
nor-beta-amyrone	O	H					
nor-olean-17-en-3-one	O	H					
28-hydroxy-beta-amyrone	O	OH					
Eleagnonic aldehyde	O	CHO		(3L,8R)-3,8-dihydroxypoly	OH, H		
Oleanonic acid	OH, H	COOH		poda-13E,17E,21-triene			
Oleanonic acid	O	COOH		(3R)-3-oxo-8-hydroxypoly	O		
18alphaH-oleanonic acid	O	COOH		poda-13E,17E,21-triene			
Oleanonic acid	-	-					
Germanicol	OH, H	CH3					
Moronic acid	O	COOH		3-hydroxy-malabarica	OH, H		
Dammaradienone				-14(26),17E,21-triene			
Hydroxydammarone	O			3-oxo-malabarica	O		
3-acetoxy-hydroxydammarone	CH3COO			-14(26),17E,21-triene			

Table 2.2: Compounds identified in dammar [20].

Name	R ₁	Structure
Dammaradienol Dammaradienone	OH, H O	
Dammarenolic acid	-	
Hydroxydammarenone Dammarenediol	O OH, H	
Shoreic acid and eichlerianic acid	-	
Hydroxyhopanone 3-acetoxy-22-hydroxy-hopanone	O CH ₃ COO	
Hydroxyoleanonic lactone	-	
23-hydroxy-2,3-seco-12-ene -2,3,28-trioic acid (2→23)-lactone	-	
Asiatic acid	-	

Chapter 3

Arsenic compounds

In this chapter, an introduction to the properties and chemistry of arsenic and arsenic compounds is presented. First, general properties of arsenic are described. Secondly, the oxidation reactions of the sulphide minerals are shown, which are those suffered by the orpiment and realgar pigments. The last section refers to arsenites and arsenates in solution. In this section, their adsorption reaction in aluminium oxide is introduced, which is the basis of the in-situ experiments performed to measure the diffusion of these species in the varnishes and binders, and lastly their mobility in water is described.

3.1 Properties of arsenic

Arsenic (As) is a chemical element that belongs to the metalloid group. It is mostly found in nature in minerals in combination with sulphur and metals, although it is also present as pure crystals. It has been used since ancient times in several applications. It has been used in metallurgy for decoration and pigmentation, in fireworks and warfare. One of the most famous uses of arsenic oxide (As_2O_3) is as a poison, "the poison of kings", since it is odourless, tasteless and lethal in small doses and was mostly used by the ruling class. In the other hand, it was used for curative purposes to treat syphilis and cancer and is still used to treat leukaemia. It has also been used in agriculture as a insecticide and in wood as a preservative since it is toxic to insects, bacteria and fungi [21, 12].

The toxicity of arsenic is due to its affinity to dithiol groups $(\text{SH})_2$ which interferes with enzymatic activity. Long exposures may cause dome forms of cancer such as skin, bladder, lung and kidney. The greatest arsenic exposure threat for humans is in drinking water. Therefore, much effort has been made to understand the chemistry of arsenic with the finality of removing it from soils and water [21].

Arsenic is found in the periodic table in group V in the third row and its atomic number is 33. Its electronic configuration is $[\text{Ar}]4s^2 3d^{10} 4p^3$, which provides 5 valence electrons to form a bond and empty p orbitals for electron occupation. As a consequence, it can form

compounds with oxidation states from +5 to -3, but is predominantly found as As^{+3} and As^{+5} and it is mainly found in nature bounded to oxygen and sulphur. The compounds formed in solution are arsenites, with an oxidation state of +3, and arsenates with an oxidation state of +5.

3.2 Arsenic sulphides

Arsenopyrite (FeAsS), orpiment (As_2S_3) and realgar (As_4S_4) are the most common arsenic sulphide minerals. Arsenic bonds to sulphur in a covalent way and it forms arrangements together with As-As bonds. A description of orpiment and realgar can be found in [Section 2.3.4](#). The most common reactions suffered by these minerals are the photo-oxidation of realgar and the oxidation of orpiment and realgar. These reactions are presented in the following section.

3.2.1 Photo-oxidation of realgar

When exposed to light, α -realgar degrades into a friable, yellow film. In the past, this yellow product was mistakenly identified as orpiment, since the two pigments are often found together. However, recent studies have demonstrated that it is the polymorph para-realgar [22]. The transformation to para-realgar occurs when the pigment is exposed to light at wavelengths of 500-670nm. A molecule of As_4S_4 incorporates a sulphur atom into its structure forming As_4S_5 , called the χ -phase. Subsequently, the χ -phase is transformed into a larger As_4S_4 para-realgar molecule by releasing a sulphur atom, which is re-attached to another realgar molecule. The resulting para-realgar molecule has the same chemical formula as realgar but with a different structure ([Fig. 3.1](#)).

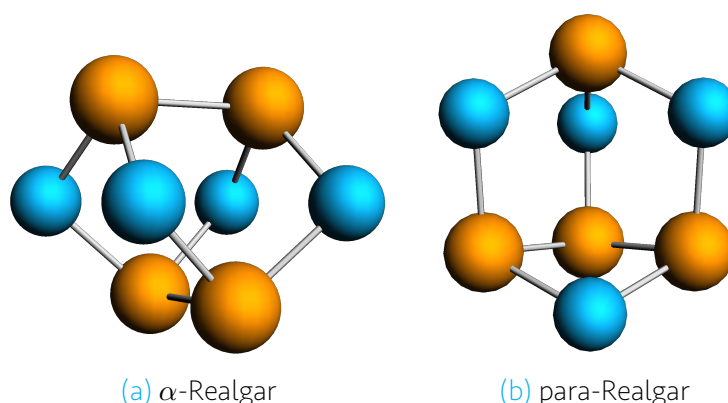


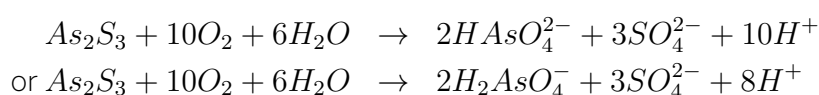
Fig. 3.1: Structures of the realgar polymorphs. Arsenic is represented by orange and sulphur by blue.

Within the α -realgar molecule, the four arsenic atoms are in equivalent environments: they are covalently bonded to two sulphur atoms and another arsenic atom. The photo-oxidation produces a new arrangement of the atoms in para-realgar. Now there are three different environments for the four arsenic atoms: the first As atom is bonded to three S atoms, the second has one As-S bond and two As-As bonds and the third and fourth (two equivalent arsenic atoms) have two As-S bonds and one As-As bond. Moreover, there is an anisotropic unit cell expansion (from 802 to 810 Å) resulting in a loss in crystallinity [23]. The para-realgar molecule can be further oxidized to produce arsenic oxide (As_2O_3), which is white. Therefore, the transformation of realgar to para-realgar and further to arsenic oxide imply a colour change, which changes the aspect of the painting or painted object and may have detrimental effects in the painting since it is accompanied with a volume expansion and by the release of secondary reaction products.

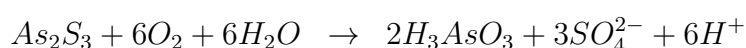
3.2.2 Oxidation of orpiment and realgar

Contrarily to the photo-oxidation, which only applies to realgar, this other kind of degradation occurs in both realgar and orpiment. It consists of an oxidation reaction of the arsenic sulphides with water and oxygen to form aqueous arsenites and arsenates.

The oxidation of natural orpiment was studied by Lengke et al in the pH range from 6.8 to 8.2 [24]. They found that the oxidation rate of orpiment increases with pH and oxygen content and that an exothermic reaction is produced. The products of the reaction are the oxyanions arsenite and arsenate, whose properties are introduced in the next section. They proposed the following reactions:



The products of the reaction are arsenates, that depending on the pH will be mono- or di-protonated, and sulphates. Also, the reaction produces H^+ , thus acidifying the medium. Furthermore, they found that the oxidation reaction does not proceed to completion but there is a competitive dissolution reaction where arsenites and sulphates are formed:



Therefore, the product of the reaction is a mixture between arsenites (H_3AsO_3) and arsenates ($HAsO_4^{2-}$ or $H_2AsO_4^-$ depending in the pH) whose ratio of As(III)/As(V) varies between 1.1 to 2.2 depending on the pH and oxygen content conditions. Sulphates and

H^+ are produced in both reactions, which indicates that there is an acidification the medium.

In a review made by Sadiq et al, a compendium of equilibrium constants of arsenic compounds reactions is presented [25]. Those of interest for this thesis are:

Reaction	logK
$As_2S_3 + 16H_2O \rightarrow 2HAsO_4^{2-} + 2SO_4^{2-} + 22e^- + 23H^+$	-180.42
$As_4S_4 + 8H_2O \rightarrow HAsO_4^{2-} + SO_4^{2-} + 11e^- + 15H^+$	-83.13

With the above information, it is clear that the orpiment oxidation gives rise to the formation of both arsenites and arsenates. The proportion between them will be specific of the conditions of the surroundings. Also, sulphates are produced as a by-product of the reaction. As seen from the equilibrium constants, the oxidation of orpiment is less favoured than that of realgar (the equilibrium constant is higher), which indicates that orpiment is thermodynamically more stable than realgar.

3.3 Arsenite and arsenate

In solution, arsenic exist as oxyanionic acids, mainly as arsenites, with a oxidation state of 3+ and as arsenates with a oxidation state of 5+. The structures of arsenite and arsenate are presented in Fig. 3.2.

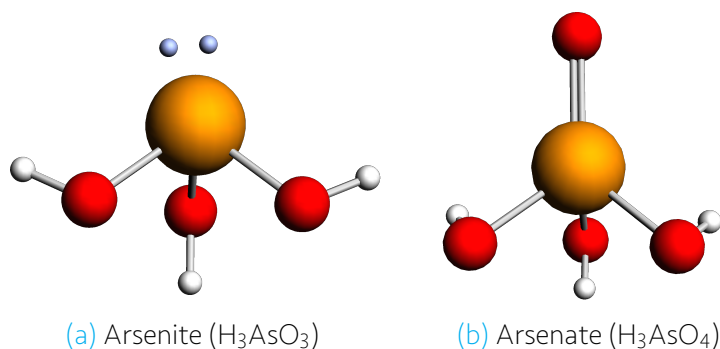


Fig. 3.2: Structures of arsenite and arsenate. Arsenic is represented by orange and sulphur by blue.

The speciation of the oxyanionic acids of arsenic in solution can be seen in the Pourbaix diagram of the As-O-H system, presented in Fig. 3.3. The pKas of arsenites are 9.23 for H_3AsO_3 , 12.13 for $H_2AsO_3^-$ and 13.40 for $HAsO_3^{2-}$; and those for arsenates are 2.3 for H_3AsO_4 , 6.8 for $H_2AsO_4^-$ and 11.6 for $HAsO_4^{2-}$ [21].

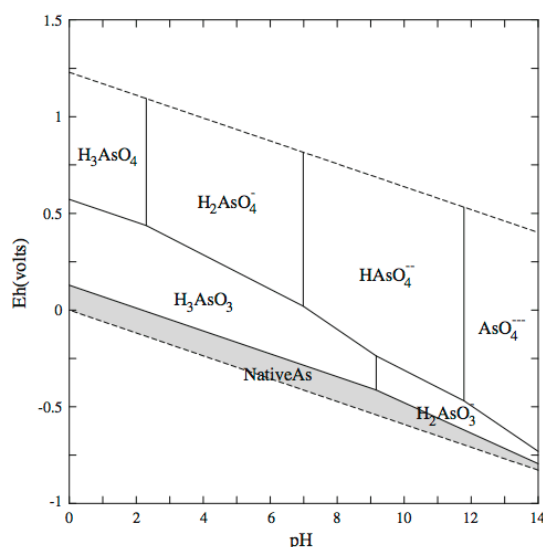


Fig. 3.3: E-pH diagram of the As-O-H system at 25 °C and 1 bar [26].

3.3.1 Adsorption reactions

It is well known that arsenites and arsenates have a high affinity to iron and aluminium oxides. This has been studied with the objective of removing of arsenic species in contaminated ground water by using oxides. Goldberg et al studied the mechanisms of adsorption of arsenite and arsenates in amorphous iron and aluminium oxides [27]. The complexes that the arsenic species form with the oxides can be inner-sphere or outer-sphere. In an inner-sphere complex, there are no water molecules between the absorbing specie and the substrate, while in an outer-sphere complex, one or more water molecules are present. They found that arsenates form inner-sphere complexes with amorphous aluminium and iron oxides forming Al-O-As or Fe-O-As bonds and that the adsorption decreases with increasing pH. Contrarily, arsenites form outer-sphere complexes with amorphous aluminium oxide and it can form both type of complexes with amorphous iron oxide.

3.3.2 Mobility

The mobility of arsenite and arsenate in water is of great interest since the main human exposure to arsenic is through drinking water. The diffusion of ions in water highly depends in the charge of the ion and the size of the atom radius. The ratio between the charge z and the atomic radius r is called the ionic potential (z/r). The higher the ionic potential, the slower diffusion coefficient. A higher charge creates a higher electrostatic interaction between the ions and the water molecules thus producing a thicker hydration layer, which hinders the mobility of the ion. The size of the ion has the same effect, a higher ion will have more difficulty to diffuse through water molecules.

Tanaka et al [28] and Takayashi et al [29] performed experimental and simulation measurements of the diffusion coefficient of arsenite and arsenate in water at different pH values. They found that arsenates have a lower mobility than arsenites in the whole pH scale. Their results are presented in Table 3.1. The lower diffusion coefficient of arsenates is due to the larger size of the molecule. Moreover, they found that an increase in the pH leads to a decrease in the diffusion coefficient. This is explained as by increasing the pH, the degree of dissociation rises, the charge of the ion increases and thus there is more electrostatic interaction making a thicker hydration layer, lowering the diffusion coefficient. This is reflected in the molar volume of the diffusion species $V_{m,H}$, in which the molar volume of the water molecules of the hydration layer are considered. The molar volumes are also presented in Table 3.1. As seen in the table, the higher the pH, the higher the molar volume and the lower the diffusion coefficient. Furthermore, the arsenates have a higher molar volume than arsenites, which indicates a lower diffusion coefficient.

Table 3.1: Diffusion coefficients and molar volumes of arsenite and arsenate species in water [28, 29].

Diffusing specie	pH	D ($10^{-6} \text{ cm}^2 \text{ s}^{-1}$)	$V_{m,H}$ ($\text{cm}^3 \text{ mol}^{-1}$)
Arsenites			
H_3AsO_3	2-6	11.6	79.9
H_2AsO_3^-	11.0	9.71	107.4
Arsenates			
H_3AsO_4	1.0	8.75	127.8
H_2AsO_4^-	4.75	8.12	144.7
HAsO_4^{2-}	9.2	7.27	215.2
AsO_4^{3-}	12.0	6.40	174.2

Chapter 4

Methodology

In this chapter, the methodology followed in this thesis is presented along with the fundamentals of the techniques and the experimental conditions used. As mentioned before, paintings are complex systems composed by several layers that are at the same time made by a wide variety of materials. Therefore, multiple interactions exist and, in combination with water, light, temperature and time, different reactions may occur. In order to study these systems, it is necessary to simplify them and start with a basic model system that allows the investigation of a particular interaction. This simple system can be further complemented by adding each time other components or processes to get closer and closer to resembling a real painting.

In this thesis, two approaches were chosen to get an insight into the diffusion of arsenic species through the paint layers.

The first approach, called ex-situ experiments, consists in the analysis of a set of painting reconstructions. The reconstructions are composed of a ground layer and an orpiment pigment layer and were light aged and kept under different levels of relative humidity for a period of 10 months. The aim of this section is to identify any oxidation or migration of the arsenic compounds and to study the effect of the type of ground and humidity in these processes. These analysis was performed with Fourier Transform Infrared (FTIR) Microscopy and Scanning Electron Microscopy (SEM-EDS).

In the second approach, called in-situ experiments, the diffusion of arsenic species in two varnishes and two binders commonly used in paintings was studied. Since the hypothesis of this work is that the arsenic compounds are transported through the paint layers via water, the diffusion of water in the study case materials needs to be firstly addressed. Beside setting a starting point for the methodology, it provides a characterization of the materials and gives an indication on how the arsenic may diffuse. Finally, the diffusion of arsenate and arsenite through the materials was studied. The techniques used were Total Reflectance Fourier Transform Infrared spectroscopy (ATR-FTIR) and Electrochemical Impedance Spectroscopy (EIS).

4.1 Ex-Situ experiments

As mentioned above, the ex-situ experiments consist in the analysis of painting reconstructions. These were prepared by Arie Wallert and Katrien Keune on April 12th, 2016. The reconstructions consist of an orpiment layer on top of different grounds. The orpiment paint was composed of a pigment mixture of Natural Pigments Rubvel and one that Wallert synthesized himself using the dry sublimation process. The binder used was raw linseed oil from Kremer in a ratio that yielded a workable paint. Additionally, a few glass beads provided by E. Hermens and a small amount of alkyd oil from Talens were added to facilitate drying. Three different grounds were tested: chalk, clay earth and lead white, and they were provided by Maartje StolsWitlox and Emilie Froment from C&R, UvA. The composition of the clay earth ground is 56% silicon dioxide, 29% aluminium oxide, 1.2–1.7% iron oxide, 1.6% titanium oxide, 0.3% calcium oxide, 0.37% magnesium oxide, 3% potassium oxide, and 0.5% sodium oxide. Canvas was chosen as a substrate to allow for humidity to pass entirely through the paint films, as opposed to a glass slide that would block airflow. For 27 days (April 20th - May 16th, 2016), three quarters of the paint outs on each ground type were light aged in a XENOS light ageing chamber. The chamber uses visible and ultraviolet light to represent normal day conditions through normal glass. The Xenon lamp strength was 105 lx and has a 320 nm cutoff filter. The chamber was held constant at 40% RH and at 50 °C due to the heat generated by the lamp.

The samples were kept at relative humidities of 11%, 43% and 93% for a period of 10 months. For this thesis, cross-sections were taken with an scalpel from the 9 samples (3 grounds in 3 different RH) and embedded in Technovit LC 2000 (Heraeus Kulzer GmbH). The embedding resin was wet-polished until the sample was almost exposed and then dry-polished with MicroMesh sanding papers of grades 4000, 6000, 8000 and 12000. The cross-sections were then analysed with SEM-EDS and FTIR microscopy to identify the presence of oxidation and migration products.

4.1.1 FTIR microscopy

The Fourier Transform Infrared spectroscopy (FTIR) is a technique that provides information about the functional groups that compose the molecules of a sample. When exposed to infrared radiation, the molecules go from their ground state to an excited vibrational state. The energy required for the transition is quantized, which means that it only happens if the molecule is exposed to an energy equal to $1/2h\nu$, where h is the Planck's constant and ν is the frequency of the vibration. Each molecule has different vibrational modes depending on the number of atoms, and each vibration corresponds to a certain energy. By this principle, it is possible to identify what molecules are present in the sample by detecting this energy and correlating it to the particular vibration characteristic of a functional group. An example of an FTIR spectra is presented in Fig. 4.1. In this image, the spectra of hexanoic acid is shown. The intensity of the transmitted radiation (transmittance) is plotted as a function of the wavenumber of the IR radiation. The wavenumber is the reciprocal of the wavelength and instead of the transmittance,

the absorbance of the IR radiation is sometimes used. This way, the signals present at certain wavenumbers are correlated to the vibration of functional groups.

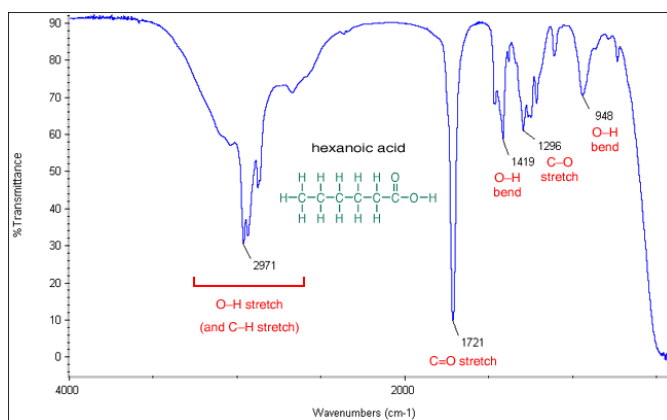


Fig. 4.1: FTIR spectra of hexanoic acid [30].

Furthermore, there must be a change in the net dipole moment of the molecule for a transition to occur. Therefore, a dipole moment must exist in the molecule, meaning that homonuclear diatomic molecules are not affected by the radiation and thus, not detected. The vibrations of the molecule refer to the stretching and bending of the bonds between its atoms and depend on the bond strength and the mass of the atoms [31]. There are mainly 6 vibrational modes, that are shown in Fig. 4.2.

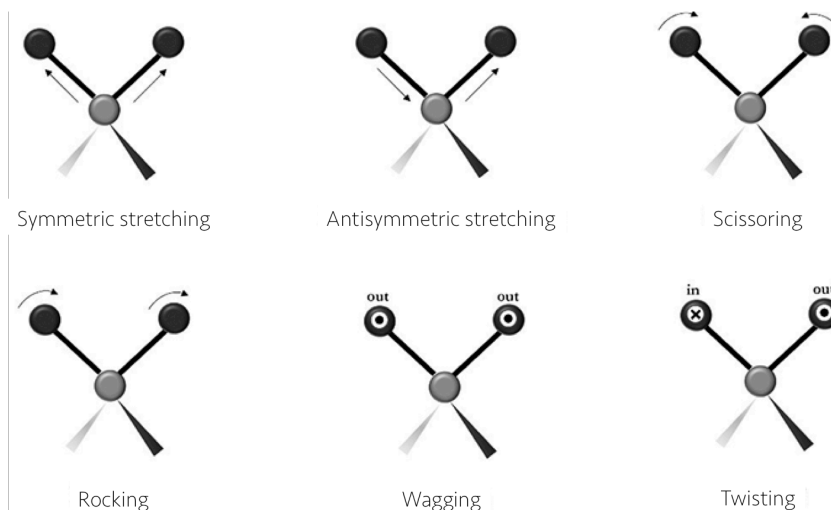


Fig. 4.2: Main vibrational modes [32].

A modern application of FTIR spectroscopy is FTIR microscopy, an imaging technique in which FTIR spectra are collected over the whole surface of a sample. Intensity maps can be produced for each vibration, so that the distribution of a certain functional group over the sample is known. In this thesis, FTIR microscopy was used to analyse the cross-sections of the painting reconstructions to identify the oxidation and migration of the arsenous pigment through the As-O vibration.

The cross-sections were analysed with a Perkin Elmer Spotlight 400 FTIR imaging system with a mercury cadmium telluride (MCT) detector. The spectral maps were taken with a spatial resolution of 8 cm^{-1} and a pixel resolution of $1.56\text{ }\mu\text{m}$.

4.1.2 SEM-EDS

Scanning electron microscopy (SEM) is a localized imaging technique that enables to produce images of the surface of a sample with magnifications up to 10,000x. A sample is placed under an electron beam that is directed by a series of lenses. The electrons of the beam have different interactions with the sample, which yield different information. These are shown schematically in Fig. 4.3.

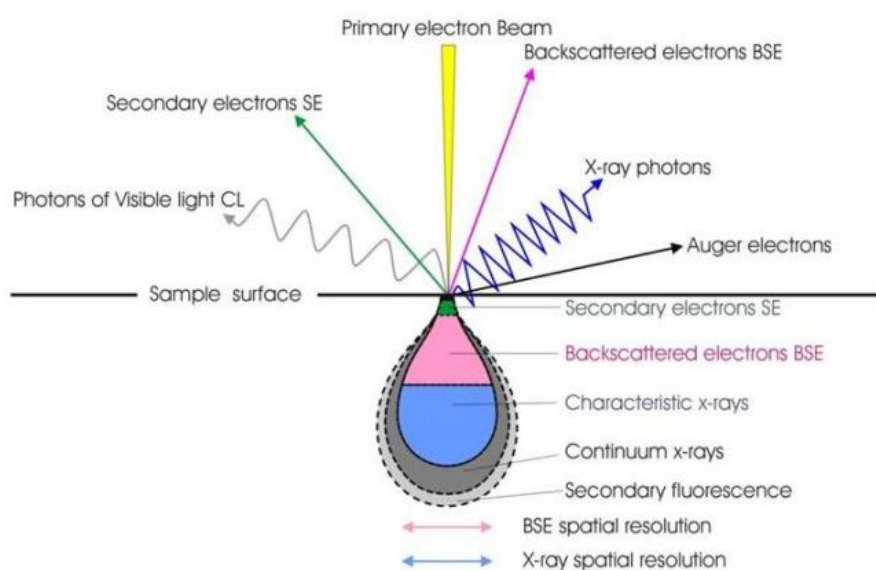


Fig. 4.3: Schematic representation of electron interactions in SEM [33].

One kind of interaction is inelastic scattering, in which the sample is ionized by the incident electrons and those emitted electrons are detected (secondary electrons or SE). The amount of secondary electrons produced depends on how the beam touches the surface of the sample. It is based in the so called *edge effect*, in which more electrons can leave the sample at edges compared to a flat surface and produce a brighter image. This provides information about the morphology and surface topology of the sample, which is the most common application of SEM.

The second kind of interaction is elastic scattering, in which electrons from the incident beam are diffracted back and detected (called backscattered electrons or BSE). Since heavy elements scatter the electrons more strongly than light elements, they appear more brightly in the image and it is therefore possible to see differences in composition.

The third kind is fluorescence, in which electrons from outer shells fill the holes left by ionization and produce characteristic X-rays that can be detected to identify the elements present in the sample, a technique called Energy Dispersive Spectroscopy (EDS) [34].

The cross-sections were imaged and analysed with SEM-EDS to identify any possible arsenic migration. The analysis was made in a JEOL JSM-IT100 with an integrated EDS.

4.2 In-situ experiments

In this section, the proposed methodology for the in-situ experiments to study the diffusion of water and arsenic through the materials is described. Two varnishes and two binders that are commonly encountered in paintings were chosen as the study case materials. The analysis was performed with two techniques: Attenuated Total Reflectance Fourier Transform Infrared spectroscopy (ATR-FTIR) and Electrochemical Impedance Spectroscopy (EIS). These two techniques are proposed since they both allow the estimation of the diffusion coefficient, and therefore the results can be compared to each other. Additionally, ATR-FTIR spectroscopy provides information about molecular changes in the coating, which gives an idea of the stability of the materials. On the other hand, with EIS it is possible to analyse individual processes happening in the whole sample. This will become clearer in [Section 4.2.3](#).

4.2.1 Materials

The materials studied in this thesis project are dammar, mastic, animal skin glue and linseed oil. The dammar and mastic varnishes were used from stock solutions from the Conservation Department of the Rijksmuseum and consist in a mixture between dammar resin, turpentine and Shellsol-A and mastic and turpentine, respectively. For the animal skin glue, a mixture of glue and cold water 1:10 was prepared and left overnight for the glue to absorb the water and swell. This mixture was heated to 30°C and stirred until the glue was dissolved and a homogeneous fluid was produced. The linseed oil was mixed in equal proportions with turpentine to lower the density of the oil and achieve a thinner film.

4.2.2 ATR-FTIR spectroscopy

The fundamentals of FTIR spectroscopy are presented in section [4.1.1](#) (page 24). In this section, the ATR-FTIR technique and its application to diffusional studies is presented.

A variation of the FTIR spectroscopy is the Attenuated Total Reflectance FTIR spectroscopy (ATR-FTIR), which is the most widely used FTIR technique nowadays. One of

the disadvantages of the conventional transmission FTIR spectroscopy is that the sample must be diluted to avoid total absorption of the infrared radiation. This is overcome by diminishing the depth of penetration of the infrared beam d_p , which is exactly the principle behind ATR-FTIR. By placing a crystal with a higher reflective index between the infrared beam and the sample, the beam reflects in the internal surface of the crystal with an angle θ and creates an evanescent wave that penetrates into the sample in a lesser amount than the infrared beam alone. Part of the evanescent wave absorbs in the sample and the rest is reflected and collected by the detector (Fig. 4.4).

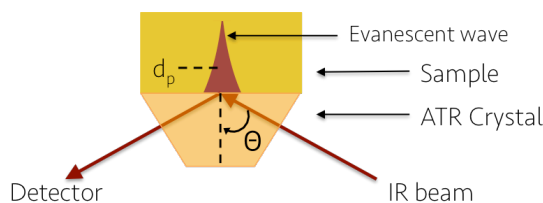


Fig. 4.4: Representation of the evanescent wave in the ATR-FTIR configuration.

With this variation, it is possible to do in-situ measurements and follow the change in composition of a sample over time. One specific application of ATR-FTIR, proposed by Fieldson and Barbari, is the diffusion of molecules through a coating [35]. The equation they developed results from combining the Beer-Lambert law, that states that the measured absorbance is proportional to the concentration and thickness of the sample, and the solution of the Fick's second law for a film in which the solvent enters from only one side of the film. The equation is:

$$\frac{A_t}{A_\infty} = 1 - \frac{8\gamma}{\pi[\exp(-2\gamma L)]} \times \sum_{n=0}^{\infty} \left[\frac{\left[\frac{(2n+1)\pi}{2L} \exp(-2\gamma L) + (-1)^n (2\gamma) \right] \exp\left(\frac{-D(2n+1)^2 \pi^2 t}{4L^2}\right)}{(2n+1) \left(4\gamma^2 + \frac{(2n+1)^2 \pi^2}{4L^2}\right)} \right] \quad (4.1)$$

where A_t is the measured absorbance at time t , A_∞ represents the absorbance at equilibrium, γ is the reciprocal of the penetration depth d_p , D is the diffusion coefficient and L is the thickness of the film.

Methodology: Diffusion studied by ATR-FTIR

The experiments were performed in a Thermo Scientific Nicolet 6700 FT-IR spectrometer equipped with a VeeMAX III PIKE module and a Mercury Cadmium Telluride (MCT) detector. The spectra was collected by co-adding 32 scans with a spacial resolution of 4 cm^{-1} corresponding to a scanning time of 14s. A ZnSe ATR-crystal with a face angle of 60° was used and the incident angle of the beam was adjusted to 80° .

Water diffusion studied by ATR-FTIR

For the water diffusion measurements, the materials were applied drop-wise to the ATR-crystal and heated in an oven at 80°C until dry. The quantity of material applied to the crystal was such to produce a thickness between 25 and 30 μm of dried film. The thickness was measured with a Mitutoyo digital micrometer as the difference in thickness of the ATR-crystal with and without coating. The coated crystal was allowed to cool down to room temperature and was mounted in the ATR cell as shown in Fig 4.5. The cell consists in a chamber where the ATR-crystal is mounted facing upwards with a liquid cell placed on top. The IR radiation penetrates from one of the faces of the crystal a distance that depends on the angle of incidence and the refractive index of the crystal and the coating on top. The chamber was purged with nitrogen to avoid CO_2 and H_2O from the environment. A spectra of the coated crystal was taken prior to the experiments and used as a background. Additionally, spectra of the dried coatings was taken to characterize the coatings and used as reference for the subsequent experiments.

In the arsenic diffusion experiments, D_2O was used instead of H_2O since the O-H vibration of H_2O overlaps with the As-O vibration. Moreover, hydroxyl groups are present in the molecules of the coatings and would interfere in the quantification if water is used. When using D_2O , there is a shift of the peaks to higher wavenumbers that allows the visualization of the arsenate peaks. For consistency, D_2O was used in the water diffusion experiments. Therefore, 2 ml of D_2O (99.9 atom% D, Sigma Aldrich) were added to the cell and spectra was collected every 30 minutes for a period of 40 hours. The spectra was processed with Matlab and the water diffusion coefficient was calculated with equation 4.1.

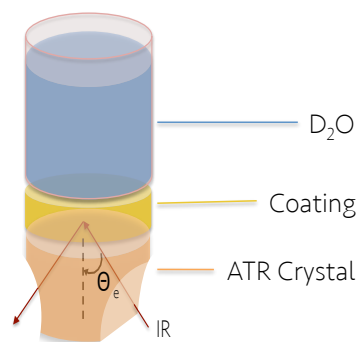


Fig. 4.5: ATR-FTIR cell configuration.

Arsenates diffusion studied by ATR-FTIR

Due to time constraints only the arsenate diffusion, and not the arsenite, was analysed with ATR-FTIR. The same procedure than that for water was followed, however some modifications were made. A 0.01M arsenic solution was prepared by dissolving sodium arsenate $\text{Na}_2\text{HAsO}_4 \cdot \text{H}_2\text{O}$ ($\geq 98.0\%$, Sigma Aldrich) in D_2O . For the arsenate ions to be

detected, they need to be absorbed in a substrate. Since the arsenate forms a complex with aluminium oxide [27], a layer of aluminium was deposited on top of the ATR-crystal before applying the coating. This way, the arsenic species travel through the entire thickness of the film, react with the aluminium oxide layer and are detected with the ATR-FTIR. The aluminium layer was deposited in a Normvac evaporator to a thickness of approximately 15 nm. The coating was applied and dried as described above and spectra was measured likewise. The following experiments were performed:

- Aluminium layer with D_2O , to verify the stability of the aluminium oxide to D_2O .
- Aluminium layer with arsenate solution, to see how fast the absorption reaction is and to what wavenumber the As-O vibration corresponds (as it shifts with the pH of the solution).
- Aluminium layer coated with dammar with arsenate solution, to study the diffusion of arsenates in dammar.

For the arsenate diffusion analysis, the background was taken as the spectra of the ATR-crystal with the aluminium layer and the dry coating.

4.2.3 Electrochemical Impedance Spectroscopy

Electrochemical impedance spectroscopy (EIS) is a technique based on the response of an electrode to an applied alternating voltage at different frequencies. It is a powerful technique that provides qualitative and quantitative, as well as time-dependent information of processes taking place at the interface between a metal and an electrolyte.

The most common and standard procedure, is to apply a small alternating potential signal (in the order of mV and a frequency range from 10^{-4} to 10^6 Hz) to an electrode, the resulting current is measured and the impedance at each frequency is computed. Although the voltage-current relation in an electrochemical cell is coherently non-linear, it is possible to work within a range in which this dependence is approximated as linear (Fig 4.6). This is the case for a potential with an amplitude in the range of 5-10 mV.

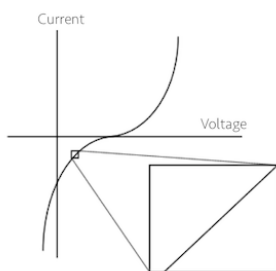


Fig. 4.6: Voltage vs current curve showing a range where the relation can be considered linear.

Fundamentals of EIS

A detailed explanation of the fundamentals of EIS can be found in [36, 37, 38, 39]. Only a summary is presented in this section. The *impedance*, Z , is defined as the tendency of a circuit to resist (or impede) the flow of an alternating electric current. The applied sinusoidal voltage $E_{(t)}$ is expressed as

$$E_{(t)} = E_0 \sin(\omega t) \quad (4.2)$$

where E_0 is the maximum amplitude of the voltage, ω is the angular frequency and t is the time. The resulting current $I_{(t)}$ is also a sinusoidal signal of the same angular frequency but it is shifted in time due to the slow response of the system (Fig. 4.7) and is described by

$$I_{(t)} = I_0 \sin(\omega t - \phi) \quad (4.3)$$

where I_0 is the maximum amplitude of the current and ϕ is the phase shift.

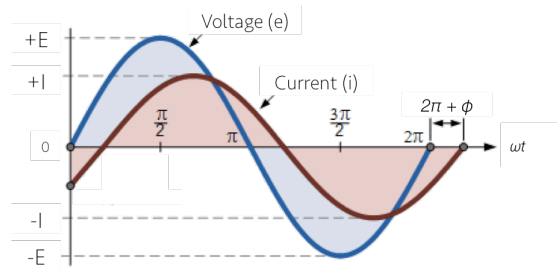


Fig. 4.7: Voltage and current as a function of time showing the phase shift between them [40].

The impedance is described by an equation analogous to Ohm's law ($R = E/I$) but with a frequency dependency:

$$Z(\omega) = \frac{E_{(t)}}{I_{(t)}} \quad (4.4)$$

Substituting with equations 4.2 and 4.3,

$$Z(\omega) = \frac{|E_0| \sin(\omega t)}{|I_0| \sin(\omega t - \phi)} = Z_0 \frac{\sin(\omega t)}{\sin(\omega t - \phi)} \quad (4.5)$$

The relationship between voltage and current can be studied in terms of vectors that share a common origin and are separated by the phase angle ϕ and are best described by complex numbers. Using Euler relationship, $\exp(jx) = \cos(x) + j \sin(x)$, where j is the complex number $j = \sqrt{-1}$, the equations for the voltage and current (4.2 and 4.3, respectively) are transformed to:

$$E_{(t)} = |E_0| \exp(j\omega t) \quad (4.6)$$

$$I_{(t)} = |I_0| \exp(j\omega t - j\phi) \quad (4.7)$$

Therefore, the impedance can be rewritten as:

$$Z(\omega) = \frac{|E_0| \exp(j\omega t)}{|I_0| \exp(j\omega t - j\phi)} = |Z_0| \exp(j\phi) = |Z_0| \cos(\phi) + j |Z_0| \sin(\phi) \quad (4.8)$$

where $[|Z_0| \cos(\phi)]$ is the real component Z' and $[j |Z_0| \sin(\phi)]$ is the imaginary component Z'' of the impedance, leading to the general expression for the impedance

$$Z(\omega) = Z' - jZ'' \quad (4.9)$$

The magnitude of the impedance is then $|Z|^2 = (Z')^2 + (Z'')^2$ and the phase angle

$$\tan \phi = \frac{Z''}{Z'} \quad (4.10)$$

There are two commonly used graphic representations of the impedance data. The first one is called a *Nyquist plot*, in which, for different values of ω , the real component Z' is plotted in the x axis and the imaginary component Z'' , in the y axis. An example is presented in Fig. 4.8a. In this kind of plots, the frequency is not display explicitly. However, the values closer to the origin correspond to higher frequencies. Moving further away from the origin the frequency tends to smaller values.

The second representation is the *Bode plot*, that consist in two graphs, shown in Fig. 4.8b. In the first one, the magnitude of the impedance $|Z|^2$ is plotted as a function of the frequency ω and in the second one, the phase angle ϕ is plotted also as a function of ω .

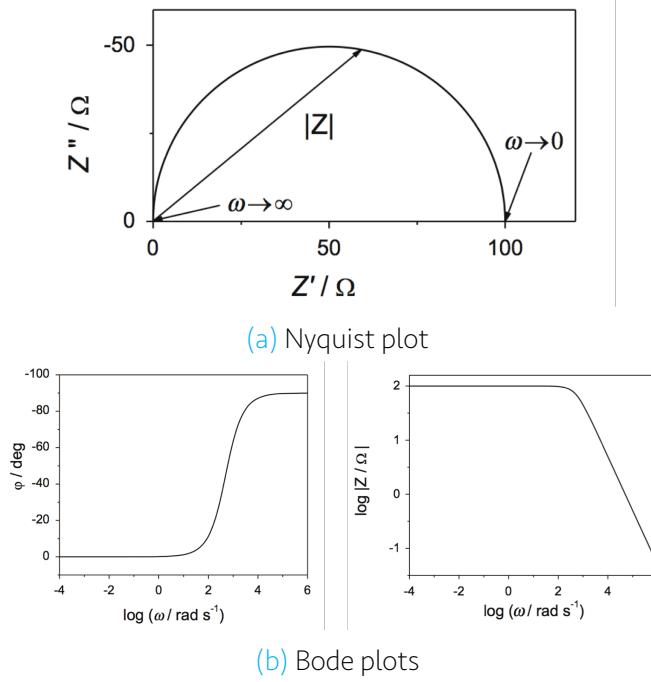


Fig. 4.8: Typical Nyquist and Bode plots of impedance data [39].

The experimental impedance data is commonly analysed by fitting it to an equivalent electrical circuit to obtain quantitative information about the system. The equivalent circuit contains electrical components, such as resistors and capacitors, that resemble the processes taking place in the real system. It is therefore important to know the impedance equations of these circuits.

For example, in a circuit composed of a pure resistance, the response to a sinusoidal voltage can be described by Ohm's law ($R = E/I$), which corresponds to a situation where the phase shift $\phi=0$ and the vector diagram is that of figure 4.9a.

On the other hand, for a circuit with a pure capacitance, the current is described by

$$I = C \frac{dE}{dt} \quad (4.11)$$

Solving with the equation of the sinusoidal voltage (equation 4.2), $I_t = \omega C E_0 \cos(\omega t)$. Since $\cos(\omega t) = \sin(\omega t + \pi/2)$ and defining the *capacitive reactance* as $\chi_c = 1/\omega C$,

$$I_t = \frac{E_0}{\chi_c} \sin\left(\omega t + \frac{\pi}{2}\right) \quad (4.12)$$

Here the phase shift $\phi = \pi/2$ and the vector diagram is as the one shown in Fig. 4.9b. In this situation, it is said that the current leads the voltage and the vector diagram is expanded into a plane, as shown in Fig. 4.9b. This is the reason why the notation in complex numbers is introduced as it simplifies the mathematical treatment. In this case,

the components of the imaginary axis are multiplied by the complex number $j = \sqrt{-1}$, hence $E = -Ij\chi_c$.

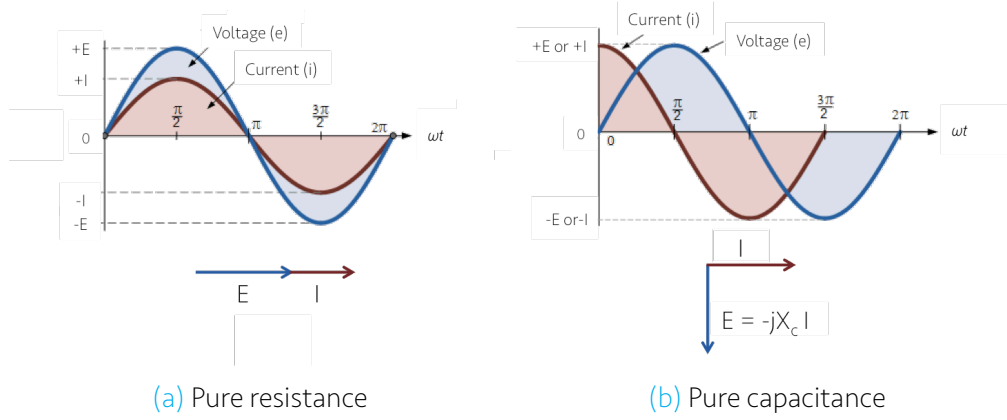


Fig. 4.9: Relation between alternating voltage and current across a (a) pure resistance and (b) pure capacitance [40].

Summarizing, for an individual resistance and an individual capacitance,





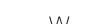
$$\text{Pure resistance} \quad E = IR \quad \phi = 0 \quad (4.13)$$

$$\text{Pure capacitance} \quad E = -Ij\chi_c \quad \phi = \pi/2 \quad (4.14)$$

These elements can be combined in a circuit in different ways, a simple example is a resistance in series with a capacitance. In this circuit, the sum of the voltage drop across the individual elements must be equal to the applied voltage. Therefore, $E = E_R + E_C$ and substituting with equations 4.13 and 4.14, $E = IR + (-jI\chi_c)$, or $E = I(R - j\chi_c)$. Therefore, the voltage and the current are related to each other through the vector $R - j\chi_c$, which is in fact, the impedance of the circuit: $E = IZ$.

In this way, different circuits can be constructed in which the elements or combination of elements, represent the processes happening in the real system, such as the corrosion of a metal, an oxide film formation or the diffusion of species in the solution. The most commonly used electrical elements are presented in table 4.1. To compute the total impedance, the individual impedance vectors of the elements are added. The impedance of the elements in series is calculated as the sum of the individual values, while for elements in parallel, the inverse of the overall impedance is equal to the sum of the reciprocals of the individual impedance vectors.

Table 4.1: Circuit elements commonly used in the models

Element	Impedance	Symbol
Resistor	R	
Capacitor	$\frac{1}{j\omega C}$	
Inductor	$j\omega L$	
CPE	$\frac{1}{Q(j\omega)^\alpha}$	
Warburg	$\sigma\omega^{-1/2} - j\sigma\omega^{-1/2}$	

A commonly used circuit to model the electrical behaviour of the interaction between the metal and the electrolyte is the complete *Randles circuit*, presented in Fig. 4.10 along with the correspondent Nyquist and Bode plots. This circuit represents a mixed kinetic and diffusion controlled process taking place in the electrode-electrolyte interface. In most cases, a simplified version of the circuit is used, called the *simplified Randles circuit*, which consists of only the R_s , R_{ct} and C_{dl} .

The typical Nyquist plot of the complete Randles circuit shows a semicircle representing the kinetic controlled process at the high frequency region (closer to the origin), while at low frequencies (away from the origin) the mass transport is the limiting process.

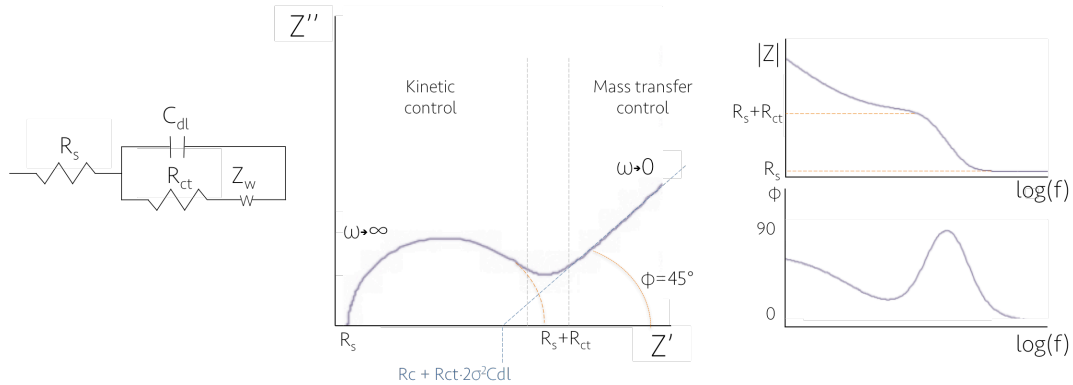


Fig. 4.10: Randles equivalent circuit model, Nyquist and Bode plots.

The first element is R_s , which represents the resistance imposed by the solution to the current. Sometimes it is treated as a general resistance R_Ω to account for uncompensated resistances. It can be calculated as the high-frequency intercept with the real axis in the Nyquist plot. The second element is C_{dl} , the double layer capacitance. When a charged electrode is in contact with an electrolyte, ions from the solution absorb in the surface of the electrode to compensate for the surface charge and an electric double layer is formed, as shown in Fig. 4.11. This double layer can be modelled as a capacitance C_{dl} . The charge transfer resistance R_{ct} , which is connected in parallel, is a resistance formed due to the electron or charge transfer at the interface and it depends on the kinetics of the reaction, temperature, concentration of the reaction products and the potential. It can be calculated from the Nyquist plot, as the diameter of the semicircle, i.e. the right intercept with the real axis minus the solution resistance; or from the Bode

plot as the value of $|Z|$ in which the phase shift is zero. Since a pure resistance has no dependency on the frequency, it shows as a plateau in the Bode plot.

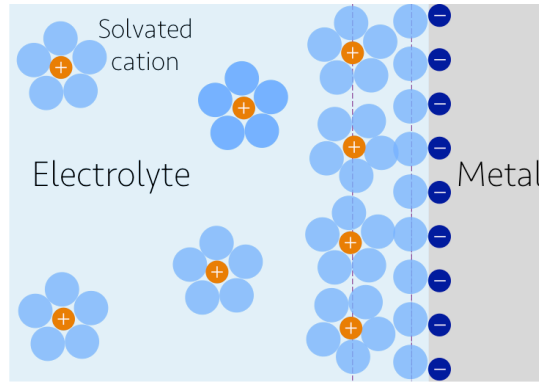


Fig. 4.11: Representation of the double layer formation in the electrode-electrolyte interface.

Warburg impedance

In certain occasions, for example when the metal is covered with absorbed components from the solution or is coated, the reaction may be limited by the diffusion of reactants to the interface. In this cases, an element called *Warburg Impedance* Z_w is added to the circuit in series with the R_{ct} . It appears at low frequencies since the diffusion is a slow process and at high frequencies, the molecules do not have enough time to move. The Warburg impedance can be regarded as a frequency dependent resistance connected in series with a capacitance. It is deduced considering the electrochemical reaction $O + ne \rightleftharpoons R$ and a linear diffusion of the species through a semi-infinite layer, which results in the equation

$$Z_w = \sigma \omega^{-1/2} - j(\sigma \omega^{-1/2}) \quad (4.15)$$

$$\sigma = \frac{RT}{F^2 n^2 A \sqrt{2}} \left(\frac{1}{D_o^{1/2} C_o} + \frac{1}{D_R^{1/2} C_R} \right) \quad (4.16)$$

where σ is the Warburg coefficient, R is the gas constant, T is the absolute temperature, F is the Faraday constant, n is the number of electrons A is the area of the electrode surface, D_o and D_R are the diffusion coefficients of the oxidized and reduced species, and C_o and C_R are the concentration of the oxidized and reduced species respectively. The phase angle is 45° , as calculated with equation 4.10 and it shows in the Nyquist plot as a straight line with a slope of -1 at low frequencies and in the Bode plot as an angle of 45° (Fig. 4.12).

Once every element is defined, the total impedance of the cell can be computed. As stated above, the Warburg impedance is small compared to R_{ct} in the high frequency range. Therefore, the real and imaginary components of the impedance take the limiting form:

$$Z' = R_s + \frac{R_{ct}}{1 + \omega^2 C_{dl}^2 R_{ct}^2} \quad (4.17)$$

$$Z'' = \frac{\omega C_{dl} R_{ct}^2}{1 + \omega^2 C_{dl}^2 R_{ct}^2} \quad (4.18)$$

On the other hand, the low frequency region will have the form:

$$Z' = R_s + R_{ct} + \sigma \omega^{-1/2} \quad (4.19)$$

$$Z'' = \sigma \omega^{-1/2} + 2\sigma^2 C_{dl} \quad (4.20)$$

Combining equations 4.19 and 4.20 and eliminating ω ,

$$Z'' = Z' - R_s - R_{ct} + 2\sigma^2 C_{dl} \quad (4.21)$$

This last equation implies that the Warburg coefficient can be calculated from the intersection of the straight line with the real axis in the Nyquist plot since $Z' = R_s + R_{ct} - 2\sigma^2 C_{dl}$ when $Z'' = 0$. However in practice, the diffusion is not through a semi-infinite layer. Most of the times there is a coating or membrane with a defined thickness hindering the diffusion. Therefore, the Warburg impedance has to be modified to model a finite length diffusion. There are two cases in which this can be treated:

- **Reflective boundary:** The diffusion of mobile species is distributed in an impermeable layer where no charge transfer is possible. Assuming the diffusion of only one species, the Warburg impedance, also called *open circuit* Warburg impedance, is given by

$$Z_w^o = \frac{\sigma}{\sqrt{j\omega}} \coth \left[\sqrt{\frac{j\omega}{D}} l_e \right] \quad (4.22)$$

where l_e is the diffusion layer, which is the region in the vicinity of the electrode where a concentration gradient of the diffusing specie is built.

At high frequencies, the penetration length of the ac signal is smaller than the layer thickness. Due to the fact that the layer is impermeable, at lower frequencies the charges accumulate in the interface between the layer and the electrolyte and a capacitor-like behaviour is produced (Fig. 4.12). The imaginary component of the impedance tends to infinity since no current can flow in the system.

- **Transmissive boundary:** The species diffuse through a semi-permeable layer before reaching the electrode interface. The Warburg impedance, also called *short circuit* Warburg impedance is:

$$Z_w^s = \frac{\sigma}{\sqrt{j\omega}} \tanh \left[\sqrt{\frac{j\omega}{D}} l_e \right] \quad (4.23)$$

At high frequencies, where the time available for the species to move is short, the oscillation in the concentration will be given by only those located in the vicinity of the electrode, which can be regarded as a diffusion in a semi-infinite layer. At lower frequencies, the system resembles a dc system as the species are able to move across the entire thickness of the layer and a current can flow. A resistance is built, which can be seen as a semicircle in the Nyquist plot (Fig 4.12).

The limiting value of the Warburg impedance when $\omega \rightarrow 0$ is

$$Z_w^s = \frac{W_R}{\sqrt{j\omega W_T}} \tanh \sqrt{j\omega W_T} \quad (4.24)$$

$$\text{where } W_R = \frac{\sqrt{2}\sigma l_e}{\sqrt{D}} \quad (4.25)$$

$$\text{and } W_T = \frac{l_e^2}{D} \quad (4.26)$$

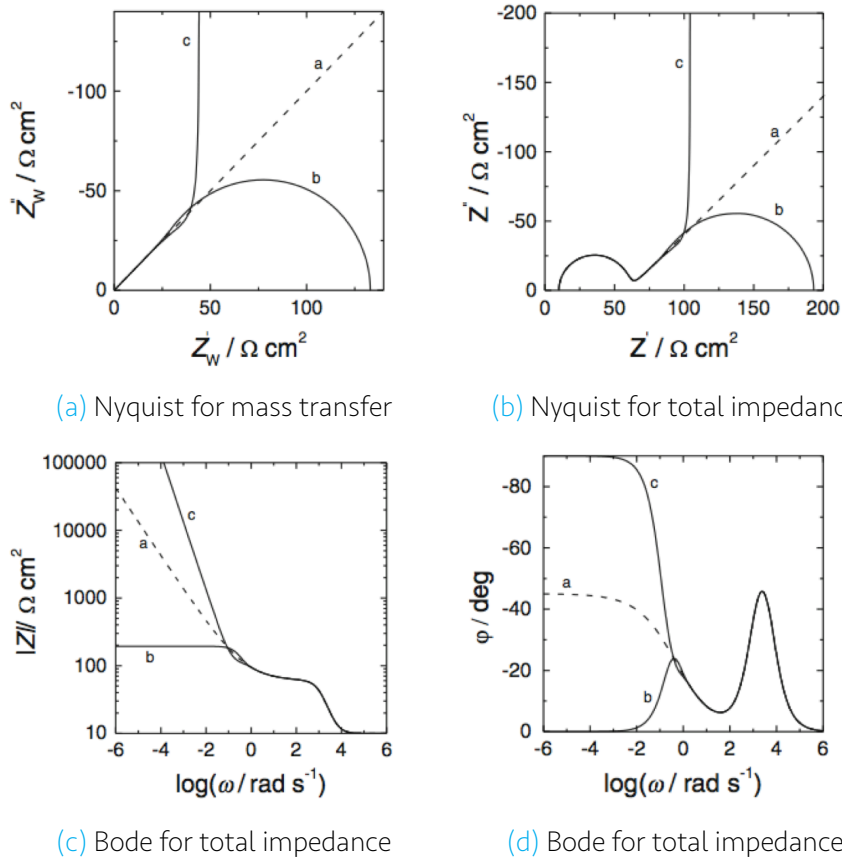


Fig. 4.12: Nyquist and Bode plots of mass transfer and total impedance for *a*: semi-infinite, *b*: transmissive, and *c*: reflective boundary [39].

The Warburg impedance is relevant to this thesis since it is the method by which the diffusion coefficient of arsenates and arsenites is estimated. The analysed sample is formed by a coated metal immersed in an arsenite or arsenate solution. This way, the diffusion of the arsenic species will be hindered by the coating producing a Warburg impedance behaviour seen in the Nyquist and Bode plots. In this case, the reaction that is limited by the diffusion process is the absorption of arsenates or arsenites in aluminium oxide. Therefore, in order to calculate the diffusion equation, an approximation is made where only the concentration of the arsenites or arsenates species is considered:

$$\sigma = \frac{RT}{F^2 A \sqrt{2D^{1/2}C}} \quad (4.27)$$

Water diffusion through a coating

An ideal coating can be modelled as a capacitor whose capacitance C_c is given by

$$C_c = \frac{\varepsilon A \varepsilon_0}{d} \quad (4.28)$$

where ε is its dielectric constant, ε_0 is the permittivity of vacuum, A is the surface area and d is the thickness of the coating.

There are two approaches to calculate the capacitance of the coating, the first one is by using the imaginary component of the impedance at high frequency (between 1 and 10 kHz), where the coating capacitance is the mainly EIS response [41]. The capacitance is calculated as:

$$C_{HF} = -\frac{1}{2\pi f Z''} \quad (4.29)$$

where f is the frequency and Z'' is the imaginary part of the impedance between 1 and 10 kHz.

However, generally the coating does not behave as an ideal capacitor. This is caused by contamination or roughness across the thickness of the coating or to a non-uniform current distribution. Often, a *constant phase element*, or *CPE*, is used to take into account such inhomogeneities. Therefore, the impedance of the capacitor is replaced by the impedance of the CPE:

$$Z_{CPE} = \frac{1}{Q(j\omega)^\alpha} \quad (4.30)$$

where Q is the parameter related to the capacitance and α is the constant phase exponent ($0 < \alpha < 1$). When $\alpha = 1$, the impedance corresponds to that of an ideal capacitor. The non-ideal behaviour of the capacitance can be seen in the Nyquist plot as a depressed semi-circle and in the Bode plot as a deviation to lower angles (Fig. 4.13).

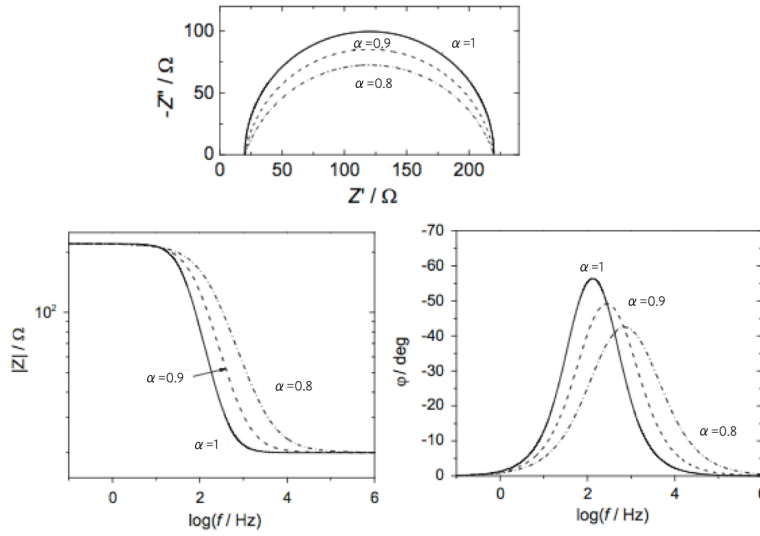


Fig. 4.13: Nyquist and Bode plots of a simplified Randles circuit showing the behaviour of a CPE [39].

There have been studies using the CPE as the capacitance of the coating to calculate the water uptake, however it has been found that the results are far from the real ones and an effective capacitance has to be obtained from the CPE parameters [42]. There are two ways to calculate the effective capacitance. The Eq. 4.31 was proposed by Brug, who attributed the non ideal behaviour to heterogeneities along the surface of the coating. And Eq. 4.32, proposed by Hsu to take into account a variation normal to the surface [43]. Both equations have been used to calculate capacitances for similar systems for a wide variety of applications. Nevertheless, it remains unclear which approach yields the best results.

$$C_{eff}^B = [Q \cdot R_s^{(1-\alpha)}]^{1/\alpha} \quad (4.31)$$

$$C_{eff}^H = [Q \cdot R_c^{(1-\alpha)}]^{1/\alpha} \quad (4.32)$$

During immersion, there is a change in the capacitance of the coating. As water starts to penetrate, it changes the dielectric constant of the coating (normally 3-8) to that of

water (approximately $\varepsilon_w = 80$) and thus, there is an increase in the capacitance. Brasher and Kingsbury proposed equation 4.33 to determine the volume fraction of water, $\phi(\%)$, inside the coating, which has been commonly used by several authors [41, 42, 44, 45, 46].

$$\phi(\%) = \frac{\log(C_t/C_0)}{\log \varepsilon_w} \quad (4.33)$$

where C_t is the capacitance measured at time t and C_0 is the initial coating capacitance. The Brasher and Kingsbury equation have several assumptions:

- The change in the measured capacitance is only due to the penetration of water.
- The distribution of water is random and uniform
- There is no chemical interaction between the water and the coating and thus, the permittivity of water is 80.
- Swelling can be ignored.
- There is no polar solvent in the film.

With EIS, the coating capacitance can be measured over time. If it follows a Fick's diffusion profile, the diffusion coefficient of water through the coating, D , can be estimated with the following equation

$$\phi_t = \phi_s \left[1 - \sum_{n=0}^{\infty} \frac{1}{(2n+1)^2} \exp \left(\frac{-(2n+1)^2 D \pi^2}{4L^2} t \right) \right] \quad (4.34)$$

where ϕ_t is the volume fraction of water absorbed at time t , ϕ_s is the volume fraction of water absorbed at saturation and L is the thickness of the coating.

Methodology: Water diffusion studied by EIS

The diffusion of water through the four materials was studied with EIS. A conventional three electrode set-up was used (Fig. 4.14), in which a Ag/AgCl electrode acted as the reference electrode, a stainless steel mesh as the counter electrode and an aluminium 2024 plate as the working electrode. A 0.01 M Na_2SO_4 solution was used as the electrolyte. The Al plates were mechanically polished to produce an even surface free of scratches and the tested area was 2.5 cm^2 . Each of the materials was applied to an Al plate with a $30 \mu\text{m}$ drawdown bar and dried in an oven at 80°C . The coating thickness was measured with a Mitutoyo digital micrometer as the difference in thickness of the Al plate with and without coating. EIS measurements were performed every 30 minutes

for 24 hours with a Metrohm Autolab potentiostat combined with a FRA2 Module. The applied frequency range was 10^5 to 10^{-2} Hz with a signal amplitude of 10 mV. The data was afterwards processed with the software ZView and Matlab.

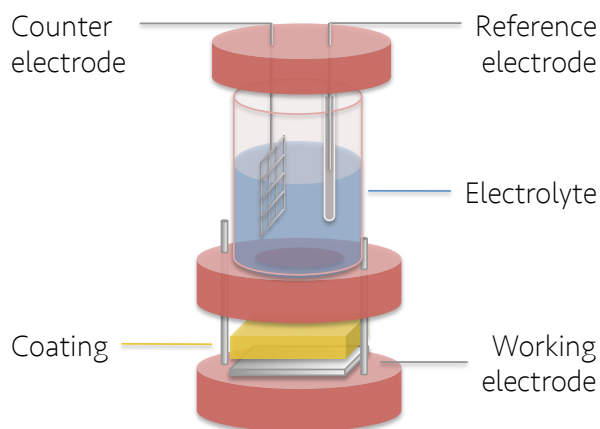


Fig. 4.14: Electrical cell configuration for EIS experiments.

As mentioned previously, both arsenate and arsenite form complexes with aluminium oxide. Therefore, to test the arsenic compounds diffusion through the coatings, the aluminium plate was treated for 30 minutes with a NaOH solution 0.1M to produce an aluminium oxide layer before the application of the coatings. A solution of 0.01M sodium arsenate $\text{Na}_2\text{HAsO}_4 \cdot \text{H}_2\text{O}$ ($\geq 98.0\%$, Sigma Aldrich) or sodium (meta)arsenite NaAsO_2 ($\geq 90\%$, Sigma Aldrich) in H_2O was used as the electrolyte. The experimental conditions are the same as reported above.

Chapter 5

Results ex-situ

In this chapter, the results of the analysis of the painting reconstructions made by FTIR microscopy and SEM-EDS is presented. The reconstructions consist of a ground layer and an orpiment layer on top. The grounds studied were chalk, earth pigment and lead white. And each one of them were kept under three different relative humidity levels: 11%, 43% and 93% for a period of 10 months. For comparison, the samples kept at a relative humidity of 43% are compared.

The hypothesis behind these experiments is that the orpiment will oxidise and migrate into the ground layer. The relative humidity was varied since in a more humid environment, firstly more oxidation is expected, and secondly the arsenic transport is expected to be faster. The paint layers that are in contact with the orpiment can also have an effect in the migration of arsenic species, and thus, three different materials were used as the grounds.

The cross-sections taken from the reconstructions were analysed by two techniques since they both provide different information. With SEM-EDS, the elemental distribution in the sample is obtained. By identifying the elements present in the ground, it is possible to know if the arsenic pigment migrated and in case it did, it can give an indication on the form of the species (oxidised or intact depending on the concentration profiles of arsenic and sulphur). However, not all elements are easily distinguishable. For example, the peaks of sulphur and lead overlap, which is a problem since one of the reconstructions is made of orpiment (arsenic sulphide) and lead white. In this case, it is not possible to detect if there is sulphur present in the lead white layer. By analysing the sample with FTIR microscopy, this issue is overcome since the signal of lead white does not overlap with the arsenic one. Furthermore, the arsenic is detected in this technique only when it is forming a bond with oxygen, (the vibration that is detected is As-O). Therefore, this allows to see if the arsenic has already oxidised.

5.1 Analysis of the cross-section of orpiment and chalk

The SEM image obtained with secondary electrons of the orpiment and chalk cross-section is presented in [Fig. 5.1a](#). It consists of a sample containing two layers. The top layer was identified with EDS as the orpiment, since the arsenic and sulphur concentrations in this part are high, and the bottom layer as the chalk, based on the presence of calcium. A point analysis was made in the surrounding resin to make sure that there is no arsenic or other components of the paint cross-section that may result from smearing when polishing the sample.

The elements of interest, namely arsenic, sulphur and calcium, were mapped with EDS to see their distribution in the sample. The distribution maps are presented in [Figures 5.1b, 5.1c and 5.1d](#). In [Fig. 5.1e](#) the SE image and the maps of arsenic and calcium were superimposed to create one single image and compare the elements distribution with the image.

The arsenic map shows the same patterns as that of sulphur, which is expected since they are both located at the orpiment layer. In the three distribution maps a clear limit is shown in the interface between the layers, there is no overlap between the arsenic and calcium maps. This is better appreciated in the superimposed image where the limit of the layers is clear. It is important to note that the high concentration of arsenic in the orpiment layer sets the intensity scale very high making difficult to identify lower concentrations in other part of the samples. A more localized analysis is therefore more useful, such as a line profile. This is a procedure in which several points along a chosen line are measured with EDS and the mass percent is plotted as a function of the distance. Therefore, the concentration at individual points is known and the plot makes it easier to visualize.

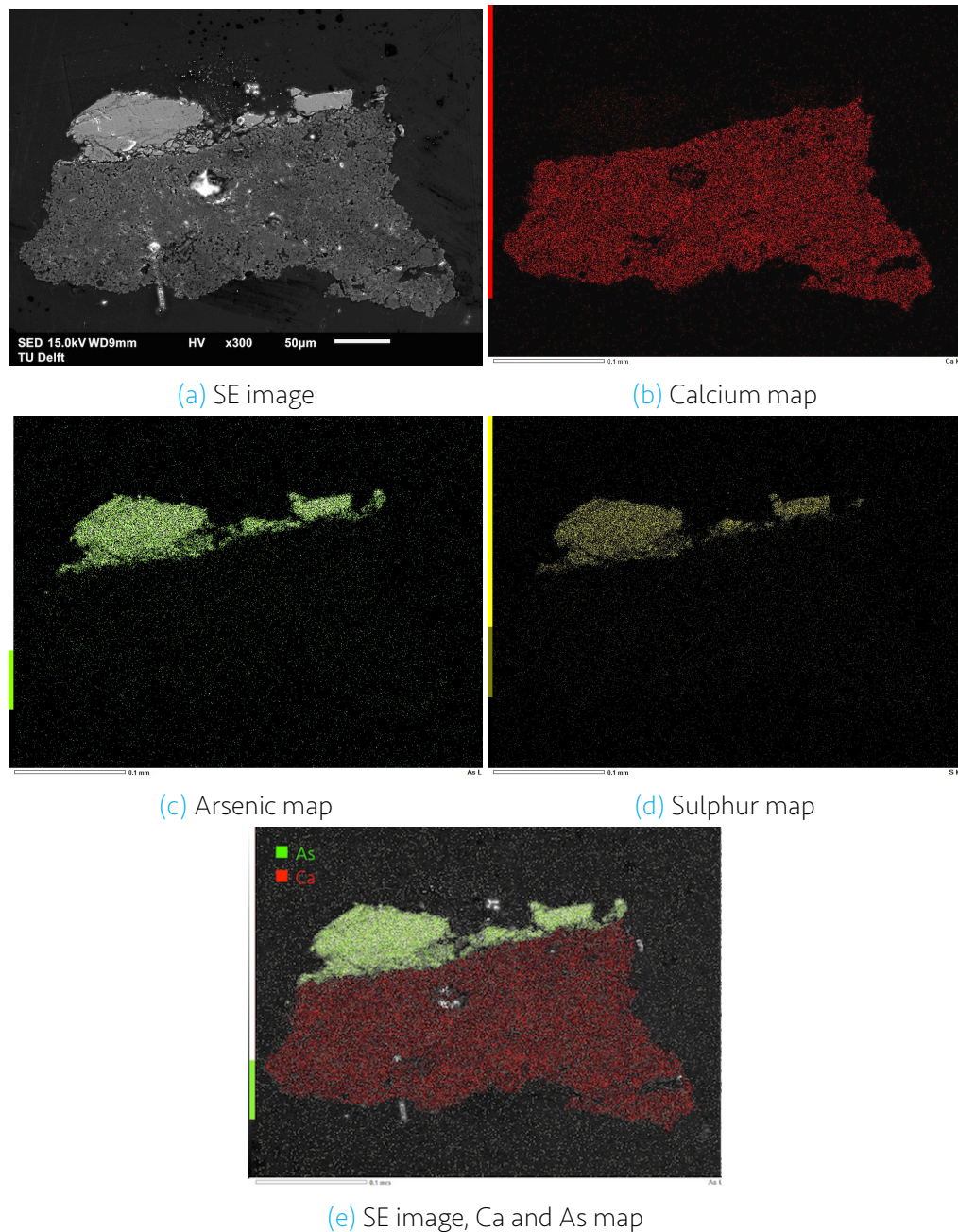


Fig. 5.1: SEM images of the chalk and orpiment cross-section kept at 43% relative humidity.

A line profile was measured in a location close to the interface of the two layers. The location and result of the line profile is presented in Fig. 5.2. In this image it is possible to see the interface closer. The two blue lines in the figure indicate the two points measured closer to the interface. The line at the left is located in a point measured directly at the interface. In this point, the concentration of calcium is zero while arsenic is still present. In the point located at approximately $6\text{ }\mu\text{m}$ at the right of the interface, the calcium concentration abruptly increases since this point is located inside the chalk layer. Here the arsenic is still detected although it is a very low concentration. This may be an indication of the migration of arsenic but the concentration is too low to draw any

conclusions. It is important to note that the line profile was measured with steps of approximately $6\text{ }\mu\text{m}$. Hence, arsenic may be present in-between these two points. Furthermore, the X-rays detected with EDS are not produced solely from the surface of the sample but from a volume below the surface, as shown in Fig. 4.3 from Section 4.1.2. Since the measurements are done close to the interface, the interaction volume of the detected X-rays may be partly localized in the orpiment layer, thus detecting arsenic. The third point, located at approximately $12\text{ }\mu\text{m}$ from the interface does not show any arsenic signals.

The profile of sulphur, although not presented here, matches the profile of arsenic suggesting that the pigment is intact.

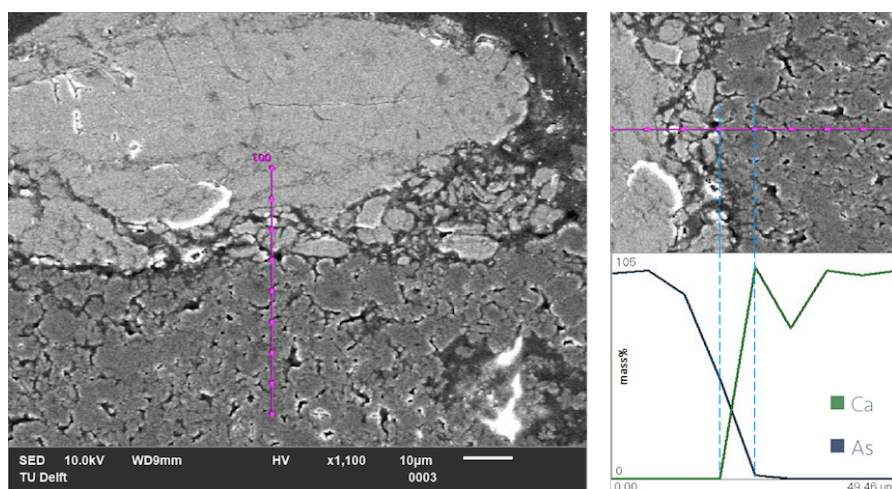


Fig. 5.2: Line profile at the interface of orpiment and chalk.

This sample was also analysed with FTIR microscopy. Spectra were taken in points located at the top and bottom layers and are presented in Fig. 5.3a. In the bottom layer, the spectra show a peak located in 796 cm^{-1} that corresponds to the As-O bond, representing arsenates [1]. The presence of this vibration indicates that there are oxidation products. In the top layer spectra, the C-O characteristic peaks of chalk are observed: 1400 cm^{-1} , 872 cm^{-1} and 712 cm^{-1} . The vibrations in 796 cm^{-1} and 1400 cm^{-1} representative of arsenates and chalk, were chosen to measure distribution maps, presented in Figures 5.3b and 5.3c. In the 1400 cm^{-1} map, the limit of the layer is clearly observed indicating that the chalk is confined and distributed in the bottom layer. The 796 cm^{-1} map shows a high concentration of arsenates in the outer part of the layer. This is caused by a combination of factors. First, these samples were light aged. The inner part of the sample is shielded from light and therefore, less oxidation occurs. The other factor is that the outer part is in more contact with the environment and thus, has more access to oxygen and water. A lower concentration of arsenates is observed throughout the whole top layer. There are certain locations in the bottom layer where the concentration of arsenic is not zero (seen in green). However, this must be considered with care since the intensity shown in the map is the result of the integration of the chosen peak and is highly dependent on the base line, that may vary from one spectrum to another.

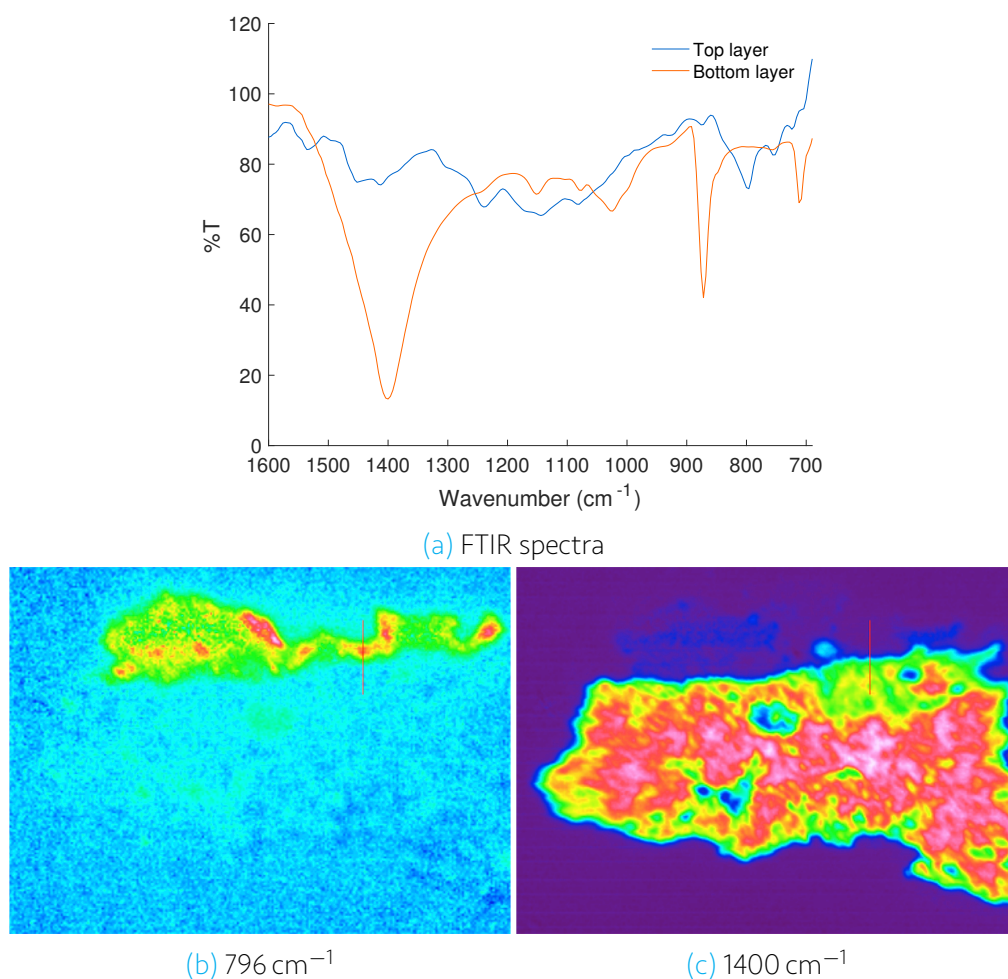


Fig. 5.3: (a): FTIR spectra and (b,c): FTIR microscopy images (red is representative of higher intensity) of the chalk and orpiment cross-section kept at 43% relative humidity for 10 months.

Similarly to the SEM-EDS line profile, a more localised analysis was made. A line profile close to the interface was measured and is shown in Fig. 5.4. A slight overlap between the profiles is observed at approximately $10\text{ }\mu\text{m}$ deep into the chalk layer. Even though the intensity of the arsenates in this region is very low, it may be an indication of migration.

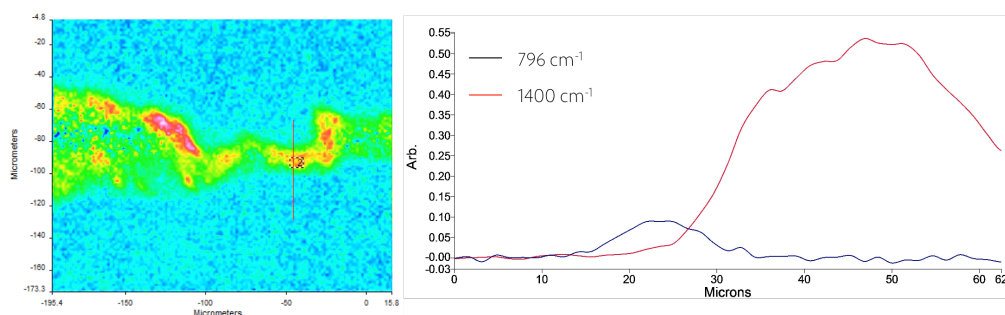


Fig. 5.4: Line profile location and result of the chalk and orpiment cross-section kept at 43% relative humidity for 10 months.

5.2 Analysis of the cross-section of orpiment and earth ground

The SEM image of the orpiment and earth ground cross-section is presented in Fig. 5.5. Two layers are distinguished. The one on top, identified with EDS, is the orpiment layer and the bottom one is the earth ground, based on the presence of silicon and aluminium. Similar to the previous sample, an EDS point analysis was made to the resin to check for impurities. The EDS distribution maps were performed in a smaller area enclosing the interface between these two layers. The maps are presented in Fig. 5.6.

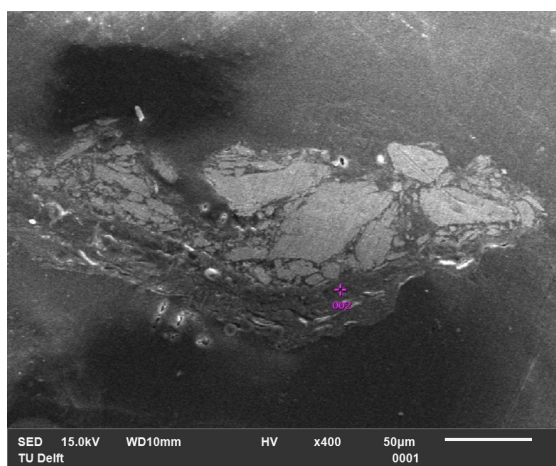


Fig. 5.5: SEM image of the earth ground and orpiment cross-section

Since the earth consists of an aluminosilicate compound, in addition to the elemental maps of arsenic and sulphur, the maps of aluminium and silicon were measured, which as shown in Figures 5.6b and 5.6c. They have the same distribution and are marking the interface between the earth ground and the orpiment layer. The arsenic and sulphur map (Figures 5.6d and 5.6e, respectively) match and its limits are well defined. In Fig. 5.6f, the SE image and the maps of arsenic and aluminium were superimposed and no overlap between them is observed.

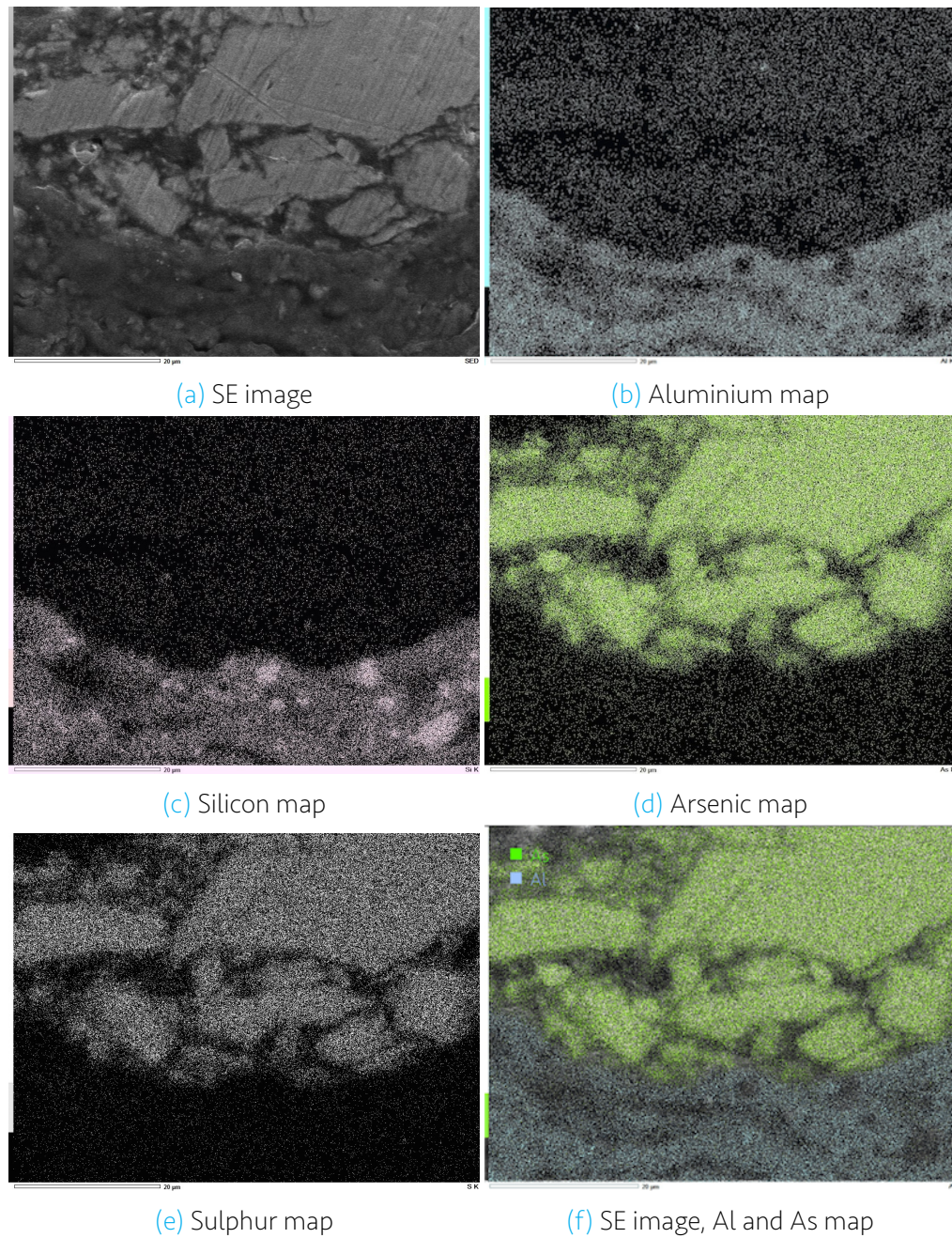


Fig. 5.6: SEM images of the earth and orpiment cross-section kept at 43% relative humidity.

A line profile was made close to the interface and is presented in Fig. 5.7. In this analysis, a continuous line was measured and the relative concentration profiles were superimposed in the SE image. The vertical blue line marks where the line profile was measured. The profile of the arsenic is shown in dark blue in both images. The silicon profile is shown in pink in the left image and the sulphur profile in green in the right image. The right margin of the image represents 0% mass and the left part 100%. As seen in the left image, the profile of the arsenic drops at the interface, which is where the silicon profile rises. However, there is still arsenic detected in the earth ground. Similar to the previous case, it is important to consider the interaction volume of the X-rays detected

with EDS, that might be partly inside the orpiment layer. The sulphur and arsenic profiles, observed in the right image, have the same shape in the orpiment layer, but in the earth ground there are differences between them. There are certain points in which the profiles do not match, which may indicate that the arsenic and sulphur migrate in separate ways, hence showing a different distribution.

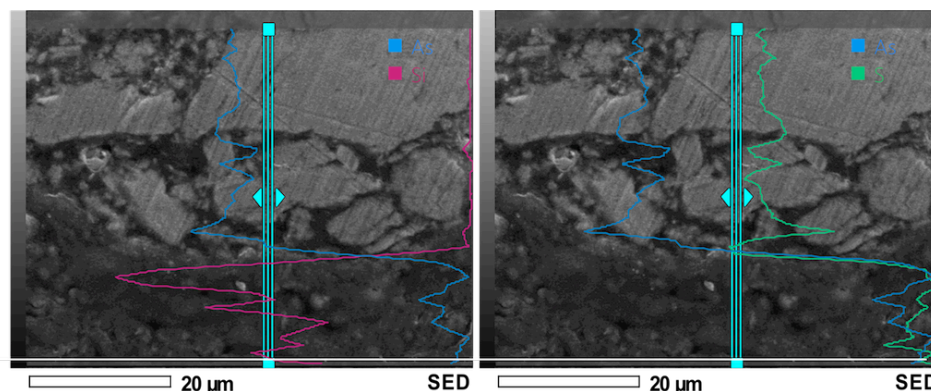
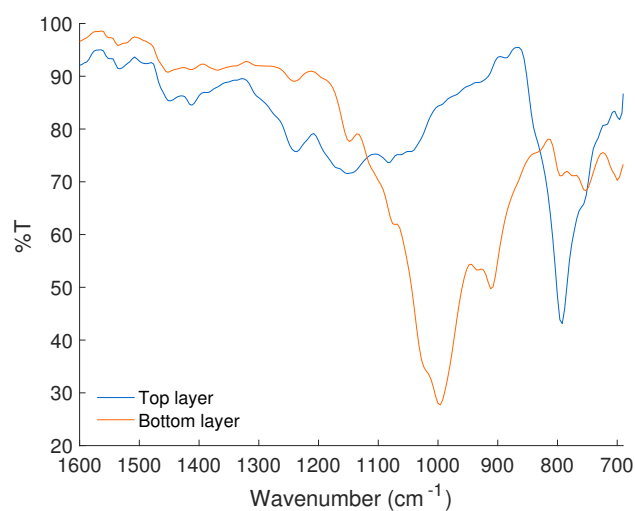


Fig. 5.7: Line profiles of arsenic (blue), silicon (pink) and sulphur (green) at the interface of orpiment and the earth ground.

The FTIR microscopy images of this sample are presented in Fig. 5.8. In image 5.8a, the spectra measured in the top layer shows a peak in 797 cm^{-1} characteristic of the As-O bond. The bottom layer spectra has a peak in 996 cm^{-1} characteristic of the earth ground. This distribution of these peaks are shown in Figures 5.8b and 5.8c. The As-O bond are identified in a higher amount in the outer part of the orpiment and in a lower concentration throughout the orpiment layer. Similarly to the previous sample, the outer part of the layer received more light during the artificial ageing than the inner part of the sample and it has more access to oxygen and water, and thus it shows a higher degree of oxidation.



(a) FTIR spectra

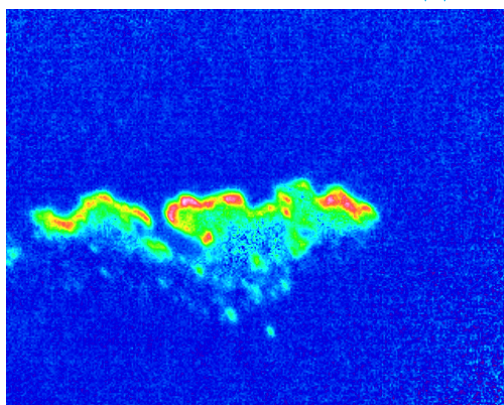
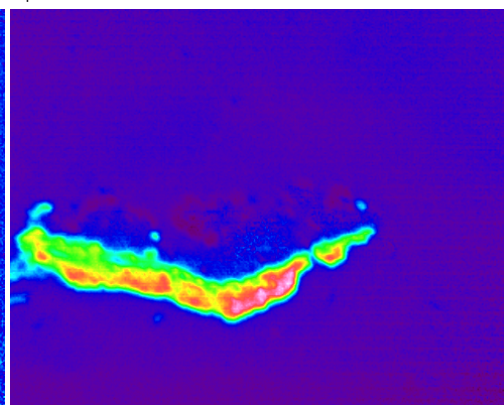
(b) 797 cm^{-1} (c) 996 cm^{-1}

Fig. 5.8: (a): FTIR spectra and (b,c): FTIR microscopy images (red is representative of higher intensity) of the earth and orpiment cross-section kept at 43% relative humidity for 10 months.

A line profile was performed to verify the presence of arsenates in the earth ground (Fig. 5.9). It is observed that in the earth layer, where the intensity of the 996 cm^{-1} peak is high, there is a slight concentration of arsenates. However, the two layers are well separated by an intact orpiment layer (based on the absence of a As-O signal) and thus, no conclusion can be made.

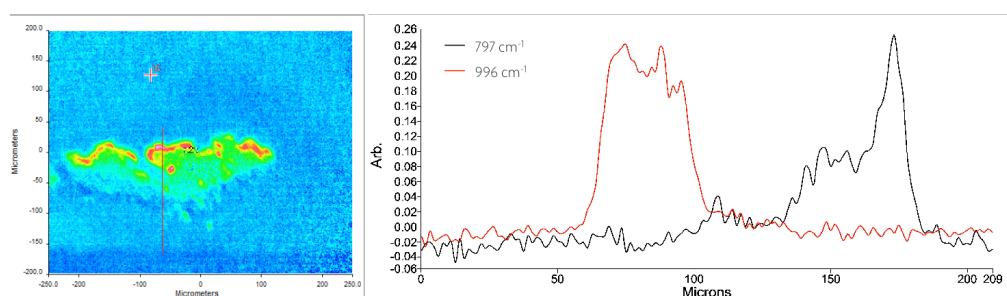


Fig. 5.9: Line profile location and result of the earth and orpiment cross-section kept at 43% relative humidity for 10 months.

5.3 Analysis of the cross-section of orpiment and lead white

The SEM image of the cross-section of orpiment and lead white and the distribution maps of lead, sulphur and arsenic are presented in Fig. 5.10. In the SE image, Fig. 5.10a, the two layers are clearly seen, the top layer being the orpiment and the bottom layer the lead white as identified with a EDS point analysis. As mentioned above, the energy of the characteristic X-rays of lead overlaps with that of sulphur. Since the top layer contains sulphur from the orpiment and the bottom layer contains lead from the lead white, the distribution of sulphur and lead maps of lead and sulphur are the same (Figures 5.10b and 5.10c). The arsenic is distributed in the top layer, its presence is not observed in the lead white layer. In this case, only the SE and the arsenic map were superimposed and it is seen that the arsenic is limited to the top layer. However, there are some parts inside the lead white ground that show arsenic agglomerations. These seem to be gaps in the ground where arsenic may gotten caught during the sample preparation.

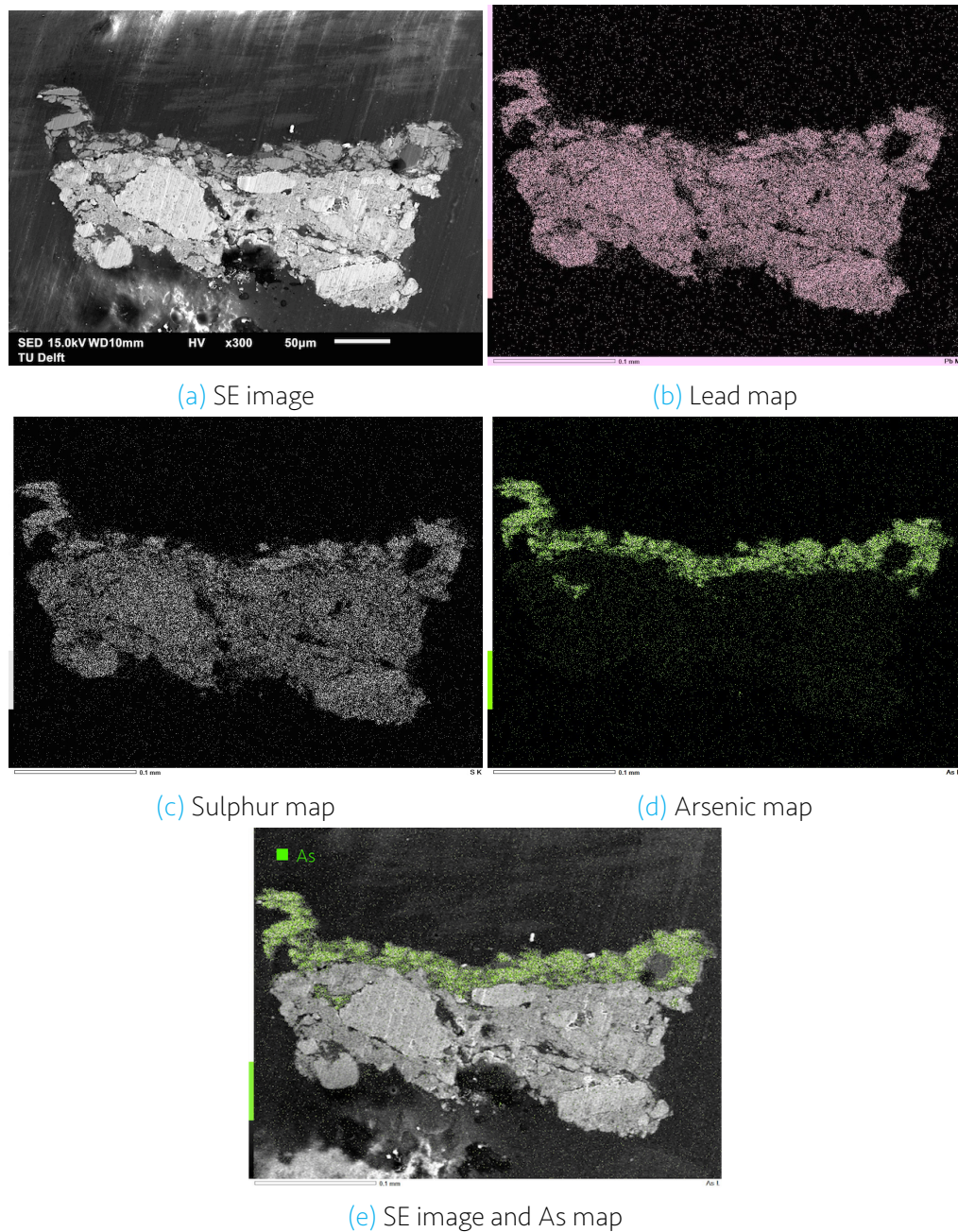


Fig. 5.10: SEM images of the lead white and orpiment cross-section kept at 43% relative humidity.

The line profile of the arsenic is presented in Fig. 5.11. It is observed that the profile decreases when crossing the interface towards the lead white ground. Inside this layer, the arsenic concentration is somewhat higher than the concentration in the resin (on the top of the sample), which may suggest its presence in the ground. However, there is not a concentration gradient to indicate the migration.

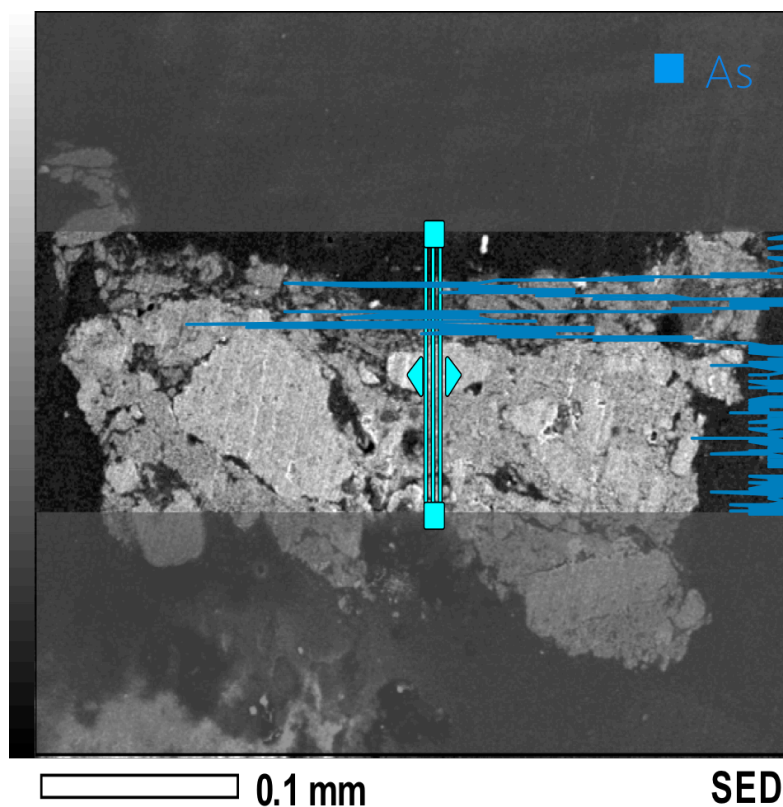


Fig. 5.11: Arsenic line profile at the interface of orpiment and lead white.

The FTIR microscopy images are found in Fig. 5.12. The spectra of the top layer contains the arsenate peak in 797 cm^{-1} , while the spectra of the bottom layer has a peak in 1378 cm^{-1} , characteristic of the C-O vibration of lead white. The distribution maps of these vibrations show that the arsenates are confined to the top layer. Since this layer is thinner than the orpiment layers in the chalk and earth cross-sections, the entire layer shows oxidation products and not an oxidation front. Furthermore, no arsenates were detected in the ground.

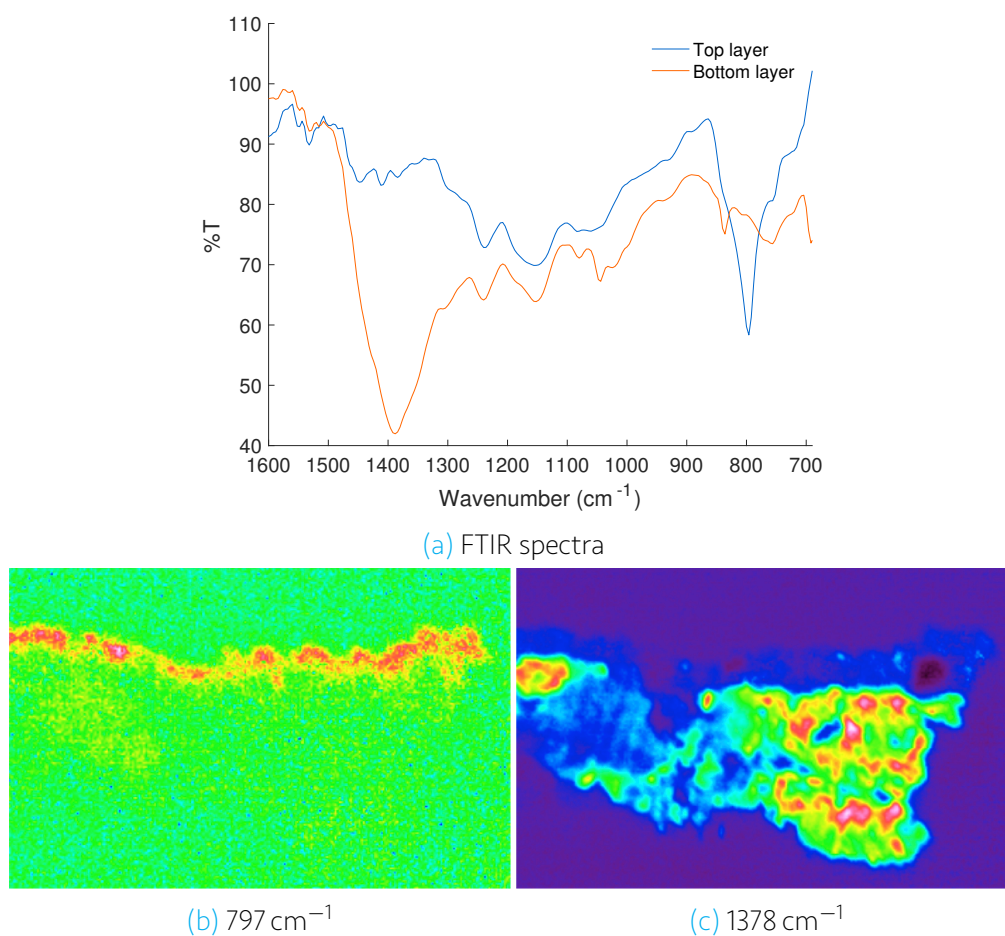


Fig. 5.12: (a): FTIR spectra; (b,c): FTIR microscopy images (red is representative of higher intensity); and (d): line profile; of the lead white and orpiment cross-section kept at 43% relative humidity.

The line profile measured with FTIR microscopy is presented in Fig. 5.13. The arsenic profile does not decrease abruptly to zero as the lead curve increases. Instead, the intensity of arsenic in the interface is slightly above than the intensity measured outside of the sample, where no arsenic is present thus setting the base line. This suggests that some arsenic might have migrated into the lead white layer.

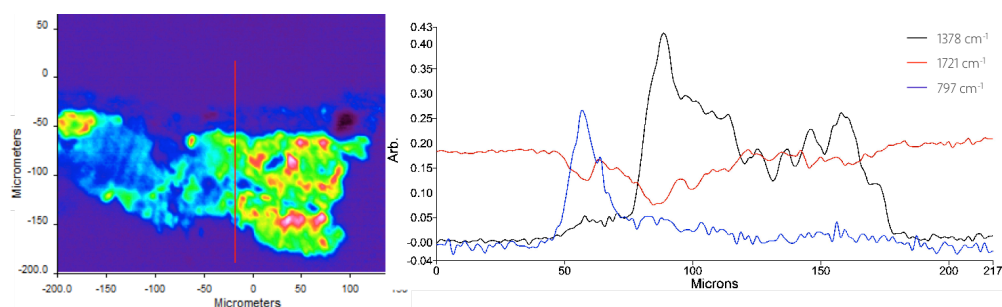


Fig. 5.13: Line profile location and result of the lead white and orpiment cross-section kept at 43% relative humidity for 10 months.

5.4 Discussion

The analysis of the grounds and orpiment cross-sections performed with SEM and FTIR microscopy provided complementary information. Besides being an imaging technique, SEM-EDS allowed to map the distribution of the elements and, through the line profile measurement, to build a concentration profile from one layer to another. The FTIR microscopy provided information about the oxidation of orpiment and complemented the line profile analysis made with SEM-EDS.

In all of the samples, arsenic was detected with both techniques inside the ground layer close to the interface. However, it is not possible to conclude if this is solely a result of the migration of the arsenic into the ground. The interface between two different materials is not perfect. Particularly in this materials where the surface is not completely flat, there is a zone close to the interface where the two materials are mixed. Therefore, the presence of arsenic in a region inside the ground close to the interface is expected. Moreover, the X-rays detected with EDS are produced from a volume below the surface, not only from the surface of the sample, as shown in [Fig. 4.3](#) from [Section 4.1.2](#). This interaction volume may be partly localized in the orpiment layer. Thus, in measurements located in the ground close to the interface, the characteristic X-rays of arsenic may be from the orpiment layer.

Therefore, the low concentration of arsenic close to the interface cannot indicate for a fact that migration of the pigment occurred during the 10 months. It is therefore recommended to keep the samples for a longer time under the different levels of relative humidity and analyse them to check if an increase in the arsenic concentration in the ground was produced.

Nevertheless, there are valuable features that are obtained from this analysis. For instance, the difference in profiles of the sulphur and arsenic in the cross-section containing the earth ground are different as they cross the interface, which may be due to the decomposition of the pigment into arsenates and sulphates.

Furthermore, in the chalk and earth cross-sections studied by FTIR microscopy, an oxidation front is observed in the outer part of the sample. During the light ageing process, the outer part of the sample receives more light than the inner part, which is shielded, showing more oxidation in the outer part of the sample. Additionally, the oxidation of the pigment involves oxygen and water as reactants. Since the outer part of the sample has more access to these two components, it is more prone to oxidise, therefore, creating an oxidation front. Contrarily, the lead white sample is composed of a thinner orpiment layer than the chalk and earth samples. Here light can penetrate across the whole layer inducing the orpiment oxidation and therefore, arsenates were found dispersed in all the orpiment layer. In order to make a more comparative analysis, the thickness of the layers should be as similar as possible and the layers should be as thin as possible. This with the purpose of ensuring the penetration of light into the whole layer and of keeping constant the diffusion of water and oxygen through the layers to promote oxidation across the whole layer.

Chapter 6

Results in-situ

In this chapter, the results of the in situ experiments are presented. First, the characterization of the coatings by ATR-FTIR spectroscopy is introduced. This measurements were performed in order to have the reference spectra of the coatings and monitor its peaks during the experiments. Secondly, the results from the water diffusion analysis by ATR-FTIR spectroscopy are presented, where the diffusion coefficient of water was calculated, and the molecular structure of the coatings was monitored over time. The results of the arsenate diffusion in dammar followed by this later technique are subsequently addressed. Finally, the EIS results of water and arsenic diffusion are shown, in which the diffusion coefficient of water was calculated and the transport of arsenite and arsenate through the different coatings was studied.

6.1 Coatings characterization by ATR-FTIR spectroscopy

First of all, the spectra of the dried coatings was collected to characterize them and have a reference to be able to compare it with the spectra taken at different immersion times. This way, any change in the molecular composition of the coatings will be noted.

The ATR-FTIR spectra of the dried coatings and D₂O is presented in [Fig. 6.1](#). The vibrations of the most representative functional groups is indicated in the figure and the assignment of the specific vibrations for each material is presented in [Table 6.1](#). The assignment for each vibration was based on [\[47, 48, 49, 50\]](#).

The spectra of dammar, mastic and linseed oil is quite similar since they are share the same functional groups (See [Section 2.3.4](#)). The most intense peaks are in the regions 2930-2958 cm⁻¹, 1695-1715 cm⁻¹ and 2865-2875 cm⁻¹ (in order of intensity) and correspond to the hydrocarbon and carbonyl stretching vibrations. A feature that aids the differentiation between oil and the resins is the shape of the carbonyl peak. In the oil, it is a sharp peak due to the ester vibration only and in the resins, there is a broader peak resulting from numerous contributions of CO vibrations in different environments.

The spectra of glue shows the four characteristic vibrations of the amide group: N-H in 3070 cm^{-1} , amide I (C=O vibration of the peptide bond) in 1630 cm^{-1} , amide II (C-N stretching and N-H bending vibrations) in 1550 cm^{-1} and amide III, that depends on the structure of the amide in 1240 cm^{-1} [50].

As mentioned in the previous chapter, there is a shift in the peaks of deuterium oxide compared to those of water. In D_2O , there is a band in 2500 cm^{-1} that correspond to a combination between three vibrational modes: symmetric and asymmetric stretching and bending vibrations; and a less intense peak in 1200 cm^{-1} attributed to the bending vibration [51].

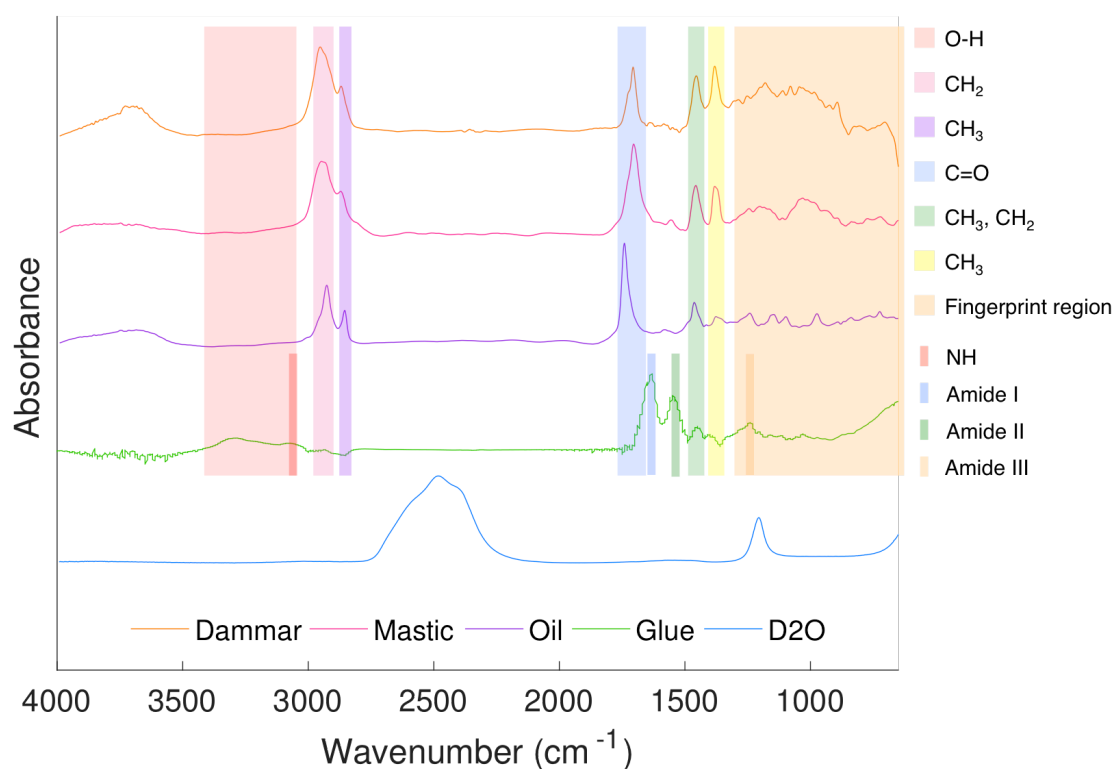


Fig. 6.1: ATR-FTIR spectra of dammar, mastic, linseed oil, glue and D₂O.

Dammar	Mastic	Glue	Oil	Approx. assignment
-	-	3290	-	$\nu(\text{O-H})$
-	-	3070	-	$\nu(\text{N-H})$
-	-	-	3005	$\nu_{\text{a}}(\text{CH}_2)$
2954	2950	2930	2956	$\nu_{\text{a}}(\text{CH}_2)$
2870	2871	-	2925	$\nu(\text{CH}_3)$
1707	1705	-	1741	$\nu(\text{C=O})$ Ester
1641	1645	-	-	$\nu(\text{C=C})$
-	-	1630	-	$\nu(\text{C=O})$ Amide I
-	-	-	1583	$\nu(\text{C=C})$
-	-	1550	-	$\nu(\text{C-N}), \delta(\text{N-H})$ Amide II
1454	1460	1450	1464	$\delta_{\text{a}}(\text{CH}_3), \delta(\text{CH}_2)$
-	-	1410	1415	$\delta(\text{CH}_2)$
1381	1381	1330	1377	$\delta_{\text{s}}(\text{CH}_3)$
-	1244	-	-	$\nu(\text{C-C}), \omega, \tau(\text{C-H}), \nu(\text{C-O-O})$
-	-	-	1242	$\nu_{\text{a}}(\text{C-O})$
-	-	1240	-	Amide III
1180	1180	-	-	$\omega, \tau(\text{C-H}), \nu(\text{C-O-O})$
-	-	1160	-	$\nu(\text{C-O}), \nu(\text{C-O-C})$
-	-	-	1146	$\nu_{\text{a}}(\text{C-O})$
1080	-	1110	1099	$\nu(\text{C-O}), \nu(\text{C-O-C})$
1043	1032	1030	-	$\nu(\text{C-O}), \nu(\text{C-C})$
-	946	-	-	$\omega, \tau(\text{C-H}), \delta(\text{O-H})$
892	-	-	-	$\delta(\text{C-H})$
-	-	-	723	$\gamma(\text{CH}_2), \omega(\text{C-H})$

Table 6.1: ATR-FTIR absorption peaks of dammar, mastic, glue and linseed oil. Frequencies are given in wavenumber [cm^{-1}]. ν : Stretching; δ : bending; ω : wagging; τ : twisting; γ : rocking; a: asymmetric.

6.2 Water diffusion studied by ATR-FTIR spectroscopy

The water diffusion through the different materials was quantified by ATR-FTIR spectroscopy. The objective of this study is to characterise the materials and gain a better insight into the transport properties, which will in part determine the diffusion of arsenic through them. Additionally, the stability of the materials towards water can be seen since the FTIR spectra gives information about the molecules composing the coating and any change will be visible.

One of the requirements of this technique is that the coatings must have a good adhesion to the ATR-crystal. Unfortunately, this condition is not met by the glue as it detached from the crystal the moment the D_2O was added to the cell. Therefore, only the results of dammar, mastic and oil are presented in this chapter.

The ATR-FTIR spectra of the coatings measured over time is presented in Fig. 6.2. The conditions at which the background spectra is taken, namely the ambient temperature, humidity, temperature of the detector and position of the crystal inside the cell, have a great effect on the sample spectra. It is recommended to take the background as the spectra of the ATR-crystal before it is coated. This way, it is possible to normalize the

peaks taken at the different times with the dry coating and compare the changes between different peaks. However this is not always possible (as in the case of the oil). It is particularly difficult to maintain constant the position of the ATR-crystal inside the cell since it has to be disassembled to coat the ATR-crystal and left in the oven to dry for 12 hours. As an alternative, the spectra may be collected against the already coated ATR-crystal before adding the D₂O. This will suppress the problem of the crystal alignment and will also reduce the effect of variation of the ambient conditions since the background spectra is collected minutes before adding the D₂O and not 12 hours in advance. The disadvantage is that the absorbance of the original peak is not known and thus, subsequent spectra cannot be normalized with respect to that peak.

The spectra of dammar and mastic (Fig. 6.2a and 6.2b, respectively) was taken against a background consisting of only the ATR-crystal and thus, the peaks of the coating and water show positive absorbance values. With time, water penetrates inside the coating and occupies the free volume of the coating. As a consequence, the peaks of the coating show lower intensities as the water diffuses through. Contrarily to dammar and mastic, the baseline of the spectra of the oil against the background of the ATR-crystal taken 12 hours before showed large deviations from a linear behaviour. As mentioned before, this may be caused by a temperature differences or a different alignment of the ATR-crystal in the cell. Therefore, the alternative method was used, in which the spectra was taken against a background of the ATR-crystal already coated. As a consequence, the baseline has a more linear behaviour than the spectra collected against the background containing only the ATR-crystal. Furthermore, it can be seen that compared to the spectra of dammar and mastic, the oil spectra has less variations in the baseline and it is more linear (Fig. 6.2). Another important difference is that the change in the coating peaks as water diffuses appear as negative absorbance values since they have a lower intensity than the original spectra.

The spectra of the coatings taken throughout the experimental time were compared to the reference spectra presented in Section 6.1. All of the peaks identified in the reference were present in the coatings, and no additional peaks were found except for the D₂O peaks located in 2500 cm⁻¹ and 1200 cm⁻¹, which indicates that there were no major changes in the molecular structure of the coatings. However, a broadening of the ester peak located near 1700 cm⁻¹ in the spectra of the oil was observed, indicating the presence of carboxylic acids. This is described in more detail in Section 6.2.3.

Even though the baseline of the spectra varies with time, it is possible to see an increase in the D₂O peaks with time (at 2500 cm⁻¹) for the three coatings. It is however difficult to visualize the change in the peaks of the coatings since the baseline is not constant for all the spectra. A baseline correction, which is presented below, must be done to be able to compare them.

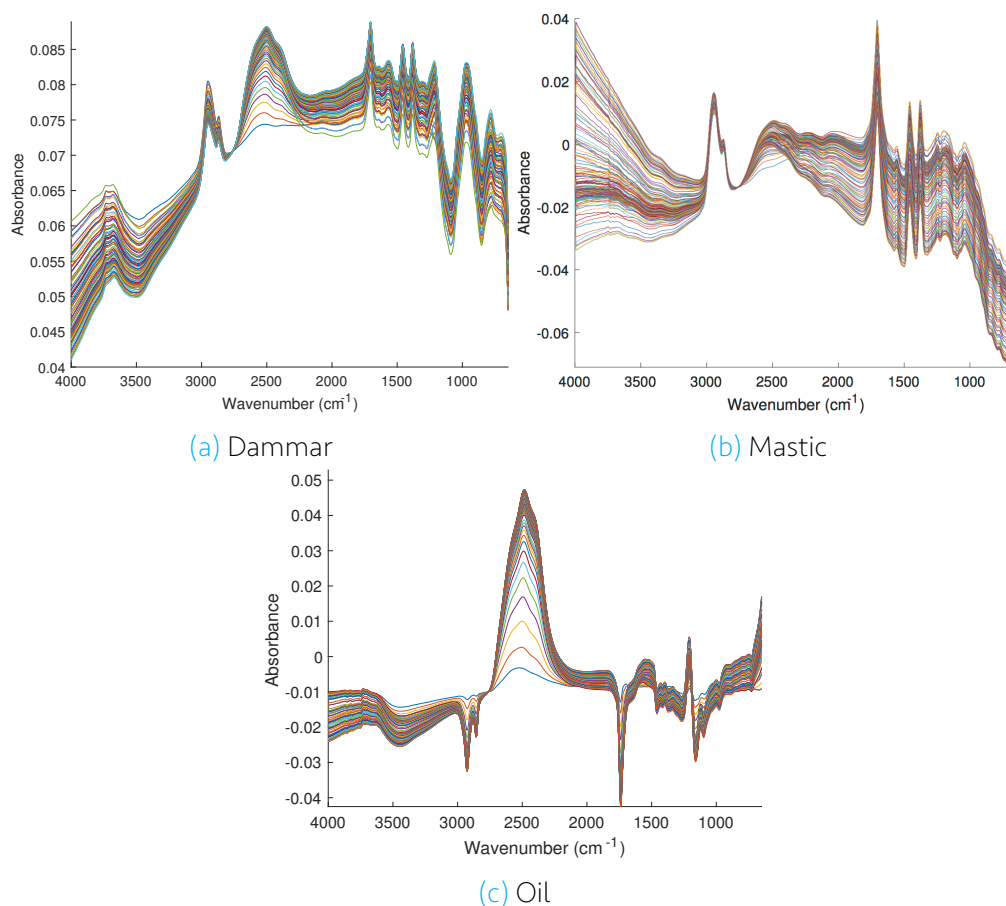


Fig. 6.2: Time-resolved ATR-FTIR spectra of dammar, mastic and oil in D_2O . The time step for taking the spectra is 30 minutes.

For the quantitative analysis, the base line of the spectra was firstly corrected. The approach taken was to correct only the peaks of interest by setting to zero absorbance the base points of the peaks. For example, for the 2500 cm^{-1} D_2O peak, the base points are located in 2800 and 2200 cm^{-1} . A straight line passing through these points was subtracted to the spectra collected at all times. The same procedure was done for the second D_2O peak located in 1200 cm^{-1} in order to have a second estimation of the water diffusion, for the alkane peaks located between 2950 cm^{-1} and 2870 cm^{-1} to have an indication of the water uptake and for the CO peak in 1700 cm^{-1} to monitor the change in the coatings.

The baseline corrected spectra for all materials showing the region where the CH_2 , CH_3 and D_2O peaks are located, is presented in Fig. 6.3. The D_2O is detected since the second measurement, which was taken 30 minutes after the D_2O was added, indicating that there is no time lag for water diffusion as it penetrates the whole thickness of the coating since the beginning. With time, there is an increase in the absorbance of this peak and a decrease in the alkane peaks, as indicated with arrows in Fig. 6.3. The relative absorbance between the D_2O and the alkane peaks gives an indication of the water uptake of the coatings. In dammar, in the last measurements where the coating is saturated with water, the D_2O has a higher intensity than the CH_2 and CH_3 peaks as opposed to mastic, where the alkane peaks are higher. This indicates that there is a higher water

uptake in dammar than in mastic. This observation cannot be made in the oil since the total absorbance of the alkane peaks is not known.

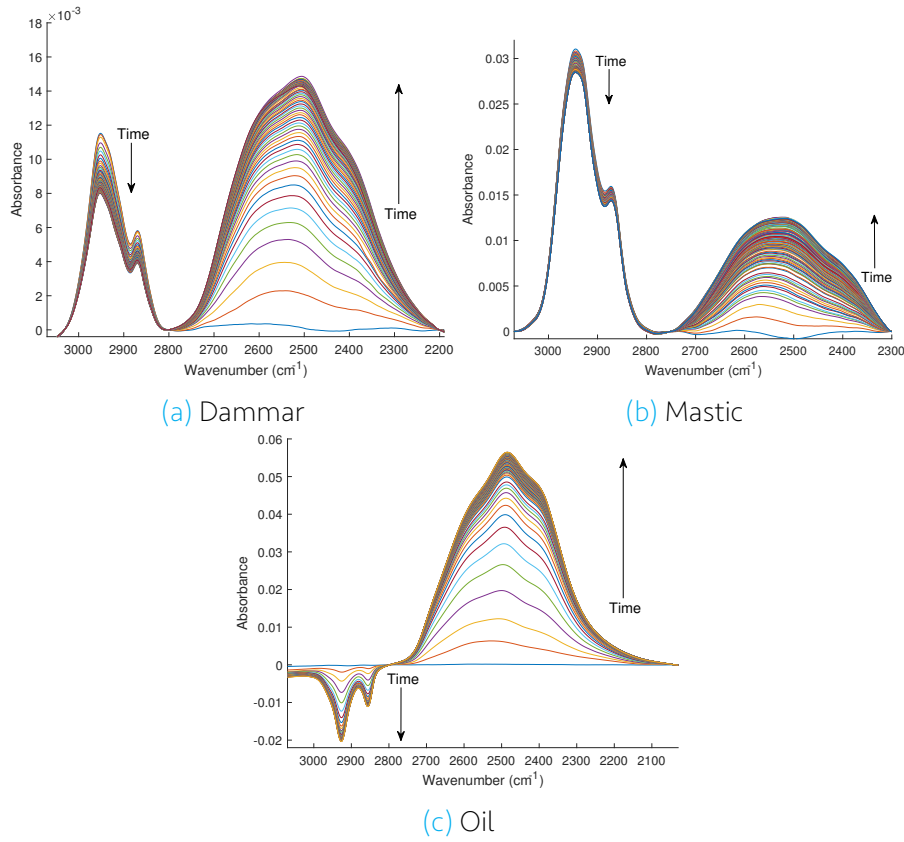


Fig. 6.3: Baseline corrected spectra of dammar, mastic and oil showing the CH₂, CH₃ and D₂O peaks.

To calculate the diffusion coefficient, the absorbance of the D₂O peak was integrated and plotted as a function of time to create a D₂O concentration profile. The integrated absorbance values were normalized by dividing them by the absorbance at equilibrium A_{∞} . Finally, the normalized values were plotted as a function of time and a curve was fitted by the method of non linear least squares with equation 6.1, proposed by Fieldson and Barbari [35] to calculate the diffusion coefficient (for an explanation of the equation see Section 4.2.2).

$$\frac{A_t}{A_{\infty}} = 1 - \frac{8\gamma}{\pi[\exp(-2\gamma L)]} \times \sum_{n=0}^{\infty} \left[\frac{\left[\frac{(2n+1)\pi}{2L} \exp(-2\gamma L) + (-1)^n (2\gamma) \right] \exp\left(\frac{-D(2n+1)^2 \pi^2 t}{4L^2}\right)}{(2n+1) \left(4\gamma^2 + \frac{(2n+1)^2 \pi^2}{4L^2} \right)} \right] \quad (6.1)$$

Where A_t is the measured absorbance at time t , A_{∞} represents the absorbance at equilibrium, γ is the reciprocal of the penetration depth of the infrared radiation d_p , D is the

diffusion coefficient and L is the thickness of the film.

The number of used terms of equation 6.1 was varied to assess the fitting. It was found that there is no further improvement after the 10th term, thus 10 terms were used to fit the equation. A_∞ was estimated by selecting an initial normalized absorbance value from the longer time data of the concentration profile and adjusted to minimize the sum of squared residuals. The penetration depth of the IR was calculated according to equation 6.2, where λ is the wavelength, (generally in FTIR instead of the wavelength, its reciprocal called the wavenumber is used, which is 2500 cm⁻¹ for D₂O), n_1 and n_2 the refractive indices of the ATR-crystal (2.4) and the coatings, respectively and θ is the effective angle of incidence of the beam.

$$d_p = \frac{\lambda}{2\pi (n_1^2 \sin^2 \theta - n_2^2)^{1/2}} \quad (6.2)$$

The effective angle of incidence was calculated with equation 6.3, where θ_f is the angle of the face of the ATR-crystal (60°) and θ_s is the set angle in the instrument (80°). The resulting effective angle is 68.19°.

$$\theta = \theta_f + \sin^{-1} \left[\frac{\sin(\theta_s - \theta_f)}{n_1} \right] \quad (6.3)$$

The refractive index of the coatings is [7]:

- Dammar: 1.515-1.536
- Mastic: 1.535-1.539
- Linseed oil: 1.48-1.49

The penetration depth calculated with equations 6.2 and 6.3 is 0.394 μm for dammar, mastic and glue, and 0.382 μm for oil. Since these values are small compared to the thickness of the coatings (23-70 μm), it is assumed that the measurement is done in the interface between the coating and the ATR-crystal, in other words, the D₂O diffuses through the whole thickness of the coating, where it is analysed.

6.2.1 Dammar

The ATR-FTIR spectra of dammar collected every 30 minutes is presented in Fig. 6.4a in the region 2800-2200 cm⁻¹. The increase of the D₂O intensity with time is clearly observed indicating the diffusion of D₂O through the coating. The normalized D₂O concentration profile is presented in Fig. 6.4b along with the fitted curve. The D₂O profile shows a typical behaviour of a Fickian diffusion process, where a fast increment is observed in the first 5 hours, followed by a period of slower water uptake from 5 to 20

hours until saturation is reached. The parameters to calculate the diffusion coefficient are: $L = 23 \mu\text{m}$, $d_p = 0.394 \mu\text{m}$ and $A_\infty = 4.4$. The calculated diffusion coefficient of D_2O in dammar is $0.11 \times 10^{-9} \text{ cm}^2 \text{ s}^{-1}$ with a R^2 of 0.9956.

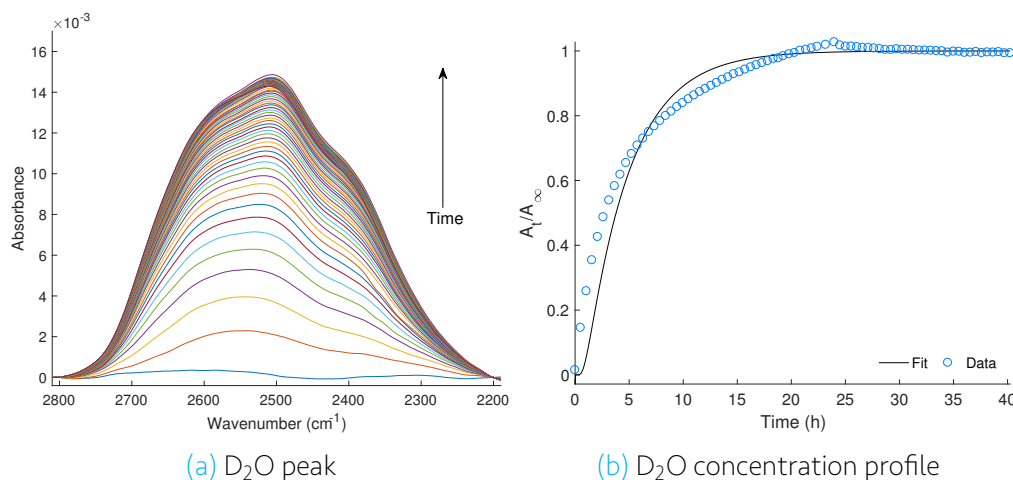


Fig. 6.4: (a) ATR-FTIR time resolved spectra of dammar in the 2800-2200 cm^{-1} region and (b) normalized integrated absorbance of the D_2O peak as a function of time.

The diffusion coefficient was also calculated with the D_2O peak localized in 1200 cm^{-1} obtaining a result of $0.15 \times 10^{-9} \text{ cm}^2 \text{ s}^{-1}$, which is consistent with the result from the 2500 cm^{-1} peak. The D_2O peak and concentration profile are presented in [Appendix A](#) and a summary of these results is presented at the end of this section in [Table 6.2](#).

Additionally, the carbonyl peak located in 1700 cm^{-1} was integrated. This peak was analysed because it gives information about the coating and its possible changes during the experiment. The concentration profile of this peak is presented in [Fig. 6.5](#). In the same figure, the concentration profile of D_2O is also presented to facilitate the comparison.

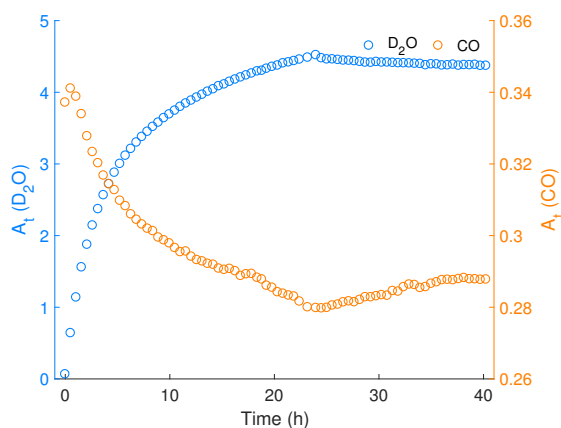


Fig. 6.5: Concentration profiles of the C=O and D_2O peaks in dammar.

As seen in the figure above, there is a decrease in the absorbance of this peak as time passes. The decrease rate of the C=O peak is the same as the increase rate of the D_2O .

In other words, the profiles are the same but inverted. This means that water diffuses through the coating until the interface where it is detected, and thus the D_2O peak increases. Gradually, it fills the volume that used to be occupied by the coating alone until it is saturated. Therefore, the absorbance of the carbonyl peak decreases with time at the same rate as the water diffuses through and it stops decreasing when saturation is reached.

6.2.2 Mastic

Similarly, the diffusion coefficient of D_2O in mastic was calculated. The D_2O peak is presented in Fig. 6.6 along with the normalized concentration profile. During the first hours of immersion there is a fast water uptake. Between 5 and 10 hours the curve smooths and tends to a saturation value, just as in dammar. However, this value is never reached (at least within the experimental time). Instead, there is still a constant water uptake.

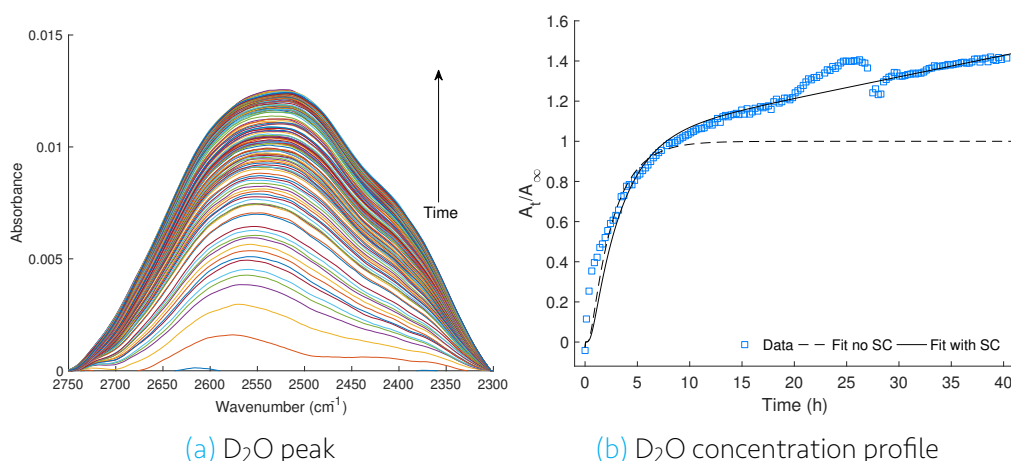


Fig. 6.6: (a) ATR-FTIR time resolved spectra of mastic in the 2800-2200 cm^{-1} region and (b) normalized integrated absorbance of the D_2O peak as a function of time and fitted curves of Fickian diffusion (dotted) and considering a SC (solid).

This type of profile is characteristic of a "two-step" sorption. The first step is a fast Fickian absorption, controlled by a concentration gradient. The second is a non-Fickian diffusion that involves the response of the polymer to a swelling stress. This phenomenon was described by Berens and Hopfenberg by studying the diffusion of various solvents in poly(vinyl chloride) and polystyrene by gravimetric analysis [52]. In the beginning, the solvent diffuses through pre-existing spaces between the polymeric chains. As a response, there is a rearrangement of the chains of the polymer (swelling) and free volume is created. This allows more water to penetrate and explains the constant water uptake seen after longer exposure times.

Another contribution to describing the phenomenon was made by van Westing, who studied the water uptake of epoxy coatings by electrochemical impedance spectroscopy.

He proposed to add a swelling coefficient (SC) to the diffusion equation (See [Section 4.2.3](#)) that linearly depends on time to account for this phenomenon [44]. The equation proposed by van Westing is shown as equation 6.4. Later, Nguyeng Dang, also performing EIS measurements, found that making this swelling coefficient linear with the square root of time and inversely proportional to the thickness (equation 6.5) was in better agreement with the experimental data [53].

$$\phi_t = \phi_s \left[1 - \sum_{n=0}^{\infty} \frac{1}{(2n+1)^2} \exp \left(\frac{-(2n+1)^2 D \pi^2}{4L^2} t \right) \right] + SC \cdot t \quad (6.4)$$

$$\phi_t = \phi_s \left[1 - \sum_{n=0}^{\infty} \frac{1}{(2n+1)^2} \exp \left(\frac{-(2n+1)^2 D \pi^2}{4L^2} t \right) \right] + \frac{SC}{L} \sqrt{t} \quad (6.5)$$

where ϕ_t is the volume fraction of water absorbed at time t , ϕ_s is the volume fraction of water absorbed at saturation and L is the thickness of the coating.

In this project, the ATR-FTIR diffusion equation (6.1) was adapted by incorporating the swelling coefficient from the EIS equation described by Nguyen, which results in equation 6.6. This is proposed based on the idea that the change in absorbance is analogous to the change in capacitance in EIS and that the incorporation of such coefficient provides a better description of the experimental data.

$$\begin{aligned} A_t = & A_{\infty} \left(1 - \frac{8\gamma}{\pi [\exp(-2\gamma L)]} \right) \\ & \times A_{\infty} \sum_{n=0}^{\infty} \left[\frac{\left[\frac{(2n+1)\pi}{2L} \exp(-2\gamma L) + (-1)^n (2\gamma) \right] \exp \left(\frac{-D(2n+1)^2 \pi^2 t}{4L^2} \right)}{(2n+1) \left(4\gamma^2 + \frac{(2n+1)\pi}{2L} \right)} \right] \\ & + \frac{SC}{L} \sqrt{t} \end{aligned} \quad (6.6)$$

It is important to note that there are other two possible explanations of the increasing D_2O concentration at longer exposure times. The first one is explained as a partial detachment of the film from the ATR-crystal. Although no visual evidence of this was encountered during the experiment, it is possible that the coating lost adhesion due to the penetration of D_2O and thus, the D_2O peak keeps increasing with time. The second hypothesis is that the saturation is never reached. In the first hours, the water penetrates into the coating filling the free volume between the molecules. Depending on the arrangement of the molecules, it may be more restricted spaces for the water to penetrate, which will show a slower water uptake explaining the second step of the concentration profile. However, it is not possible to distinguish with FTIR-ATR which one, or what combination, of these mechanisms is the cause of the two-step sorption profile.

Nonetheless, the concentration profile was fitted with equations 6.1 and 6.6. The deviation from the normal Fickian diffusion is shown in [Fig.6.6b](#). The dotted line is the fit

considering a normal Fickian diffusion using equation 6.1 while the solid line represents the fit done with equation 6.6 considering the swelling of the coating. The A_{infy} was estimated the same way as that for the Fickian diffusion calculation but the initial value was chosen as the value where the curve starts to bend towards saturation (approximately at 7 hours) even though it is never reached.

It is evident that the fitting of a Fickian diffusion is poor. In fact, adding a swelling coefficient, increases the R^2 from 0.3522 to 0.9989. The diffusion coefficient calculated by considering a swelling coefficient is $0.23 \times 10^{-9} \text{ cm}^2 \text{ s}^{-1}$. The parameters used to calculate the coefficient are presented at the end of this section in Table 6.2.

The deviation of the data between 20 and 28 hours is attributed to the incorrect functioning of the detector due to a deficiency on the supply of liquid nitrogen needed for cooling as the nitrogen feed of the FTIR is not continuous and must be done manually. Thus, the above mentioned values were not considered in the diffusion coefficient calculation. The analysis of the D_2O peak located in 1200 cm^{-1} was not possible since there is an overlap between this peak and the peaks of mastic.

One way to check the behaviour of the coating is to analyse how the peaks of the coating change with time. For this, the CO peak was integrated and plotted as a function of time Fig. 6.7. Ignoring the incorrect data points mentioned above, a clear tendency is seen. There is a fast decrease in the absorbance of the CO peak in the first 10 hours followed by a slower but constant decrease. This profile corresponds to the two-step sorption observed for D_2O . Unlike the dammar, in this case the coating peak keeps decreasing instead of reaching a saturation value, which confirms, but cannot distinguish between the swelling, partial detachment, or continuous water uptake of the coating.

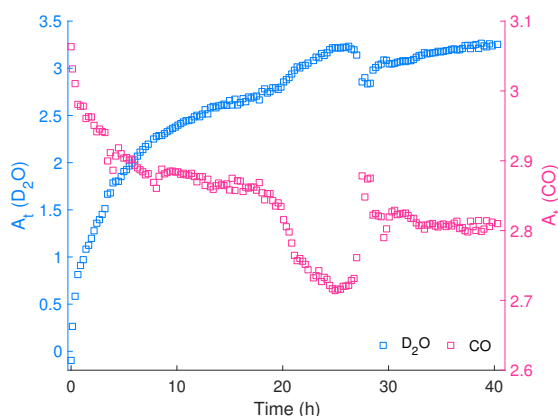


Fig. 6.7: Concentration profiles of the CO and D_2O peaks in mastic.

6.2.3 Oil

The D_2O peak and normalized concentration profile is presented in Fig. 6.8. In this case, a "two-step" profile is also observed. In the first 5 hours there is a fast water uptake, then the curve tends to stabilize but there is a constant D_2O flux at longer times deviating the curve from a purely Fickian diffusion to a non-Fickian diffusion that describes

the swelling of the polymer. Contrary to mastic, the oil coating showed partial detachment from the ATR-crystal after the experiment was performed, which could also explain the increment of the D₂O intensity at longer times. Unfortunately, with this technique is not possible to distinguish whether the increment is caused by swelling or by the detachment of the coating. Nevertheless, the diffusion coefficient was calculated with both equations (Fickian diffusion 6.1 and with a swelling coefficient 6.6). Although the results are similar: $2.82 \times 10^{-9} \text{ cm}^2 \text{ s}^{-1}$ for Fickian diffusion and $2.72 \times 10^{-9} \text{ cm}^2 \text{ s}^{-1}$ with the incorporation of a swelling coefficient; the latter curve shows a better fit (R^2 of 0.9998 versus 0.8547 without the SC).

The diffusion coefficient was also calculated with equation 6.6 based on the peak in 1200 cm^{-1} obtaining a value of $2.13 \times 10^{-9} \text{ cm}^2 \text{ s}^{-1}$. The D₂O peak and concentration profile are presented in Appendix A.

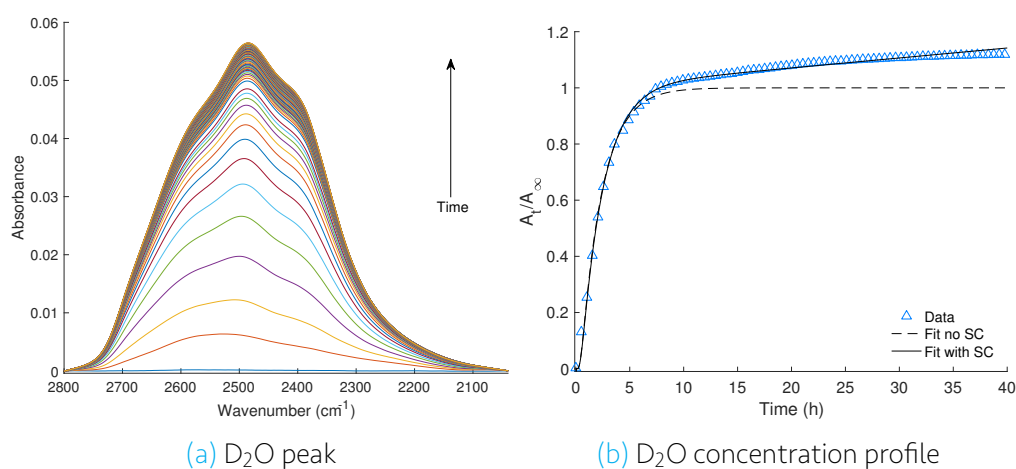


Fig. 6.8: (a) ATR-FTIR time resolved spectra of Oil in the $2800\text{--}2200 \text{ cm}^{-1}$ region and (b) normalized integrated absorbance of the D₂O peak as a function of time and fitted curves of Fickian diffusion (dotted) and considering a SC (solid).

Finally, the C=O peak was analysed. In the dry oil, this is a sharp peak that corresponds to the C=O vibration of esters. However with time, the shape of the peak changes. A broadening of the peak is observed in Fig. 6.9a. This is caused by the presence of carboxylic acids, whose C=O vibration is located at slightly lower wavenumbers (1685 cm^{-1}). This indicates that there is a hydrolysis reaction of the ester groups present in the oil with water to form carboxylic acids [54].

The concentration profile of the CO peak is presented in Fig. 6.9b along with the profile of D₂O. The same behaviour as mastic is observed in oil. There is a fast decrease in the absorbance of the CO peak, which corresponds to the increase of the D₂O absorbance followed by a slower and less noticeable decrease. The two steps corresponding to a Fickian diffusion and swelling or detachment of the coating are clearly visible in this figure confirming the hypothesis made in the diffusion coefficient analysis.

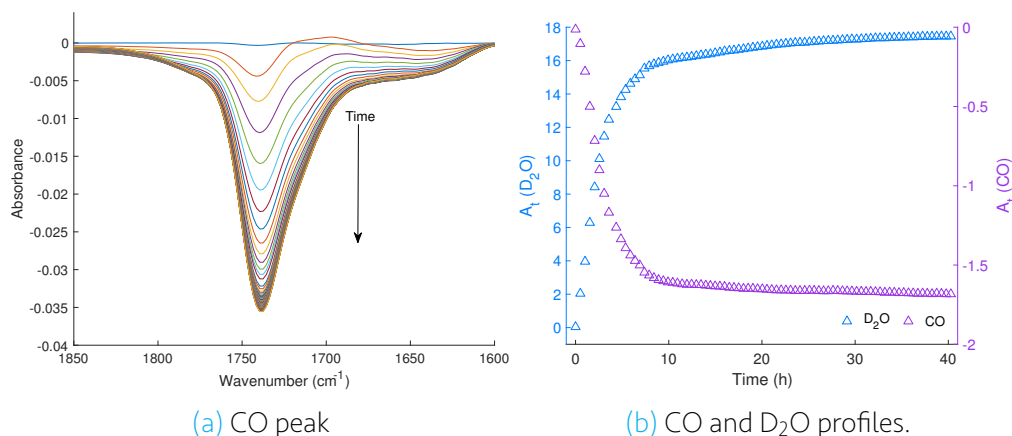


Fig. 6.9: CO peak and concentration profiles of the CO and D₂O peaks in oil.

6.2.4 Discussion

The concentration profile of D₂O in all the coatings is presented in Fig. 6.10. In mastic and oil, the curve shows a faster increase than dammar in the first hours of immersion, indicating a faster water uptake of the dry coatings. It is important to keep in mind that the thickness of the coatings is different. The films of dammar and mastic are 23 and 24 μm respectively and therefore can be compared to one another as seen in the figure. However, the oil film is 70 μm , which means that if a film of 23 or 24 μm was tested, the curve would increase much faster than how is showed in the plot, which is consistent with the calculated diffusion coefficient values.

At longer times, the curves of mastic and oil keep increasing, contrary to dammar where a saturation value is reached. This may be explained by the three phenomenons described above: the swelling of the coating followed by more D₂O penetration, the detachment of the coating from the ATR-crystal or the heterogeneous water diffusion through the coating. However, no conclusions can be drawn on the true cause for the concentration increase after saturation.

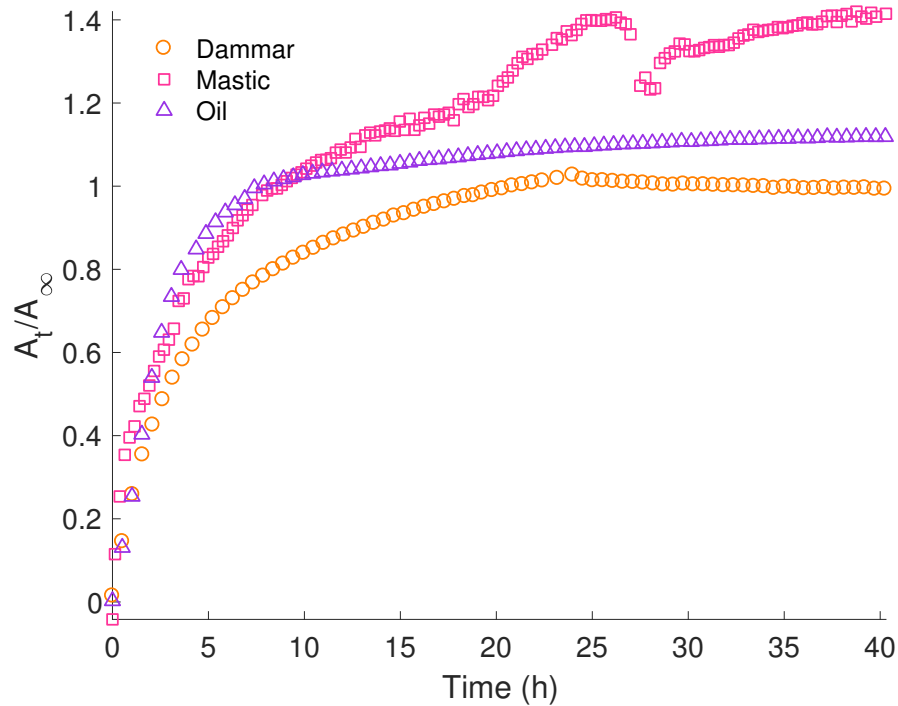


Fig. 6.10: Normalized D₂O concentration profiles of dammar, mastic and oil.

The second aspect is the magnitude of the diffusion coefficients, presented in Table 6.2 along with the parameters used for such calculation. The values for these particular materials is not reported in the literature. However, the calculated diffusion coefficients lie within the range of reported values for other materials [35, 55, 56, 57].

Table 6.2: Diffusion coefficients of D₂O calculated for dammar, mastic and oil.

Coating	L (μm)	Peak (cm^{-1})	A_{∞}	$SC \times 10^8$ ($\text{m s}^{0.5}$)	$D \times 10^9$ ($\text{cm}^2 \text{s}^{-1}$)	R^2
Dammar	23	2500	4.40	-	0.11	0.9778
		1200	0.24	-	0.15	0.9992
Mastic	24	2500	2.30	-	0.29	0.3522
		2300	2.30	1.183	0.23	0.9989
Oil	70	2500	15.6	-	2.82	0.8547
			15.6	27.73	2.72	0.9998
		1200	0.50	-	2.19	0.9057
			0.50	13.60	2.13	0.9999

As shown in Table 6.2, the diffusion coefficient of dammar calculated from the two D₂O peaks is similar (0.11 and $0.15 \times 10^{-9} \text{ cm}^2 \text{ s}^{-1}$) with an R^2 of the fitting the curve above

0.97. For this material no swelling or detachment was observed. Dammar and mastic are similar compounds made of the same type of molecules. In fact, the diffusion coefficient of these two varnishes is similar. However, there is an important difference in their behaviour when immersed in water. In mastic, a saturation plateau was not reached within the experimental time. The diffusion coefficient calculated by considering a swelling coefficient produces a better fit (R^2 of 0.9989) compared to a Fickian diffusion (R^2 of 0.3522). This phenomenon was further studied with EIS and the results are presented in the next section. The same behaviour is observed in the oil in the analysis of the two peaks of the D_2O . In both, the incorporation of a swelling coefficient improves the fitting of the data. The diffusion coefficient of D_2O in oil is one order of magnitude larger than those in the varnishes. A more thorough discussion is presented in [Section 6.6](#).

6.3 Water diffusion studied by EIS

The water diffusion through the coatings was also followed by EIS measurements. The purpose of using EIS is firstly because it provides a different way to measure the water diffusion coefficient and thus, the values calculated with ATR-FTIR spectroscopy can be compared; and second because it gives additional information about the coating properties, as well as the water uptake. As EIS gives information about the interfaces and the processes taking place in the interface, properties such as detachment of the coating from the substrate, water uptake of a coating, diffusion through the coating and swelling can be studied. In this section, the results of water diffusion through dammar, mastic and linseed oil are presented.

6.3.1 Dammar

The Nyquist and Bode plots of dammar at different times are presented in [Fig. 6.11](#). At all times, the shape of the Nyquist plot ([Fig. 6.11a](#)) seems to contain one semi-circle. This shape of is maintained over time, it is only the value of the impedance that change. Its diameter, which is associated with the total impedance of the system, decreases during the first 6 hours from approximately 4.5×10^7 to $1.5 \times 10^7 \Omega$, after which the decrease is less noticeable.

In the Bode plot, the impedance magnitude $|Z|$ shows two plateaus. In general, a plateau is representative of a resistance, since it has no dependency with the frequency and the phase angle is 0° . In this system, one plateau is located at the high frequency limit (10^5 Hz), that corresponds to the resistance of the solution and the second one at low frequencies (10^{-2} Hz), which represents the sum of all the resistances in the system. At intermediate frequencies, a capacitive behaviour is observed, characterized by its dependency with the frequency. The same decrease of the impedance with time is seen in this Bode plot at low frequencies, where the total magnitude $|Z|$ decreases in the range from 10^8 to $10^7 \Omega$. This may be linked to the penetration of water through the

coating. As water diffuses through, it creates channels in the coating that facilitate the ionic current flow between the electrodes, lowering the impedance. It can also be associated with a degradation of the coating. For further analysis, the individual parameters were calculated and are presented in the following paragraphs.

Despite of the observation made about the Nyquist plot containing only one semi-circle, in the Bode plot (Fig. 6.11b) the evidence of a second semi-circle is observed, characterized by two regions with different phase angles, a feature that becomes more evident at longer times. These two semi-circles are typical for a circuit containing two time constants (a resistance connected in parallel with a capacitance) besides the resistance of the solution. The circuits containing one and two constants are presented in Fig. 6.12 along with a schematic drawing of its physical meaning.

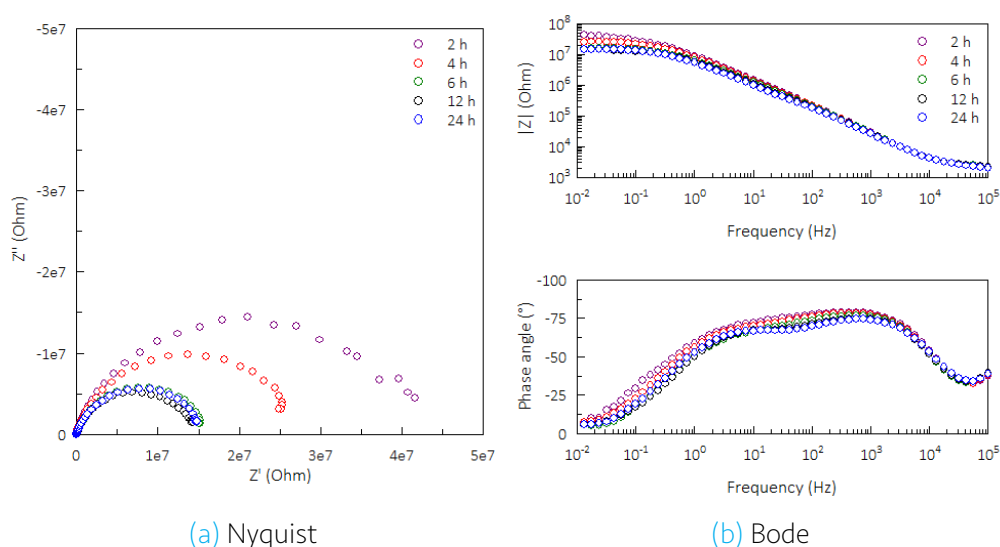


Fig. 6.11: EIS plots of dammar at 2, 4, 6, 12 and 24 h in a Na_2SO_4 solution.

The features observed in the Nyquist and Bode plots are associated to the physical system in the following manner: the impedance at higher frequencies is associated to the resistance of the solution. This resistance is connected in series with the first time constant, that consists of the coating capacitance in parallel with the coating resistance. If a second time constant is considered, it would represent the charge transfer resistance and the double layer capacitance.

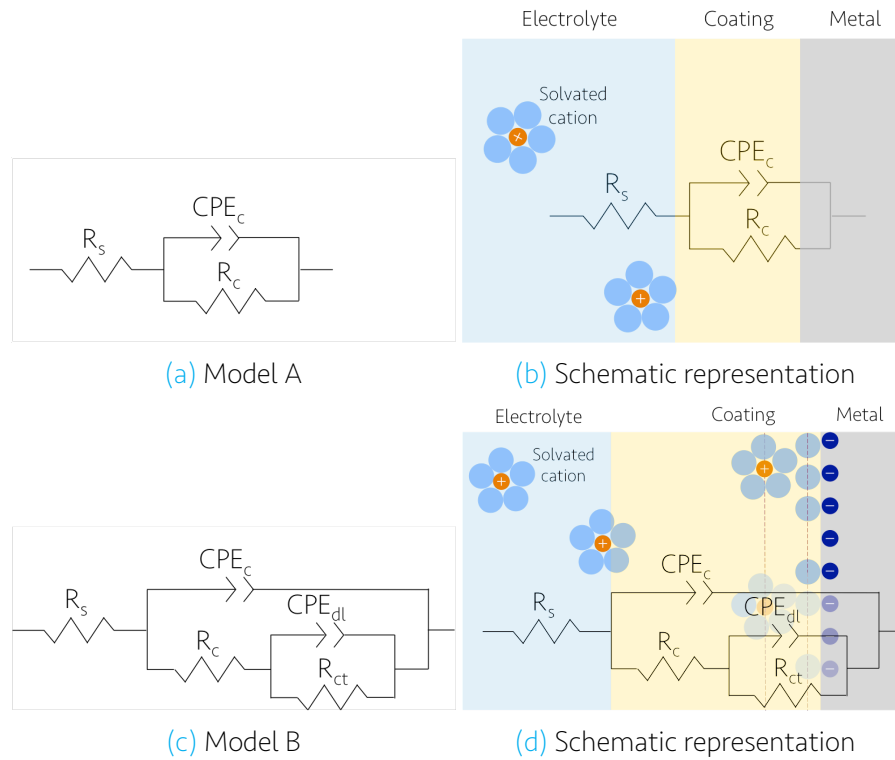


Fig. 6.12: Equivalent circuits proposed to fit the EIS data of dammar.

The coating capacitance was extracted from the data and further treated to calculate the water uptake and diffusion coefficient. As discussed previously in Section 4.2.3, there are 2 different approaches to calculate the capacitance. The first one is to calculate the capacitance from the Bode plot at a frequency of 1000 Hz (C_{HF}). However, in this case this is not possible since the phase angle is not exactly 90° and thus the behaviour is not ideal and a pure capacitance cannot be calculated. The other approach is based on fitting the data to an equivalent circuit and extract the capacitance. Since the shape of the curves is not clear, two equivalent circuits were explored to fit the data, Model A and Model B, with one and two time constants respectively. These models are presented in Fig. 6.12. Since the behaviour of the coating capacitance, as well as the double layer capacitance, are not ideal, a CPE element was used in the models instead of a capacitance. In model A, R_s is the solution resistance, CPE_c is the coating capacitance and R_c is the resistance of the coating. In model B, apart from R_s , R_c and CPE_c , the capacitance of the double layer CPE_{dl} and the charge transfer resistance R_{ct} are included.

Fig. 6.13 shows the result from fitting both models to the experimental data taken at an immersion time of 2 hours. As seen in the Nyquist and the phase angle Bode plot, a better fit is obtained with model B. This is the case for the data obtained at all immersion times. Therefore, a double layer capacitance and a charge transfer resistance appear since the first measurements. This suggests that water diffuses through the whole thickness of the coating from the beginning forming a double layer that grows as more water reaches the interface. This is in accordance with the experiments performed with ATR-FTIR, where the water was detected from the first instance.

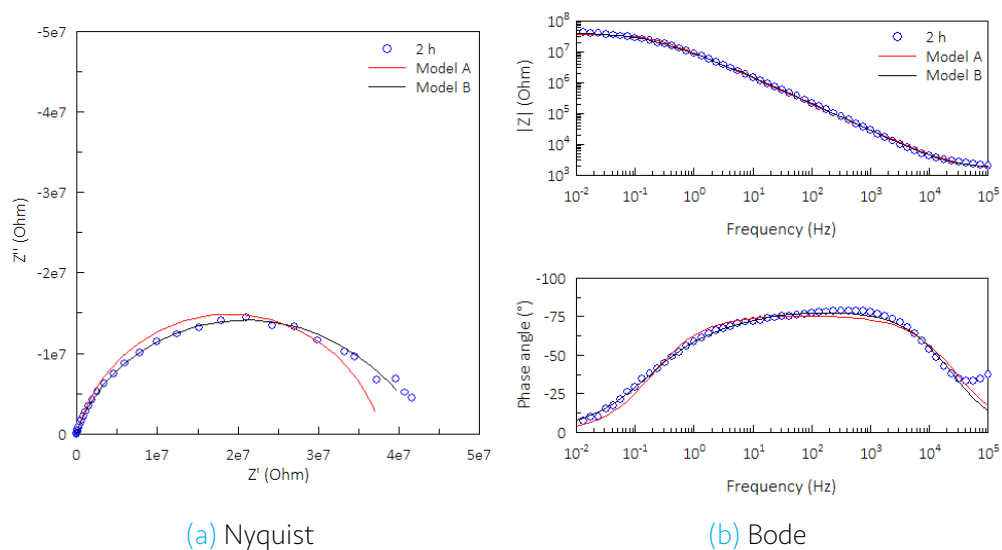


Fig. 6.13: Fitting curve with models A and B to the EIS data of dammar taken at 2h.

It is important to mention that at very high frequencies, there is a deviation of the data from the model (Fig. 6.14). This has been encountered by several authors and is attributed to an instrumental artefact [58]. Therefore, the fitting was made discriminating the frequency range from 4×10^4 to 1×10^5 Hz.

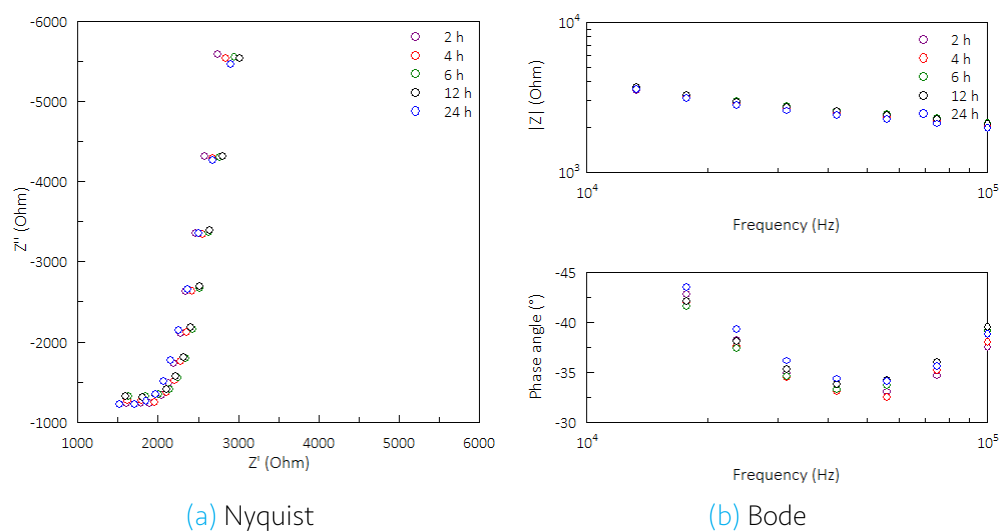


Fig. 6.14: High frequency region of the EIS plots of dammar at 2, 4, 6, 12 and 24 h in Na_2SO_4 .

The numerical results from fitting model B to the data for selected hours are shown in Table 6.3. The fitted data at all times was plotted as a function of time and is shown in Fig. 6.15, while the numerical values and the errors associated with every value can be found in Appendix B. One way to test the goodness of fit of the model is with the chi-squared (χ^2) value. A lower value of χ^2 indicates a better fitting of the model to

the data. As shown in the Table 6.3, the χ^2 is around 0.0023. Compared to the χ^2 obtained by fitting with model A (0.015), it is much smaller confirming that model B describes the data better than model A. Except from the resistance of the solution, the errors of the individual parameters are below 6.5%, which are common errors in this kind of measurements. The errors associated to the resistance of the solution are about 30% and will be discussed below.

Table 6.3: Selected EIS data of dammar calculated with Model B.

Time (h)	χ^2	R_s (Ω)	R_c (Ωcm^{-2})	CPE_c ($\text{Fcm}^{-2}\text{s}^{\alpha-1}$)	α_c	R_{ct} (Ωcm^{-2})	CPE_{dl} ($\text{Fcm}^{-2}\text{s}^{\alpha-1}$)	α_{dl}
0.5	0.0023	1976	9.75×10^6	5.76×10^{-9}	0.90	7.27×10^7	8.30×10^{-9}	0.62
2	0.0022	1917	6.70×10^6	5.60×10^{-9}	0.90	1.03×10^8	6.37×10^{-9}	0.58
4	0.0023	1980	6.10×10^6	5.96×10^{-9}	0.89	6.18×10^7	6.08×10^{-9}	0.67
6	0.0027	1992	4.54×10^6	6.73×10^{-9}	0.88	3.47×10^7	7.50×10^{-9}	0.72
12	0.0023	1933	2.44×10^6	7.50×10^{-9}	0.87	3.40×10^7	7.70×10^{-9}	0.70
18	0.0018	1814	3.10×10^6	8.22×10^{-9}	0.86	3.87×10^7	7.09×10^{-9}	0.71
24	0.0018	1774	2.25×10^6	8.06×10^{-9}	0.86	3.62×10^7	8.02×10^{-9}	0.73
40	0.0016	1601	1.31×10^6	8.62×10^{-9}	0.87	8.06×10^7	7.94×10^{-9}	0.71

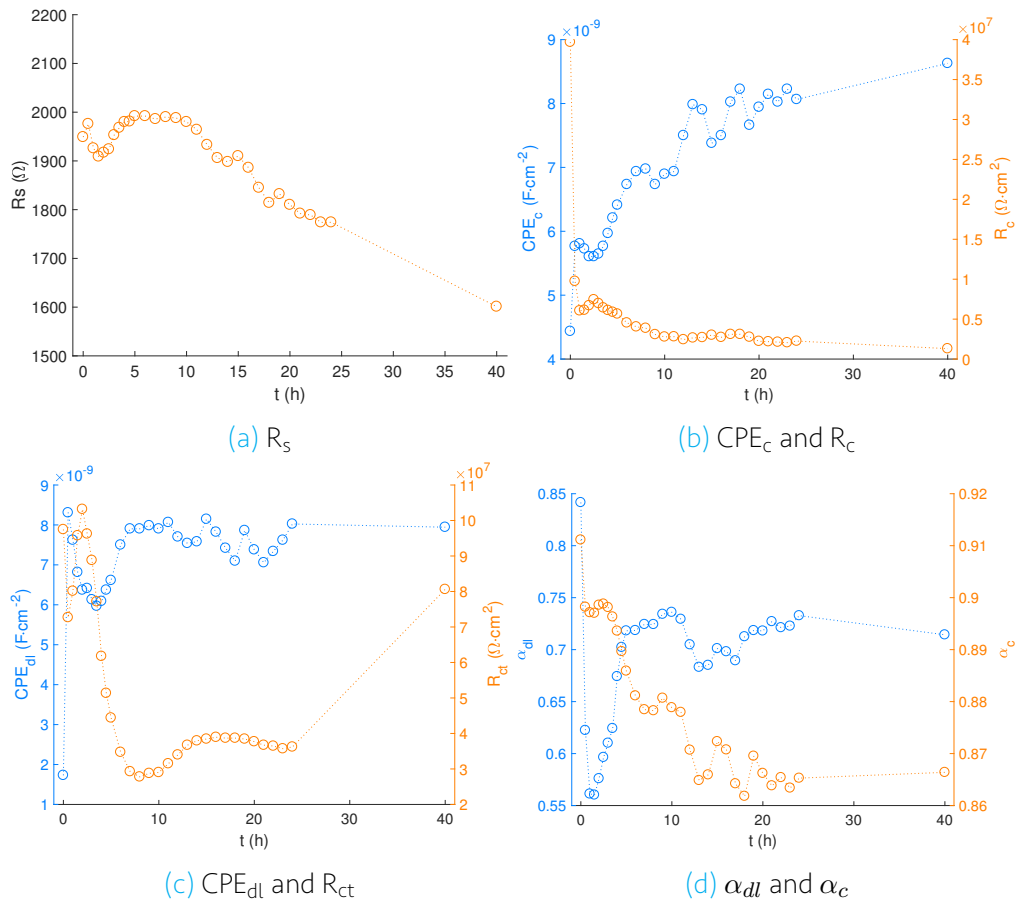


Fig. 6.15: Plots of the results from fitting the EIS data of dammar as a function of time.

The first aspect to notice in the plots is the solution resistance (Fig. 6.15a). During the first 10 hours it is relatively stable. However, at longer times it decreases, possibly due to evaporation of the water during the experiment. The magnitude is higher than expected. The electrolyte used was a solution 0.01M of Na_2SO_4 and its conductivity was measured before and after the experiment, obtaining 2.45 and 2.05 mS cm^{-1} , respectively. The resistance of a solution can be calculated with the following equation:

$$R = \frac{d}{\kappa A} \quad (6.7)$$

where R is the solution resistance, d is the distance between the working electrode and the reference electrode, κ is the conductivity of the solution and A is the area through which the current flows.

An estimation of the resistance of the solution was made. The distance between the electrodes is approximately 4.3 cm and the area was considered to be the exposed area of the working electrode: 2.48 cm^2 . With these parameters, the resistance of the solution before and after the experiment is 846 Ω and 708 Ω , respectively. The values calculated by fitting the model does not correspond to these values. However, they do correspond to the high frequency values in the Bode plot with a $|Z|$ of $10^3 \Omega$ (Fig. 6.11b). This value may be influenced by the high frequency artefact and therefore, does not allow a proper calculation of the resistance of the solution. This is reflected in the errors associated to the resistance of the solution which are approximately 30%.

The CPE of the coating lies within the typical coating capacitance values, which is in the order of nF [36]. As shown in Fig. 6.15b, the CPE of the coating increases with time. Even though there is some dispersion in the data, a trend is observed. During the first hours, the increase is fast and afterwards there is a tendency to saturate to a certain value. The increase of the capacitance is an indication of water penetration. As explained previously, the capacitance is proportional to the permittivity of the media. The permittivity of water is lower than that of the dry coating. Therefore, as water diffuses through the coating, it increases the capacitance until a value in which the coating is saturated with water.

On the other hand, the resistance of the coating decreases rapidly in the first hours and remains constant after 10 hours of immersion. The decrease of the resistance may indicate changes in the barrier properties of the coating. As water diffuses through, it may change the diffusion pathways along the coating facilitating the current flow and thus, decreasing the resistance of the coating.

The charge transfer resistance decreases with time and the double layer capacitance increases with time. Since the R_{ct} is proportional to the electrode area and CPE_{dl} is inversely proportional, this suggests that the double layer is occupying more area as time passes and more electrolyte diffuses to the electrode-coating interface. After 10 hours, the CPE_{dl} is relatively stable, which is the approximate time of saturation of the coating and no more electrolyte is penetrating.

After the data was fitted to the equivalent circuit, the capacitance was further treated to obtain the water uptake and diffusion coefficient. As mentioned before in Section 4.2.3, the calculation with CPE values does not provide true values of water uptake and hence, true diffusion coefficients. Thus, the effective capacitance C_{eff}^H must be calculated. The effective capacitance calculation proposed by Brug relies in a constant solution resistance, which was not the case for this experiment. Therefore, the effective capacitance was calculated by equation 6.8, proposed by Hsu.

$$C_{eff}^H = Q^{1/\alpha} (1/R_c)^{(\alpha-1)/\alpha} \quad (6.8)$$

The calculated effective capacitance is presented in Fig. 6.16. There is more dispersion in the C_{eff}^H data than the CPE by itself since the variations of R_c , CPE_c and α contribute to the dispersion of the effective capacitance. Nevertheless, the same trend observed for the CPE is noticeable.

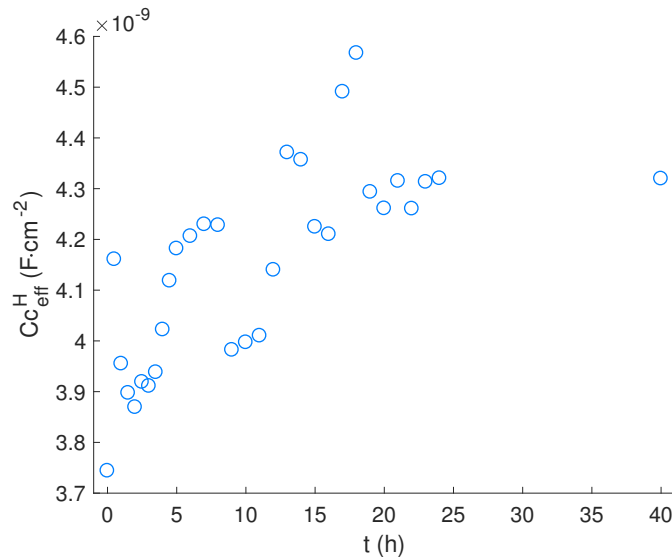


Fig. 6.16: Effective coating capacitance of dammar as a function of time.

The water uptake, $\phi(\%)$, was calculated with the Brasher Kingsbury equation:

$$\phi(\%) = \frac{\log(C_t/C_0)}{\log \epsilon_w} \quad (6.9)$$

where C_t is the effective capacitance (C_{eff}^H) measured at time t , C_0 is the initial coating capacitance and ϵ_w is the permittivity of water, assumed to be 80 at all immersion times. The results are presented in Fig. 6.17a. The diffusion coefficient was then calculated with equation 6.10 by plotting (ϕ_t/ϕ_s) as a function of time.

$$\phi_t = \phi_s \left[1 - \sum_{n=0}^{\infty} \frac{1}{(2n+1)^2} \exp \left(\frac{-(2n+1)^2 D \pi^2}{4L^2} t \right) \right] \quad (6.10)$$

Here, ϕ_t is the water uptake at time t , ϕ_s is the volume fraction of water absorbed at saturation, D is the diffusion coefficient and L is the thickness of the coating. In this case, the thickness of dammar was 43 μm .

The first 10 terms of the equation were used to fit the curve, since beyond the 10th term, the R^2 did not show a significant increase. The fitted curve is presented in Fig. 6.4b. The data points that significantly deviated from the curve were excluded from the fit and are shown in the same figure. The fitting is not ideal, in fact the R^2 is low (0.8655), which is expected due to the dispersion of the data. Nevertheless, it was possible to calculate the diffusion coefficient, obtaining $0.323 \times 10^{-9} \text{ cm}^2 \text{ s}^{-1}$. This value, although not exactly equal, is close to the diffusion of water calculated with ATR-FTIR: $0.106 \times 10^{-9} \text{ cm}^2 \text{ s}^{-1}$ (Found in section 6.2.1).

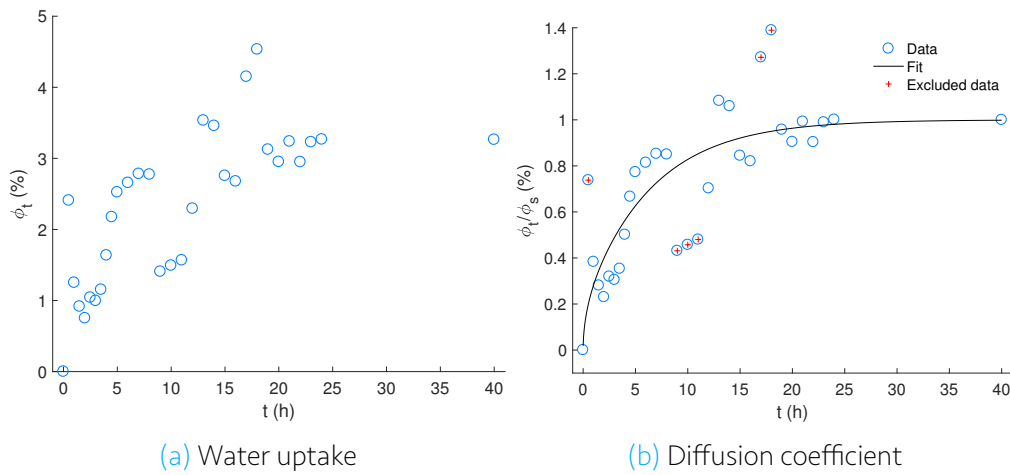


Fig. 6.17: Water uptake and fitting curve for the diffusion coefficient calculation of water in Dammar.

6.3.2 Mastic

The Nyquist and Bode plots of the EIS data of mastic immersed in a Na_2SO_4 solution at different times are shown in Fig. 6.18. In the Nyquist plot (Fig. 6.18a), two semi-circles are observed. Unlike dammar, the two semi-circles here are less overlapped and thus, more clearly visible. Even though this is not so evident in the impedance magnitude $|Z|$ from the Bode plot, the phase angle shows two high angle regions, which confirms the presence of the two semi-circles of the Nyquist plot (Fig. 6.18b).

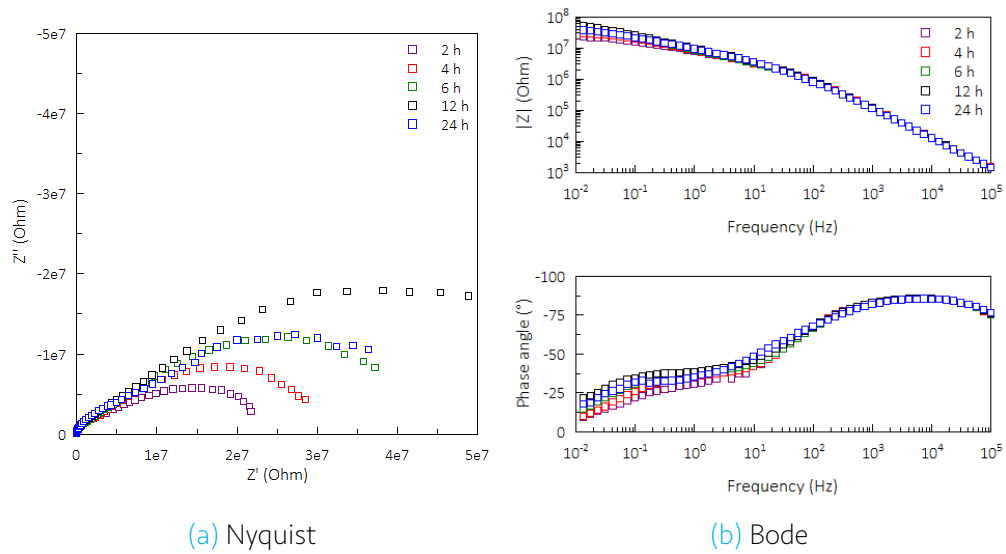


Fig. 6.18: EIS plots of mastic at 2, 4, 6, 12 and 24 h in a Na_2SO_4 solution.

The diameter of the lower frequency semi-circle increases from 2 to 12 hours and then it drops at 24 hours. This behaviour is also observed in the total impedance Bode plot. A close up to low frequencies is shown in Fig. 6.19 to illustrate this behaviour. It is important to note that it is the total impedance of the system the one that is increasing, so it is necessary to estimate the individual contributions of the individual electrical elements to understand the processes taking place in the system. This is done by fitting an equivalent circuit to the EIS data with electrical elements that represent these processes in the physical system.

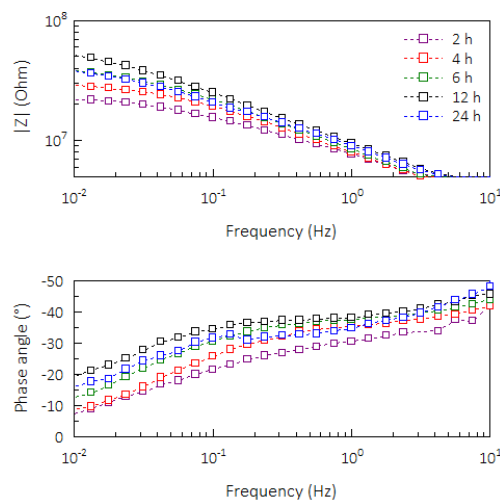


Fig. 6.19: Low frequency region of the Bode plots of mastic at 2, 4, 6, 12 and 24 h.

The two semi-circles observed in the Nyquist plot are characteristic of two time constants. Therefore, model B was proposed to fit the data (Fig. 6.12c). The fitted curves of the data measured at 2 and 24 hours is presented in Fig. 6.21. As can be seen in the figure,

the data at low frequencies deviates from the model. Furthermore, the α coefficient of the CPE_{dl} that resulted from fitting this model is around 0.5, which is characteristic of the presence of a Warburg. In fact, the Warburg can be regarded as a CPE with the imaginary component of the impedance equal to the real component and an $\alpha = 0.5$. Therefore, a Warburg element was incorporated to the model, Model C, and a better fit was obtained.

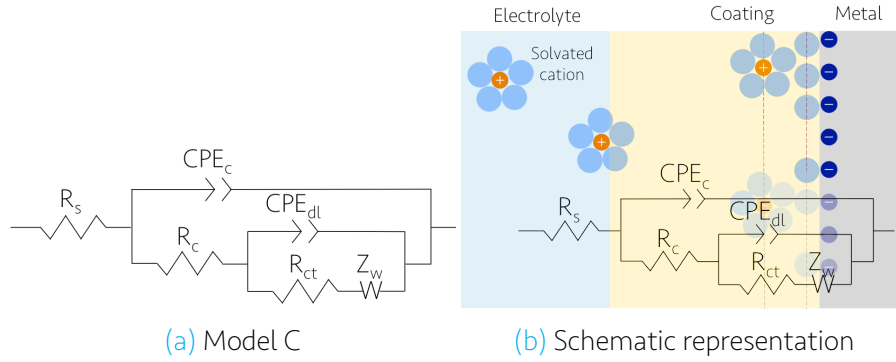


Fig. 6.20: Equivalent circuit proposed to fit the EIS data of mastic.

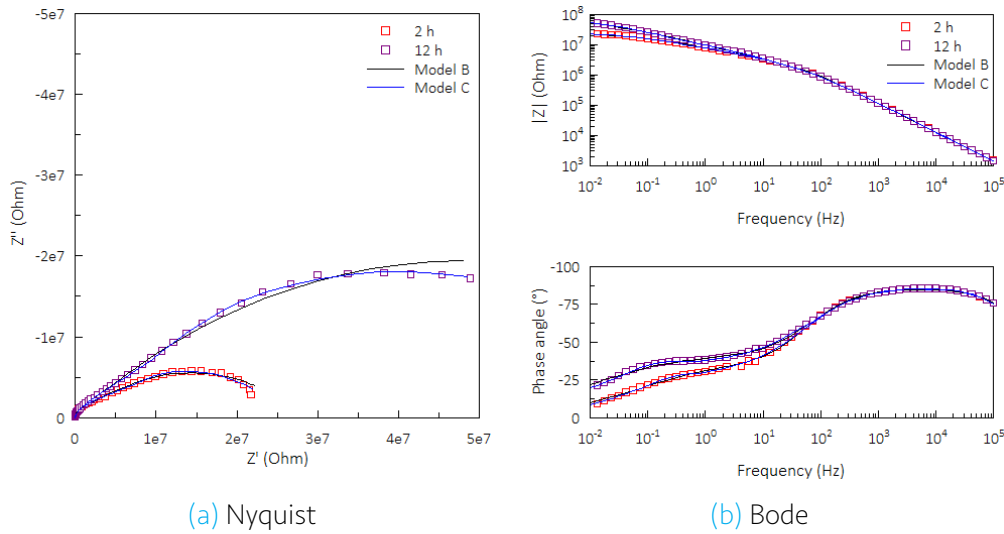


Fig. 6.21: Fitted curves of the EIS data of mastic taken at 2 and 24 hours with models B and C.

The data at all times was fitted with Model C and is presented in [Appendix B](#). Selected data is shown in [Table 6.4](#) and the plots of all the parameters as a function of time is presented in [Fig. 6.22](#). The χ^2 is low at all times, which indicates that the model produces a good fit for all the experimental times. The errors in most of the parameters, also shown in [Appendix B](#), are low except from the resistance of the coating, which after 17 hours the errors of some points are above 8%.

Table 6.4: Selected EIS data of mastic calculated with Model C.

Time (h)	χ^2	R_s (Ω)	R_c (Ωcm^{-2})	CPE_c ($\text{Fcm}^{-2}\text{s}^\alpha - 1$)	α_c	R_{ct} (Ωcm^{-2})	CPE_{dl} ($\text{Fcm}^{-2}\text{s}^\alpha - 1$)	α_{dl}
0.5	0.00058	313.2	3.72×10^6	7.22×10^{-10}	0.97	3.77×10^7	1.88×10^{-8}	0.42
2	0.00048	262.1	4.19×10^6	7.98×10^{-10}	0.96	3.84×10^7	1.71×10^{-8}	0.49
4	0.00041	261.4	4.41×10^6	8.15×10^{-10}	0.96	3.55×10^7	1.48×10^{-8}	0.55
6	0.00020	267.8	3.82×10^6	7.94×10^{-10}	0.96	5.23×10^7	1.50×10^{-8}	0.53
12	0.00018	275.7	3.12×10^6	7.58×10^{-10}	0.96	6.99×10^7	1.42×10^{-8}	0.49
18	0.00016	272.1	1.82×10^6	7.26×10^{-10}	0.97	9.30×10^7	1.28×10^{-8}	0.46
23.5	0.00029	272.6	1.24×10^6	7.18×10^{-10}	0.97	3.70×10^7	1.40×10^{-8}	0.45

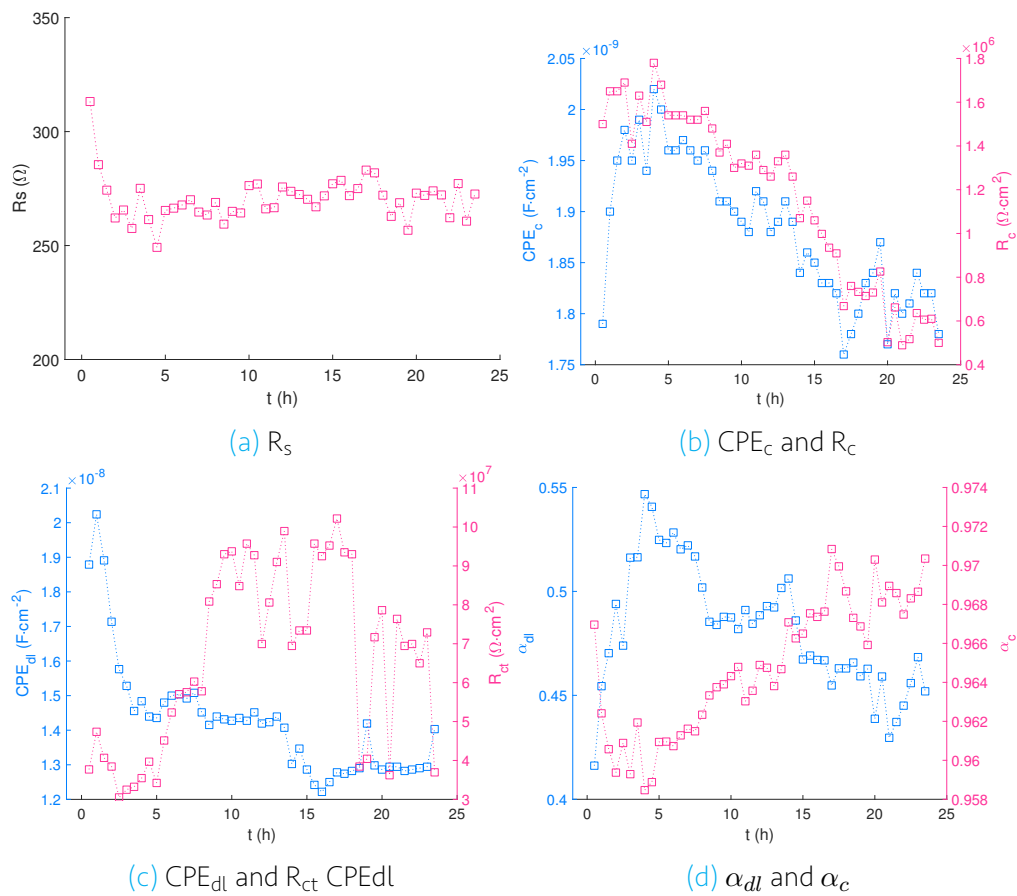


Fig. 6.22: Plots of the results from fitting the EIS data of mastic as a function of time.

As shown in Fig. 6.22a, the resistance of the solution is relatively constant along the experimental time and its magnitude is closer to the one estimated from the conductivity of the solution. In Fig. 6.22b, the capacitance of the coating, represented by a CPE, increases in the first 5 hours and afterwards it decreases with time. The first increase in the capacitance is due to the penetration of water. Same as in dammar, the permittivity of water is higher than that of the coating and, since the capacitance is proportional to the permittivity of the medium, there is an increase in the capacitance as water diffuses through the coating. However, it does not tend saturation value as in

dammar. Instead, there is a pronounced decrease from 5 to 24 hours. As the capacitance is inversely proportional to the thickness of the coating, a reduction of the capacitance could be caused by an increase in the thickness of the coating, in other words, swelling. However, the increase in thickness due to swelling is not as large as to explain the drop in the capacitance. It has been seen from several authors that the swelling of the coating will produce an increase in the capacitance since more water is allowed to penetrate [52, 44, 53, 46, 42]. In this cases, the water uptake, and thus the capacitance, has a two step sorption profile in which there is a fast increase and instead of a saturation plateau, there is a continuous but slower increase.

Another possibility to explain the capacitance decrease is the detachment or partial detachment of the coating. Deflorian et al reported a similar capacitance profile, in which the decrease was attributed to the detachment of the coating [59]. In their situation, this explanation was logical since at the end of the experiment, the coating was completely detached from the electrode. However, the mastic coating did not show any signs of detachment.

Another possible explanation is that the coating may be losing its barrier properties. As water penetrates, it may cause a degradation of the coating making it loose its capacitive behaviour. This is seen as a decrease in the capacitance as observed in Fig. 6.22b. Furthermore, the resistance of the coating decreases, which can also be explained by this reasoning as it is easier for the electrolyte to penetrate.

As shown in Fig. 6.22c, the double layer capacitance decreases with time. The formation of the double layer is a process that takes place in the interface between the metal and the electrolyte. As this interface is changing with time, the double layer capacitance takes time to stabilize, as well as the charge transfer resistance, that on the other hand has a high degree of dispersion.

The diffusion coefficient cannot be calculated since the sample does not show a Fickian diffusion profile. Nevertheless, the effective capacitance and the water uptake were calculated to show the complete set of parameters. The effective capacitance was calculated with equation 6.8 and the result is presented in Fig. 6.23a. The water uptake was calculated with equation 6.9 and presented in Fig. 6.23b. The effective capacitance, just as the CPE increases during the first 5 hours and then decreases with time. The water uptake has the same profile as the capacitance. The only possible conclusion drawn from this graph is that during the first 5 hours, the water uptake of mastic is 1.8%. The diffusion coefficient cannot be calculated since the coating capacitance is not changing only due to the water uptake but it is also related to the properties of the coating. As mentioned previously, a decrease in the capacitance of the coating may be related to a decrease in its barrier properties indicating the degradation of the coating.

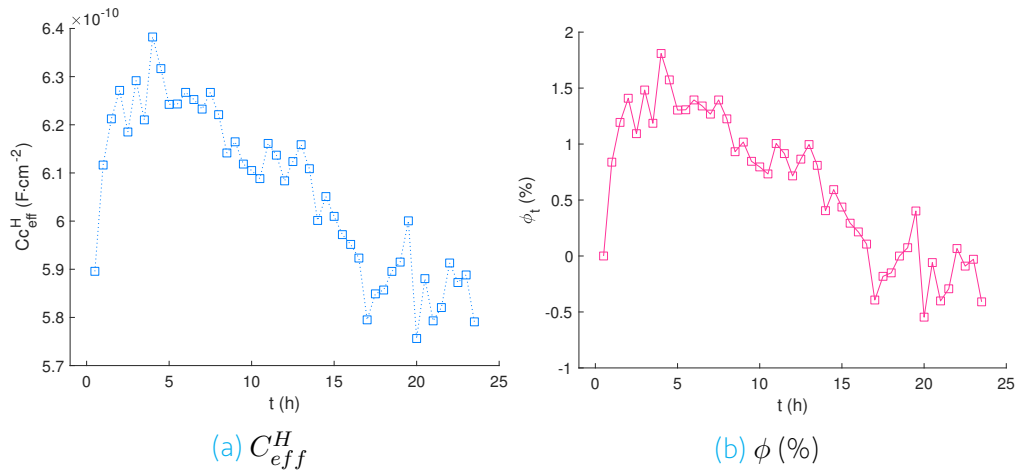


Fig. 6.23: Effective coating capacitance and water uptake of mastic.

6.3.3 Oil

The results of the EIS experiment of oil in the Na₂SO₄ solution are presented in Fig. 6.24. The Nyquist and Bode plots have different shapes than those encountered for dammar and mastic. Here, only one semi-circle is present in the Nyquist plot and it has a tail at low frequencies (Fig. 6.24a). In the Bode plot, the impedance magnitude shows only one plateau and in the phase angle plot, only one region is present (Fig. 6.24b). They both relate to the semi-circle observed in the Nyquist plot.

The diameter of the semi-circle decreases with time, and so as the total impedance $|Z|$. This may be linked to the absorption of water of the coating and the change in pathways building up inside the coating. The tail observed in the Nyquist plot may be caused by a non-ideal Warburg element. In the first measurements, the tail appears to be a pure resistance since the phase angle is close to zero. But with time, the angle increases toward the characteristic 45°, also seen as a straight line with a slope of -1 in the Nyquist plot. This is more clearly seen in the 24 hour measurement presented in the Nyquist plot (Fig. 6.24a). For the analysis of the water uptake and diffusion coefficient, the data was fitted without considering this region with an equivalent circuit containing one time constant.

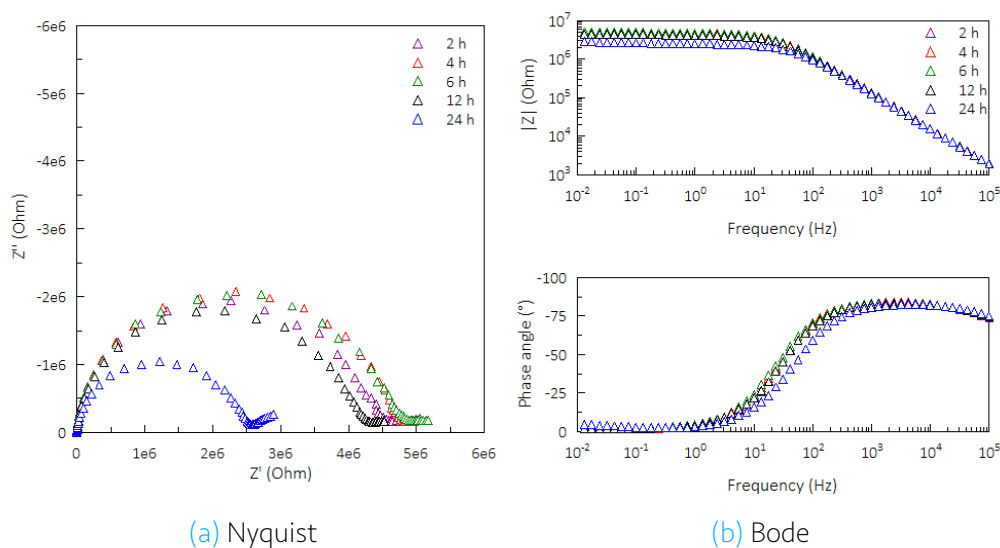


Fig. 6.24: EIS plots of oil at 2, 4, 6, 12 and 24 h in a Na_2SO_4 solution.

To calculate the water diffusion, the EIS data was fitted with model A (Fig. ??), which consists of the resistance of the solution R_s connected in series with a parallel connection between the resistance of the coating R_c and the capacitance of the coating, modelled as a CPE to consider the non-ideal behaviour of the coating CPE_c . A schematic representation of the model is presented in Fig. 6.12b. The fitted curves for the data taken at 2 and 24 hours are presented in Fig. 6.26.

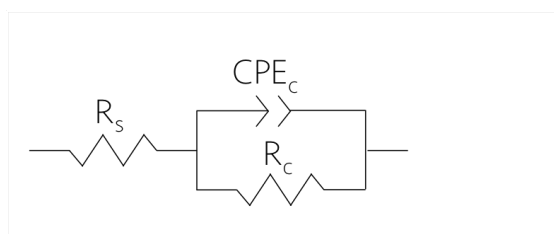


Fig. 6.25: Equivalent circuits proposed to fit the data of mastic.

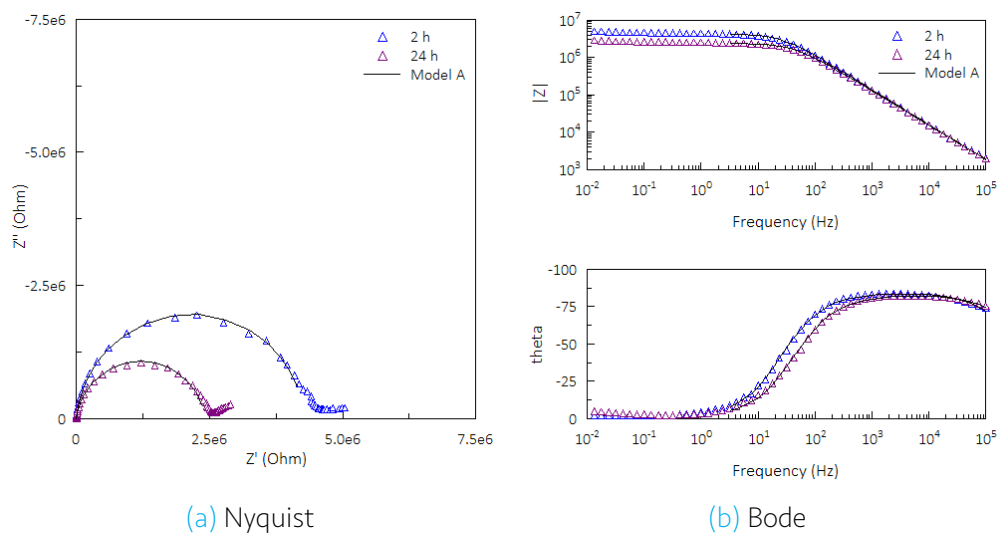


Fig. 6.26: Fitted curves of the EIS data of oil taken at 2 and 24 hours with model A.

Selected values from the fitting are presented in Table 6.5. A table with the complete values can be found in Appendix B. As observed in Fig. 6.26, the model describes well the data. This can also be seen in the value of χ^2 that is approximately 0.001 for all times. The error associated to the individual components is low, below 1.5% except from the resistance of the solution, whose maximum error is 8%. The plots of the individual components as a function of time are presented in Fig. 6.27.

Table 6.5: Selected EIS data of oil calculated with Model A.

Time (h)	χ^2	R_s (Ω)	R_c (Ωcm^{-2})	CPE_c ($\text{Fcm}^{-2}\text{s}^{\alpha-1}$)	α
0.5	0.0024	496	9.67×10^6	7.46×10^{-10}	0.95
2.6	0.0015	427	1.09×10^7	7.82×10^{-10}	0.94
4.1	0.0013	401	1.15×10^7	8.06×10^{-10}	0.94
6.1	0.0011	387	1.15×10^7	8.15×10^{-10}	0.94
12.2	0.0013	368	1.11×10^7	8.39×10^{-10}	0.93
18.3	0.0012	352	1.02×10^7	8.59×10^{-10}	0.93
24.1	0.0012	334	8.83×10^6	8.71×10^{-10}	0.93

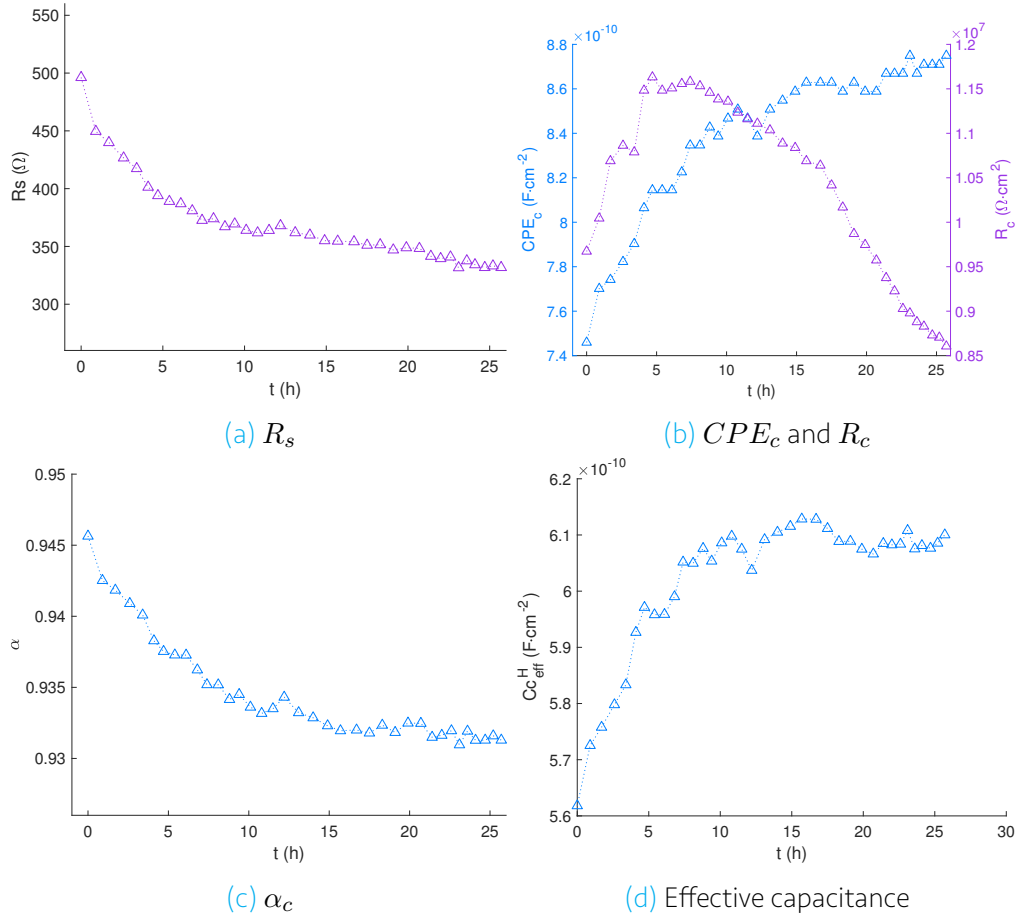


Fig. 6.27: Plots of the results from fitting the EIS data of oil as a function of time.

The resistance of the solution (Fig. 6.27a) decreases throughout the experimental time, which may be caused by evaporation of the solution, same as in dammar. In Fig. 6.27b, the capacitance of the coating, treated as a CPE, is presented. It increases with time due to the diffusion of water through the coating, that changes the permittivity of the medium and as a consequence, the capacitance. The CPE at longer times tends to a saturation value, however it does not reach it at least in the experimental time. This may be an indication of the swelling of the coating.

The resistance of the coating increases in the first hours and then decreases due to water penetration and a change in the diffusion pathways making easier the penetration of water. The CPE coefficient α is close to 1, meaning that the coating behaves almost ideal and it decreases with time as water diffuses through.

The effective capacitance of the coating was calculated with equation 6.8 and presented in Fig. 6.27d. In this case the capacitance of the coating increases rapidly during the first 10 hours and then it tends to a plateau indicating that the coating is saturated with water and no more water can penetrate. By calculating the effective capacitance, the increase at longer times is corrected and a plateau is observed. The water uptake was calculated with the Brasher Kingsbury equation (equation 6.9) and is presented in Fig.

6.28a. It shows a Fickian profile with a maximum water uptake of 1.88% in the saturation region. The diffusion coefficient was calculated with equation 6.10 obtaining a result of $1.124 \times 10^{-9} \text{ cm}^2 \text{ s}^{-1}$. The fitted curve is presented in Fig. 6.28b and has a R^2 of 0.9530. The calculated diffusion coefficient is similar to the one calculated with ATR-FTIR: $2.816 \times 10^{-9} \text{ cm}^2 \text{ s}^{-1}$ (presented in Section 6.2.3).

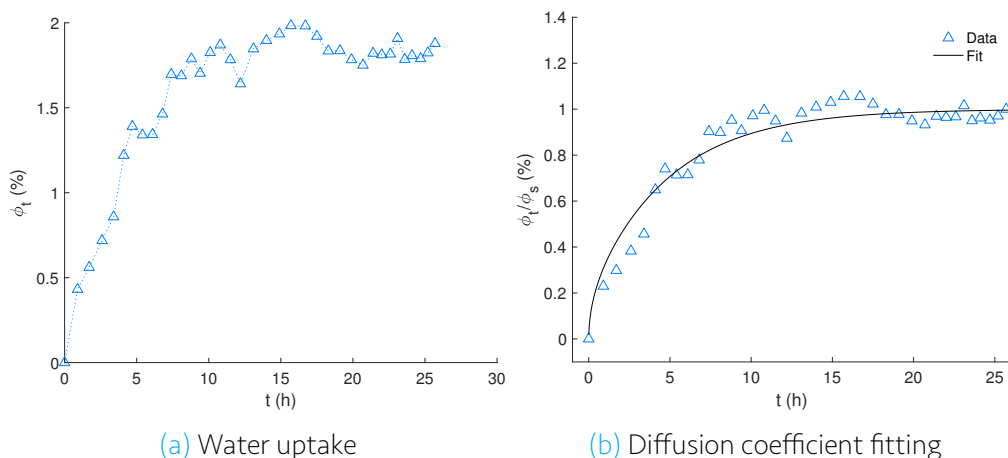


Fig. 6.28: Water uptake and fitting curve for the diffusion coefficient calculation of water in Oil.

6.3.4 Discussion

A summary of the results of water diffusion studied by EIS is presented in Table 6.6. For all the experiments, the electrolyte used was a solution 0.01M of Na_2SO_4 . The first parameter to notice is the calculated effective capacitance of the coating. The C_{eff}^H of dammar is approximately one order of magnitude higher than the capacitance of mastic and oil. This is an indication of the superior barrier properties of dammar over the mastic and the oil. The resistance of the coating is very similar for the three coatings although slightly smaller for mastic, which suggests that the coating opposes less resistance to the diffusing water.

It is observed that the water uptake of dammar is higher than that for mastic and oil, which is also seen in the ATR-FTIR spectroscopy measurements (Section 6.2). Furthermore, the penetration of water through dammar and mastic took place since the beginning of the experiments, which is reflected as the presence of the double layer capacitance in the first measurements.

The diffusion coefficient of water in dammar is smaller than the coefficient in oil and the magnitudes are consistent with those calculated with ATR-FTIR spectroscopy ($0.11 \times 10^{-9} \text{ cm}^2 \text{ s}^{-1}$ for dammar and $2.72 \times 10^{-9} \text{ cm}^2 \text{ s}^{-1}$ for oil).

Table 6.6: Selected EIS data of oil calculated with Model A.

Coating	L (μm)	C_{eff}^H (t=0) (F cm^{-2})	R_c (t=0) $\Omega \text{ cm}^2$	ϕ_∞ (%)	$D \cdot 10^9$ ($\text{cm}^2 \text{ s}^{-1}$)	R^2
Dammar	43	3.74×10^{-9}	9.74×10^6	3.26	0.32	0.8655
Mastic	13	5.89×10^{-10}	3.72×10^6	1.80	-	-
Oil	28	5.61×10^{-10}	9.67×10^6	1.88	1.12	0.9398

6.4 Arsenates diffusion studied by ATR-FTIR spectroscopy

As mentioned in the methodology (Section 4.2.2), three different type of experiments were performed in order to study the diffusion of arsenates through the coatings:

- Aluminium in D_2O
- Aluminium in D_2O + Arsenates
- Aluminium coated with dammar in D_2O + Arsenates

The hypothesis behind this experiments is that the arsenates will diffuse through the coating to reach the aluminium layer and be absorbed. As the arsenates reach the coating-aluminium interface, the bond between the arsenate and the aluminium will be detected and thus, a signal will be observed in the ATR-FTIR spectra. As the concentration of arsenates increases in such interface, so will the intensity in the spectra. Therefore, a concentration profile can be created and the diffusion coefficient calculated with the same equation used to calculate the diffusion coefficient of water (equation 6.1).

6.4.1 Aluminium in D_2O

First of all, the stability of the aluminium layer in D_2O was studied. The ATR-crystal was coated with an aluminium layer and D_2O was added. The ATR-FTIR instrument was programmed to collect spectra every 30 minutes for a period of 24 hours. However, after 5 hours a software error occurred and the following spectra was not collected. Therefore a set of measurements were done after 20 hours up until 30 hours.

The measured spectra showing the region between 650 and 1300 cm^{-1} , which is the region of interest since the arsenate peak is located between 800 and 900 cm^{-1} and the D_2O peak at 1200 cm^{-1} , is shown in Fig. 6.29a. The first thing to notice is the variation of the baseline with time. Specially at lower wavenumbers, the intensity of the spectra

increases. This is because these wavenumbers are close to the detection limit of the instrument, which is 650 cm^{-1} , and thus, there are higher deviations in the measurement. Also, it was observed that temperature changes in the environment, as well as changes in the temperature of the detector (since it must be cooled with liquid nitrogen), greatly affect the base line of the spectra.

Nevertheless, two peaks are clearly observed. The first one, in 1200 cm^{-1} , corresponds to the bending vibration of D_2O . The second one is a broader peak located between 1050 and 865 cm^{-1} with a maximum intensity in 958 cm^{-1} that corresponds to the bending vibration of the Al-O-H bond [27]. The intensity of this peak was integrated and plotted to create a concentration profile and is presented in Fig. 6.29b.

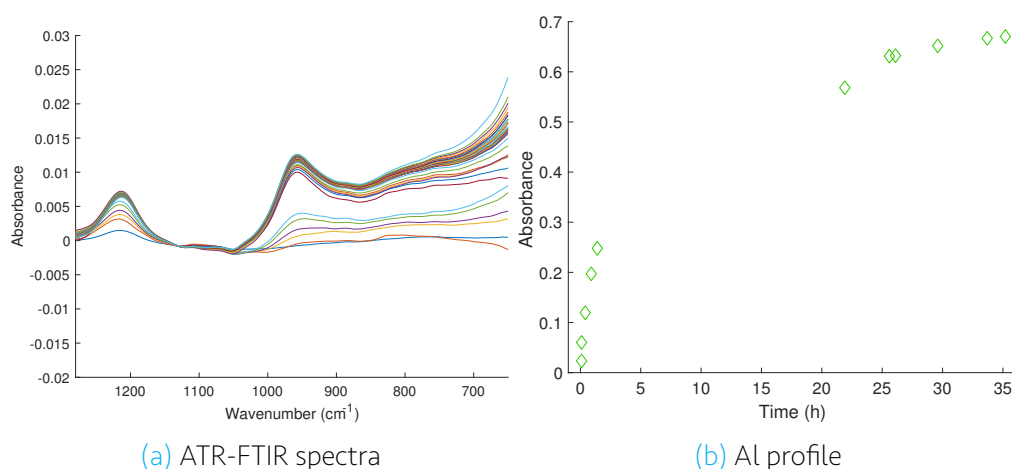


Fig. 6.29: ATR-FTIR spectra and concentration profile of aluminium in D_2O .

As can be seen in the Al profile, there is a fast increase in the intensity of this peak when it is brought in contact to D_2O . After a long period of time, it tends to stabilize and the intensity of the peak does not change any further. Therefore, this experiment showed that aluminium is not immediately stable when D_2O is added. Since the aluminium and arsenate peaks are located in the same region, it could cause an overlap of the peaks, interfering with the detection of arsenates. Therefore, an experiment to test whether the arsenates could be detected was done and is presented in the next section.

6.4.2 Aluminium in D_2O + Arsenates

This experiment was performed by changing the D_2O with a 0.01M solution of Na_2HAsO_4 in D_2O to test if arsenates could be detected. Spectra were collected every 30 minutes for a period of 24 hours. The results are shown in Fig. 6.30. The spectra show the same two peaks observed in the previous case: the D_2O peak located at 1200 cm^{-1} and the aluminium peak at 958 cm^{-1} . However, this last peak is different. A shoulder is starting to notice at lower wavenumbers (from 796 to 902 cm^{-1}) and is more evident as time passes. This peak corresponds to the stretching vibration of the As-O bond of

a Al-O-As complex [27]. The intensity of this part of the peak was integrated and its profile is presented in Fig. 6.30b. The intensity of the peak increases with time, which is due to the absorption reaction of arsenates in aluminium oxide.

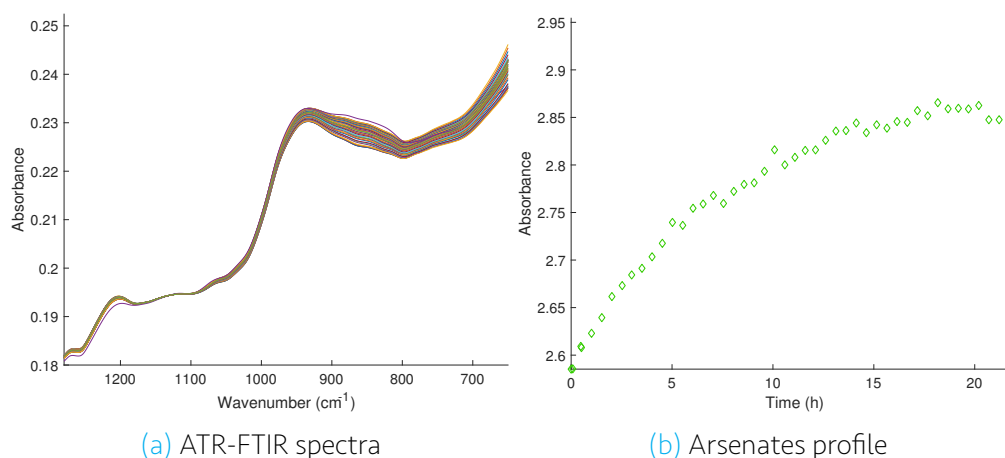


Fig. 6.30: ATR-FTIR spectra of aluminium in Na_2HAsO_4 and concentration profile of arsenates.

Two important conclusions are drawn from this experiment. The first one is that even though the peaks of aluminium and arsenates are in the same region, it is possible to distinguish from one another and individually calculate the intensity of the peak over time. The second conclusion is that the arsenates are absorbed within a reasonable time scale. Thus, in the diffusion experiments explained in the following section, they can be immediately detected as they reach the coating-aluminium interface.

6.4.3 Aluminium coated with dammar in D_2O + Arsenates

A third component is now added to the system: the varnish. Dammar was chosen since it was the coating that showed the highest stability to D_2O as it did not show any indication of swelling or detachment from the crystal, contrary to mastic and oil. To perform the experiment, an aluminium layer was deposited to the ATR-crystal and then coated with the dammar varnish. A background spectra of this sample was collected and the arsenates solution was added. Spectra was recorded every 30 minutes for a period of 24 hours.

In Fig. 6.31, selected spectra is presented. The first aspect to note is the variation of the baseline, which is much more pronounced in this sample than in the previous ones. This variation does not allow a clear comparison between the spectra and makes it impossible to distinguish individual peaks to perform a baseline correction. The change in the baseline may be associated to a numerous phenomenons. As mentioned in Section 6.4.1, the temperature of the environment and of the detector are important factors, as well as the proximity to the instrument detection limits. Additionally, as the solution diffuses through the coating, there are changes in the coating and in the aluminium

layer that are not only produced by D_2O but also by the arsenates that may affect the baseline.

The following changes in the spectra may be expected: As the D_2O diffuses through the coating, it is detected thus producing a positive peak. The coating may show negative peaks as less material is measured due to the interference with D_2O . The peak of aluminium increases as D_2O is reaching the interface, as seen in [Section 6.4.1](#) and the arsenate peak increases (seen as a shoulder in the Al peak) as the arsenates reach the aluminium oxide and form a complex, as seen in [Section 6.4.2](#).

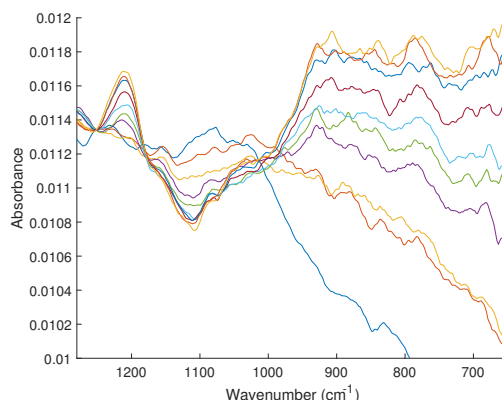


Fig. 6.31: ATR-FTIR spectra of dammar in Na_2HAsO_4 .

Unfortunately, all of these features cannot be identified in the spectra since the baseline is not at all constant and a baseline correction was not possible. One way to resolve the peaks is to do peak deconvolution, in which the spectra is fitted to a combination of gaussian functions and the individual identification of the peaks is possible. However, the intensity of the peaks is too low in this region of the spectrum and the variation of the baseline is too large, which may lead to large errors in the fitting. Thus, this approach was not explored.

Therefore, it was not possible to study the diffusion of arsenates in dammar with ATR-FTIR. This technique is too sensitive to the variations of the coating and the baseline. The region of interest is close to the detection limits of the instrument, which could also be a cause for such variation. Nevertheless, the diffusion of arsenites and arsenates was studied with electrochemical impedance spectroscopy and is presented in the following sections.

6.5 Arsenic diffusion studied by EIS

The diffusion of the arsenite and arsenate ions in the dammar and mastic varnishes was studied by EIS. As mentioned in [Section 3.3.1](#), the arsenites and arsenates have an affinity to oxides (particularly aluminium), where they are absorbed. The principle used in these experiments is that by using aluminium oxide coated with the varnishes as a substrate, the arsenic species will have a tendency to travel towards it. However, the species will

have to diffuse first through the coating in order to reach the oxide. It is such diffusion that is calculated with EIS. Therefore, the experiments were performed by immersing a coated aluminium plate with an oxide layer on top in arsenite or arsenate solutions. EIS data was taken over time, after which, the data was processed, fitted to an equivalent circuit and the diffusion coefficient was calculated by using a Warburg impedance element. Unfortunately, it was not possible to measure the diffusion in the glue and oil since these two coatings detached from the aluminium substrate immediately after immersion.

6.5.1 Arsenites in dammar

The diffusion of arsenites in dammar was analysed by EIS. The thickness of the coating was 18 μm and the electrolyte used was a 0.01M sodium (meta)arsenite NaAsO_2 solution. The resulting Nyquist and Bode plots at 2, 4, 6, 12 and 24 hours are presented in Fig. 6.32.

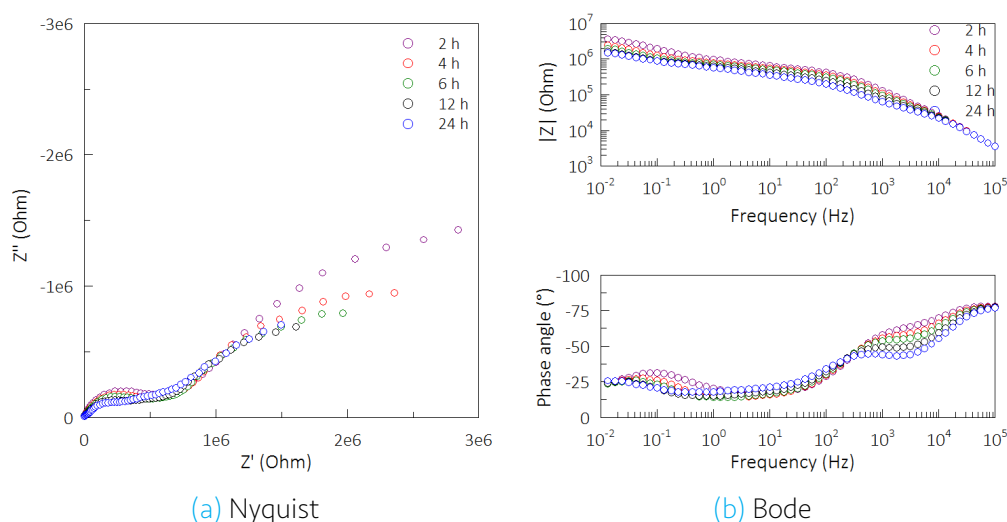


Fig. 6.32: EIS plots of dammar at 2, 4, 6, 12 and 24 h in a NaAsO_2 solution.

In the Nyquist plot (Fig. 6.32a) two semi-circles are observed at high frequencies, which belong to two time constants. The first one is observed between 10^3 and 10^4 Hz and the second one between 10 and 100 Hz. At low frequencies, below 1 Hz, there is a straight line that later bends towards the real axis at even lower frequencies. This low frequency feature is characteristic of mass diffusion in a finite layer. The straight line has a slope of approximately -1, which is distinctive of a Warburg element as discussed in Section 4.2.3. The semi-circle like shape at lower frequencies is typical of a finite length diffusion in a transmissive boundary, i.e. a short circuit Warburg.

In this case, in the Bode plot (Fig. 6.32b) showing the impedance magnitude, it is difficult to visualize and separate individual contributions. However, three resistances may be slightly differentiated by looking at the change in the slope of the curve. There is one located at a frequency of approximately 10^4 Hz, with an impedance magnitude of $10^4 \Omega$,

the second one between 100 and 10 Hz with an impedance magnitude of $10^5 \Omega$ and the third one between 1×10^{-1} and 10^{-2} Hz.

On the other hand in the phase angle plot, there are two high angle frequencies that correspond to the two semi-circles observed in the Nyquist plot and an increase in the angle at frequencies below 10^{-1} Hz that confirms the presence of the Warburg element.

The total impedance of the system, seen in the Bode plot, decreases with time from approximately 4×10^6 to $1 \times 10^6 \Omega$. This may be linked to the water uptake or to the degradation of the coating. However, as seen in the previous section, dammar proved to be stable maintaining its barrier properties in the presence of water, thus it is probable that the change in impedance is due to the water uptake. Nevertheless, in this experiment, the substrate is slightly changed since it has an oxide layer and the electrolyte is different, which could produce a different response of the coating.

The resistance that appears in the Bode plot at a frequency of approximately 10^4 Hz decreases with time. In the Nyquist plot this behaviour is confirmed in the decrease of the diameter of the first semi-circle, which is associated with this resistance. This reduction makes the semi-circle at 24 hours more easily observable. The behaviour of the second resistance (at approximately 10^2 Hz) with time is not clearly seen in neither plots.

In order to have quantitative information of the time constants observed in the spectra, and to be able to calculate the diffusion coefficient of the arsenite species in dammar, the data was fitted to an equivalent circuit. First, circuit C (Fig. 6.33a), which contains two time constants and a Warburg element, was used to fit the data as this elements were observed in the plots. A schematic representation of the circuit is presented in Fig. 6.33b. In this model, R_s represents the resistance of the solution, R_c is the resistance of the coating and CPE_c is the capacitance of the coating treated as a constant phase element to take into account heterogeneities of the coating. The second time constant is associated to the interface between the metal and the coating, where an oxide layer and the double layer are present. It is difficult to distinguish between the signals of these two layers since they are both very thin and their limit is not well defined. Therefore, the resistance and capacitance were named R_{int} and CPE_{int} to account for the two phenomenons taking place at the interface.

As explained in Section 3.3.1, there is a strong affinity of the arsenite species to the aluminium oxide. In order for the species to reach the oxide layer, they must diffuse through the coating. Such diffusion coefficient is represented in the equivalent circuit by the Warburg impedance Z_w .

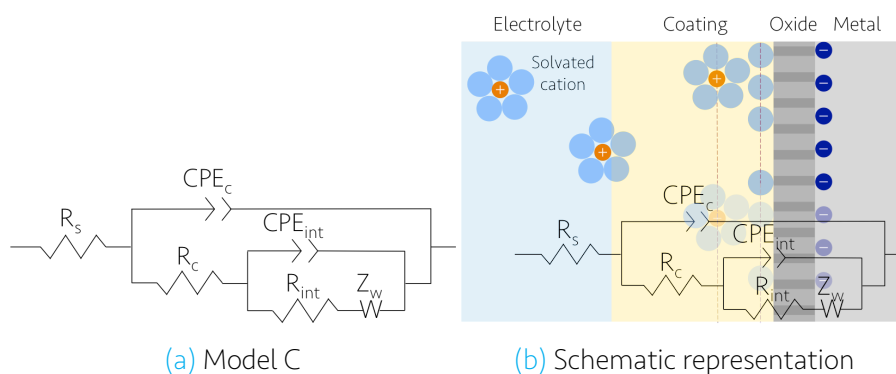


Fig. 6.33: Equivalent circuit C proposed to fit the EIS data of dammar in NaAsO_2 .

The EIS data at all times was fitted to model C. An example of the fitting is presented in Fig. 6.35, where the data taken at 4 hours was fitted with this circuit. Even though the χ^2 value is low (around 0.0007 for all data), the errors associated with the individual parameters is high, around 30%. For this reason, an equivalent circuit with an extra time constant was used. This circuit is shown in Fig. 6.34. In this model, apart from the resistance of the solution (R_s), the coating resistance and capacitance (R_c and CPE_c) and the Warburg impedance (Z_w), the resistance of the oxide R_o and the charge transfer resistance R_{ct} are included as separate parameters as well as the capacitance of the oxide CPE_o and the double layer capacitance CPE_{dl} . The separation of these two time constants allows a better fitting of the data at all times, as shown in Fig. 6.35. The χ^2 of this model (approximately 0.0002), although not significantly, is lower than the one obtained from fitting model C. Furthermore, model D produces lower individual errors and thus, was used to calculate the parameters at all times. The values obtained from the fitting are presented in Table 6.7.

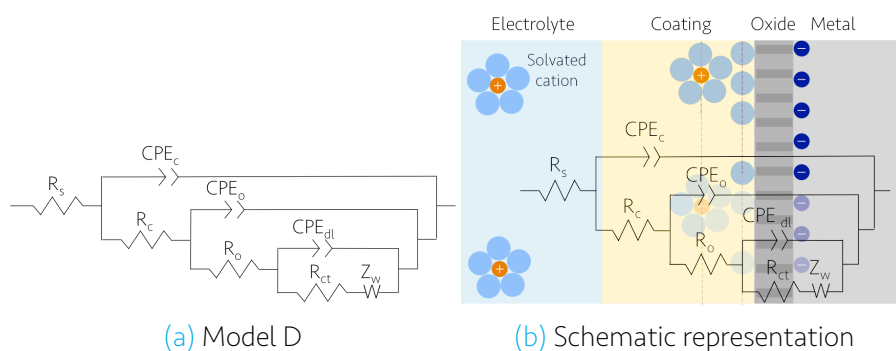


Fig. 6.34: Equivalent circuit D proposed to fit the EIS data of dammar in NaAsO_2 .

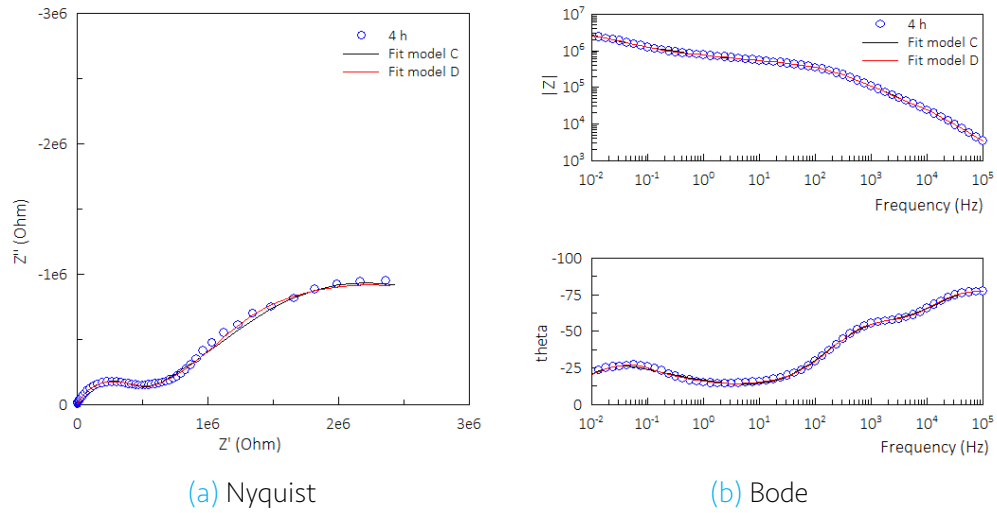


Fig. 6.35: EIS data of dammar in NaAsO_2 taken at 4 hours and fitted curve with models C and D.

Table 6.7: Fitted parameters of the EIS data of dammar in NaAsO_2 taken at 5.5 hours calculated with Model D.

Element	Units	Value	Error (%)
χ^2		0.00027	
R_s	(Ω)	141	35.01
R_c	(Ω)	4.09×10^3	6.53
CPE_c	(F)	1.36×10^{-9}	10.76
α_c		0.92	0.94
R_o	(Ω)	2.32×10^5	18.86
CPE_o	(F)	4.20×10^{-9}	28.61
α_o		0.86	3.53
R_{ct}	(Ω)	6.33×10^5	5.56
CPE_{dl}	(F)	6.10×10^{-7}	9.05
α_{dl}		0.37	8.85
W_r	(Ω)	2.94×10^6	8.13
W_t	(s)	17.63	6.71

The fitting of the parameters concerning the Warburg impedance is as follows. As mentioned in Chapter 5, the Warburg impedance that represents a finite length diffusion with a transmissive boundary is described by equation 6.11:

$$Z_w^s = \frac{\sigma}{\sqrt{j\omega}} \tanh \left[\sqrt{\frac{j\omega}{D}} l_e \right] \quad (6.11)$$

At low frequencies, this equation takes the form of equation 6.12. In this case, three fitting parameters are needed: the Warburg resistance W_r , the Warburg time constant

W_t and the parameter P . W_r and W_t are defined by equations 6.13 and 6.14, respectively. The parameter P is a coefficient that goes from 0 to 1 and in the case of a finite length diffusion $W_P=0.5$ and thus, it is fixed to 0.5 when fitting the data.

$$Z_w^s = W_r \cdot \frac{1}{(j\omega W_t)^P} \tanh[(j\omega W_t)^P] \quad (6.12)$$

$$\text{where } W_r = \frac{\sqrt{2}\sigma l_e}{\sqrt{D}} \quad (6.13)$$

$$\text{and } W_t = \frac{l_e^2}{D} \quad (6.14)$$

Therefore, there are two parameters from the Warburg impedance that are fitted to the data: W_r and W_t . These parameters are connected to the diffusion coefficient in the following way.

The Warburg impedance that results from changing the parameter P to 0.5 is:

$$Z_w^s = \frac{W_r}{\sqrt{W_t}} \cdot \frac{1}{\sqrt{j\omega}} \tanh(\sqrt{j\omega W_t}) \quad (6.15)$$

Substituting equation 6.14,

$$Z_w^s = \frac{W_r}{\sqrt{W_t}} \cdot \frac{1}{\sqrt{j\omega}} \tanh\left(\sqrt{\frac{j\omega}{D}} l_e\right)$$

Comparing with equation 6.11,

$$\sigma = \frac{W_r}{\sqrt{W_t}} \quad (6.16)$$

The parameter σ is the Warburg coefficient, which is also inversely proportional to the diffusion coefficient. Thus, the diffusion coefficient is obtained by calculating σ from the fitting parameters W_r and W_t and including it in the equation

$$D = \left[\frac{RT}{\sqrt{2}AF^2\sigma C} \right]^2 \quad (6.17)$$

where D is the diffusion coefficient of the diffusing specie ($\text{m}^2 \text{s}^{-1}$), R is the gas constant ($8.314 \text{ J K}^{-1} \text{ mol}^{-1}$), T is the absolute temperature (298 K), A is the area of the electrode surface ($2.48 \times 10^{-4} \text{ m}^2$), F is the Faraday constant ($96\,500 \text{ C mol}^{-1}$), σ is the Warburg coefficient ($\Omega \text{s}^{-1/2}$), and C is the concentration of the diffusing specie (10 mol m^{-3}).

The Warburg impedance parameters must be calculated from the spectra that shows a pure Warburg. During the first hours of the experiment, water is diffusing through the coating and thus, the system is constantly changing. The diffusion of the species must be calculated once an equilibrium is established and the response at low frequencies is only given by mass diffusion. Therefore, the Warburg parameters must be calculated from the spectra where the slope of the Nyquist plot is closer to -1. In this case, it was the one taken at 5.5 hours (Fig. 6.36a), with a slope of -0.92 with a R^2 of 0.99702.

The Warburg parameter σ was calculated with equation 6.16 by using the parameters W_t and W_r estimated with the fitting (Table 6.7). The obtained value of σ is $7.00 \times 10^5 \Omega \text{s}^{-1/2}$. The diffusion coefficient was calculated with equation 6.17 giving a value of $1.17 \times 10^{-16} \text{ cm}^2 \text{s}^{-1}$.

Additionally, the Warburg coefficient was calculated by a graphic method. In this procedure, the real and imaginary components of the Warburg impedance are plotted as a function of $\omega^{-1/2}$. The result of this plot is two perpendicular lines, as shown in Fig. 6.36b. Also in this case, the fitting must be done to the spectra that shows a pure Warburg behaviour, which in this case is the data taken at 5.5 hours. The lower frequency regions of both curves, which resemble a semi-infinite diffusion, are fitted to a line whose slope is equal to the Warburg coefficient σ . Theoretically, the slope of the two curves should be the same. However, experimentally there are associated errors and deviations of the data that lead to dispersion in the calculated slopes. Therefore, two Warburg coefficients were calculated: one for the real component and one for the imaginary one.

The slope of the line of the real component (σ_{real}) is $3.60 \times 10^5 \Omega \text{s}^{-1/2}$ with a R^2 of 0.99578; and of the imaginary part (σ_{im}) is $3.32 \times 10^5 \Omega \text{s}^{-1/2}$ with a R^2 of 0.99930. The diffusion coefficients calculated with these two Warburg coefficients with equation 6.17 are $D_{real} = 4.44 \times 10^{-16} \text{ cm}^2 \text{s}^{-1}$ and $D_{im} = 5.22 \times 10^{-16} \text{ cm}^2 \text{s}^{-1}$. A summary of this results is presented in Table 6.8.

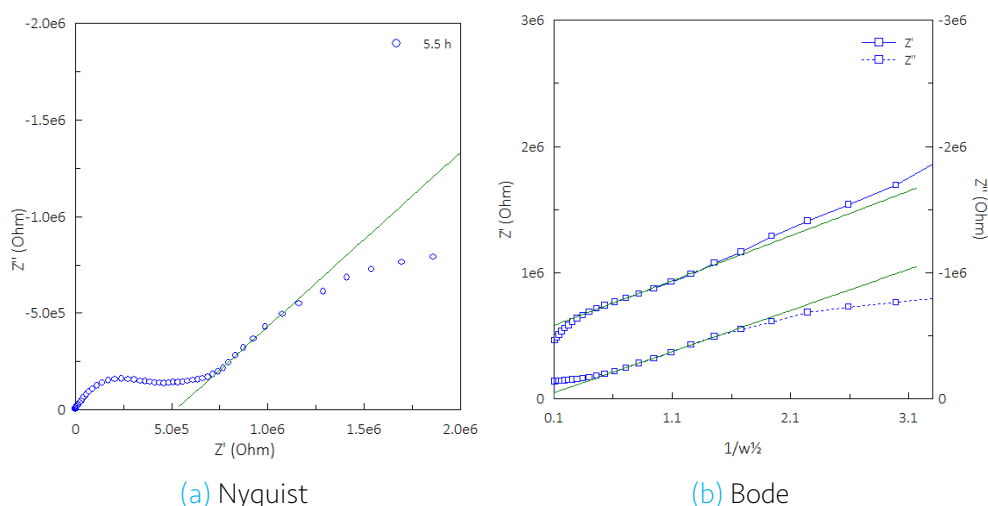


Fig. 6.36: Nyquist and Bode plot of dammar in NaAsO_2 at 5.5 hours.

As seen in Table 6.8, there is variation between the diffusion coefficient values calculated by the different methods. However they are similar to each other and lie within the range 1×10^{-16} and $5.3 \times 10^{-16} \text{ cm}^2 \text{ s}^{-1}$. The R^2 of the line fitting is good, higher than 0.99 and the associated error to the Warburg parameters is low: 2.72% for W_r and 6.62% for W_t . Therefore, the calculation of the diffusion coefficient by fitting the data to an equivalent circuit and by the graphic method proved to give similar results. As for the magnitude of the diffusion coefficient, it is several orders of magnitude lower than the diffusion coefficient of water in the same coating ($0.323 \times 10^{-9} \text{ cm}^2 \text{ s}^{-1}$ calculated previously with EIS). This indicates that the arsenite ions are not diffusing at the same pace as the water. There is a delay effect on the transport of arsenites caused by the coating due to the larger size of the molecule compared to water and the interaction it may have with the coating.

Table 6.8: Calculated Warburg coefficients and diffusion coefficients of arsenites in dammar.

Method	σ ($\Omega \text{ s}^{-1/2}$)	R^2	$D_{\text{As}^{3+}}$ ($\text{cm}^2 \text{ s}^{-1}$)
Fitting	7.00×10^5	-	1.17×10^{-16}
Slope Z'	3.60×10^5	0.99758	4.44×10^{-16}
Slope Z''	3.32×10^5	0.99930	5.22×10^{-16}

6.5.2 Arsenates in dammar

In the same manner, the diffusion of arsenates through dammar was studied. The thickness of the dammar coating was $30 \mu\text{m}$ and the electrolyte, a 0.01M sodium arsenate $\text{Na}_2\text{HAsO}_4 \cdot \text{H}_2\text{O}$ solution. The results at 2, 4, 6, 12 and 24 hours are presented in Fig. 6.37.

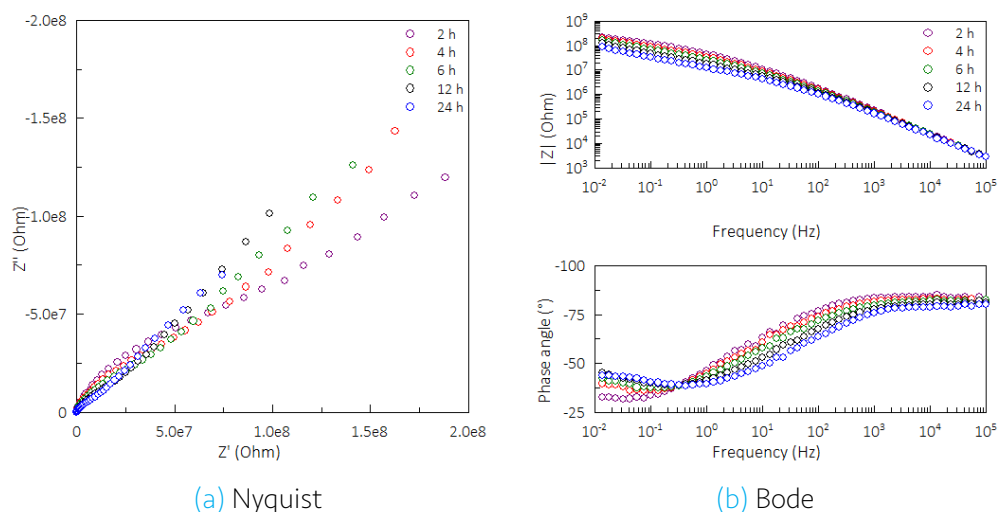


Fig. 6.37: EIS plots of dammar at 2, 4, 6, 12 and 24 h in a Na_2HAsO_4 solution.

In the Nyquist plot, a semi-circle above 100 Hz is observed; and at low frequencies, the characteristic line with a slope of -1 of the Warburg element. Contrary to the arsenite solution, in this sample the line does not bend toward the real axis. It continues as a straight line, which is distinctive of a diffusion in a semi-infinite layer (Section 4.2.3). This implies that the diffusion of arsenates may be taking place in a region so small that the thickness of the coating is regarded as infinite. This may be produced by two aspects. The first one is that the thickness of the coating may be much larger than the diffusion layer. In fact, the coating in this experiment is thicker than in the arsenite diffusion one, which could explain such difference. The other possible explanation is that the arsenate species diffuse much slower than the arsenite species, creating a smaller diffusion layer. Certainly a combination of the two explanations is another possibility: a slower diffusion in a thicker layer.

In the Bode plot, a plateau associated with a resistance is observed at frequency values of approximately 10^3 Hz. At lower frequencies, below 10^{-1} Hz, the phase angle approximates 45° , which is a characteristic of the Warburg impedance.

The EIS data was fitted with the equivalent circuit presented in Fig. 6.33 (Model C) as it was observed that this model described the data better than a circuit containing only one time constant. This circuit consists of the resistance of the solution R_s , the coating resistance R_c and capacitance CPE_c , the charge transfer resistance R_e , the double layer capacitance CPE_e and a semi-infinite Warburg element Z_w , that in the case of semi-infinite diffusion, is modelled as a CPE with a fixed α coefficient of 0.5, named CPE_w .

The data taken at 7 hours is presented in Fig. 6.38 as an example to show the fitting curve obtained with model C and the values are presented in Table 6.9. The χ^2 is low, in the order of 10^{-4} for all times, which indicates that the model is a good description of the data. The errors associated with the parameters are not ideal but still acceptable, reaching no more than 11%.

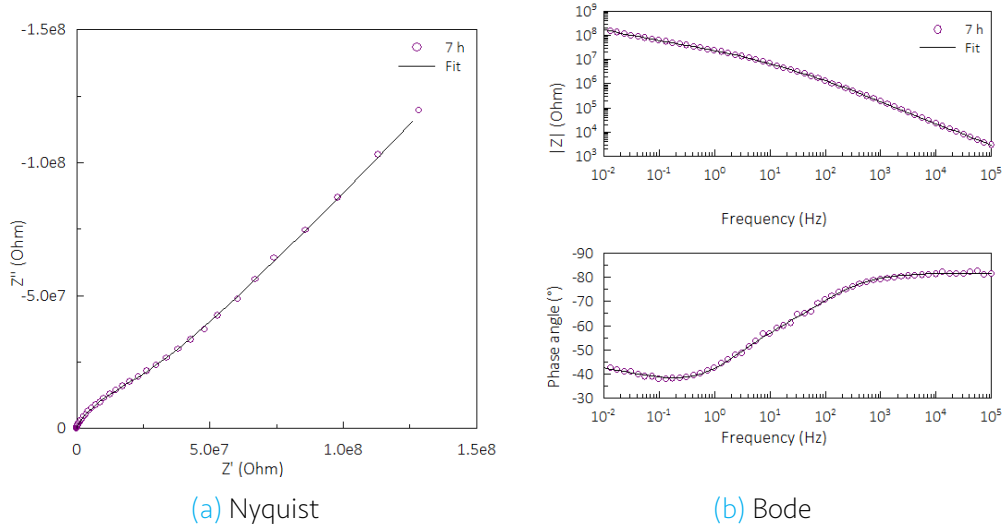


Fig. 6.38: EIS data of dammar in Na_2HAsO_4 taken at 7 hours and fitted curve with model C.

Table 6.9: Fitted parameters of the EIS data of dammar in Na_2HAsO_4 taken at 7 hours calculated with Model C.

Element	Units	Value	Error (%)
χ^2		0.00044	
R_s	(Ω)	23	10.75
R_c	(Ω)	3.86×10^6	9.11
CPE_c	(F)	1.89×10^{-9}	1.80
α_c		0.91	0.18
R_{ct}	(Ω)	3.34×10^7	10.07
CPE_{dl}	(F)	7.00×10^{-9}	9.93
α_{dl}		0.62	4.14
CPE_w	(F)	2.07×10^{-8}	4.05

The CPE that is used to fit the Warburg impedance is defined by:

$$CPE_w = \frac{\sqrt{W_t}}{W_r} \quad (6.18)$$

From equation 6.16, it is clear that

$$\sigma = \frac{1}{CPE_w} \quad (6.19)$$

Therefore, the Warburg coefficient σ was calculated from the fitting parameter CPE_w in order to calculate the diffusion coefficient. The data taken at 7 hours is the one that shows a pure Warburg impedance characterised by the slope of -1 in the Nyquist plot and therefore was used in such calculation. The fitted line is shown in Fig. 6.39a.

The slope of this curve is -1.01 with a R^2 of 0.99912. The CPE calculated from the fitting is 2.07×10^{-8} F and the σ calculated with equation 6.19 is $\sigma = 4.83 \times 10^7 \Omega s^{-1/2}$. The diffusion coefficient was then calculated with equation 6.17 giving a result of $2.46 \times 10^{-20} \text{ cm}^2 \text{ s}^{-1}$.

Furthermore, the Warburg coefficient was calculated by two different graphic methods. The first one is a method that applies to the semi-infinite diffusion and was discussed in Section 4.2.3. It consists in taking the intercept with the real axis of the fitted line x and calculating σ with the following equation:

$$\sigma_x = \left[\frac{R_s - R_{ct} - x}{2C_{dl}} \right]^2 \quad (6.20)$$

The second one is as discussed in the previous section when calculating the diffusion of arsenites: the slope of the lines in a Z' and Z'' vs $\omega^{1/2}$ is equal to σ . The Nyquist plot showing the intercept and the plot of Z' and Z'' vs $\omega^{1/2}$ are presented in Fig. 6.39a and Fig. 6.39b, respectively.

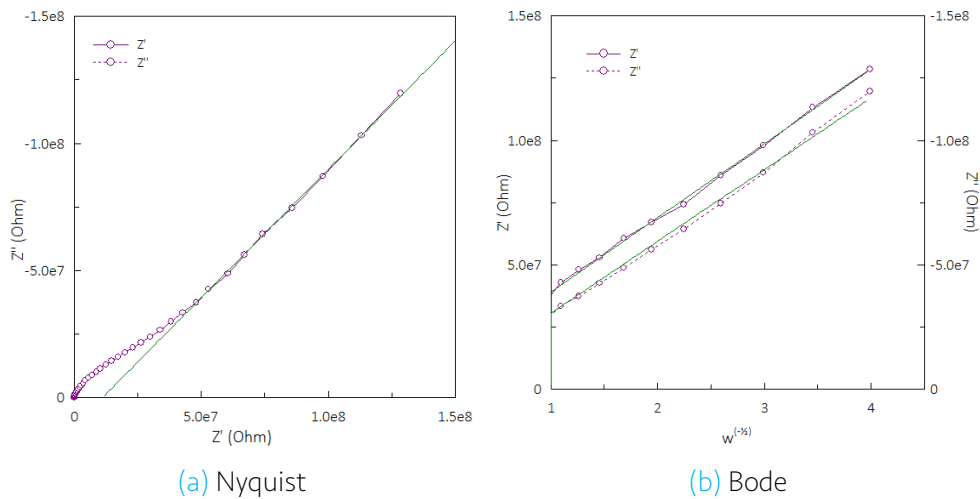


Fig. 6.39: Nyquist and Bode plot of dammar in Na_2HAsO_4 at 7 hours.

The results of the calculation of σ by the two graphic methods is presented in Table 6.10. The diffusion coefficient was calculated for each σ with equation 6.17 and are included in the table along with the σ and D calculated by fitting the equivalent circuit.

Table 6.10: Calculated Warburg coefficients and diffusion coefficients of arsenates in dammar.

Method	σ ($\Omega s^{-1/2}$)	R^2	$D_{As^{5+}}$ ($cm^2 s^{-1}$)
Fitting	4.83×10^7	-	2.46×10^{-20}
Intercept	3.99×10^7	0.99912	3.61×10^{-20}
Slope Z'	2.95×10^7	0.99909	6.61×10^{-20}
Slope Z''	2.95×10^7	0.99753	6.61×10^{-20}

As seen in the table above, the diffusion coefficient calculated by the several methods is similar. Moreover, in the graphic method, where σ was calculated as the slope of the real and imaginary components of the impedance, the values are exactly the same. It is once more concluded that the determination of the diffusion coefficient by the three different methods gives similar results, which was also seen for the arsenites in dammar in the previous section.

The magnitude of the diffusion coefficient of arsenates in dammar is much lower than that of arsenites (which was calculated in the previous section obtaining a result in the order of $10^{-16} cm^2 s^{-1}$). This is also seen in the difference between the Nyquist and Bode plots of the two cases. In the arsenite diffusion experiment, a finite-length diffusion with a transmissive boundary was observed, while with arsenates, the plots showed a semi-infinite diffusion. In the later case, the species diffuse in such a slow time that the coating looks like an infinite layer and thus, a semi-infinite Warburg appears. In conclusion, the diffusion coefficient of arsenites in dammar was found to be 4 orders of magnitude higher than that of arsenates. This similar behaviour occurs in the diffusion coefficients of this species in water (Section 3.3.2). Even though the coefficients have the same order of magnitude between each other, the one of arsenites is higher than that of arsenates.

6.5.3 Arsenites in mastic

Similarly, the experiment was performed for mastic. EIS measurements performed to an aluminium plate with an oxide layer on top coated with mastic. The thickness of the coating was $40 \mu m$ and the electrolyte, a 0.01M solution of $NaAsO_2$.

The Nyquist and Bode plots for selected measurements are presented in Fig. 6.40. In the Nyquist plot three semi-circles are observed at all times. The first semi-circle of the Nyquist plot (from left to right in the Z' axis) is not easily visible in the figure due to the scale of the plot. However, its intercept with the real axis (the resistance) decreases with time within the range of 10^4 and $10^5 \Omega$. The second semi-circle is more clearly appreciated and it is evident that its diameter decreases with time from 2×10^6 to $1 \times 10^6 \Omega$. The third semi-circle is incomplete and therefore, a fitting will show the behaviour in a clearer manner.

In the Bode plot, two plateaus, that are indicative of resistances, are visible. The first one is at 10^4 Hz and has a $|Z|$ of approximately $10^5 \Omega$. And the second one is observed at 1 Hz. The total impedance, shown in the Bode plot at a frequency of 10^{-2} Hz decreases with time and is between 1×10^6 and $1 \times 10^7 \Omega$.

The spectra thus consists of three time constants, corresponding to the three semi-circles of the Nyquist plot, each of them having the three resistances observed in the Bode plots.

The difference between this sample and those obtained for the arsenite and arsenate diffusion in dammar is the absence of the Warburg impedance. This indicates that the diffusion of arsenites in mastic in this sample cannot not be seen in the EIS data. To obtain more quantitative information, the EIS data was fitted to an equivalent circuit. The model used was a simplified version of Model D (Fig. 6.34), modified only by taking out the Warburg impedance.

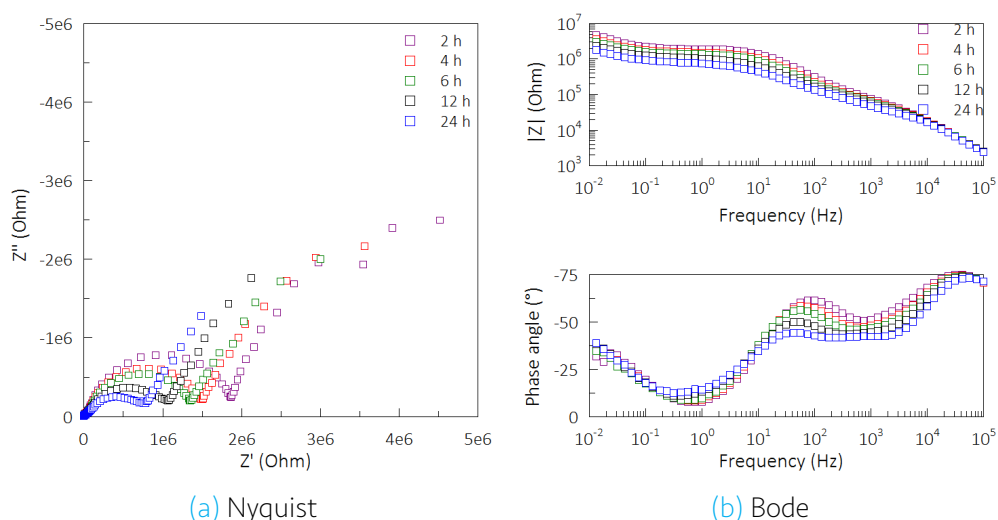


Fig. 6.40: EIS plots of mastic at 2, 4, 6, 12 and 24 h in a NaAsO₂ solution.

The simplified Model D equivalent circuit is therefore composed by the resistance of the solution R_s , the resistance and capacitance of the coating R_c and CPE_c , the double layer capacitance CPE_{dl} , the charge transfer resistance R_{ct} and the resistance and capacitance of the oxide R_o and CPE_o .

The fitting was performed to all the data. An example showing the measurement at 4 hours is presented in Fig. 6.41. The χ^2 value is in the order of 10^{-3} of all the data, which indicates that the simplified version of model D produces a good fit. The value of the parameters at 4 hours is presented in Table 6.11.

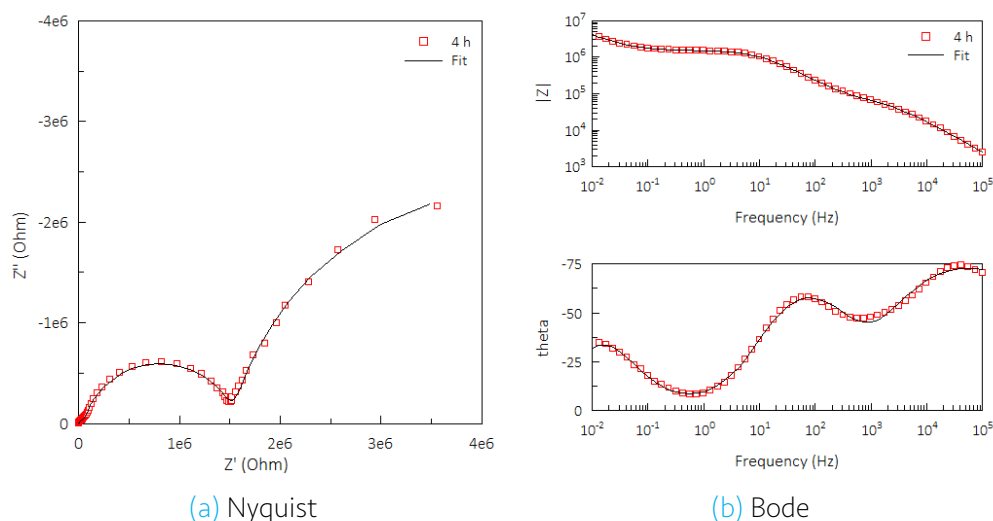


Fig. 6.41: EIS data of mastic in NaAsO₂ taken at 4 h and fitted curve with model D simplified.

Table 6.11: Fitted parameters of the EIS data of mastic in NaAsO₂ taken at 4 hours calculated with Model D.

Element	Units	Value	Error (%)
χ^2		0.0013	
R_s	(Ω)	168	33.08
R_c	(Ω)	8.81×10^4	3.35
CPE_c	(F)	3.98×10^{-9}	8.24
α_c	-	0.86	0.82
R_o	(Ω)	1.46×10^6	0.91
CPE_o	(F)	1.53×10^{-8}	4.74
α_o	-	0.85	0.84
R_{ct}	(Ω)	5.67×10^6	6.97
CPE_{dl}	(F)	2.87×10^{-6}	3.41
α_{dl}	-	0.87	2.00

A plot of the resistance and capacitance of the coating is presented in Fig. 6.42. Concerning the capacitance of the coating, first there is an increase in the capacitance which is linked to the water uptake, and at later hours there is a decrease, suggesting that the coating may be loosing its barrier properties. More interestingly, the magnitude of the resistance of the coating lies between 1.5×10^5 and $2 \times 10^4 \Omega^2 \text{ cm}^{-1}$. This values are considerably lower than those previously found for mastic in the water uptake measurements ($10^6 \Omega^2 \text{ cm}^{-1}$) and for those measured in the arsenates diffusion experiment also in mastic ($10^7 \Omega^2 \text{ cm}^{-1}$), which are presented in the next section. A possible explanation of the low resistance and the lack of a Warburg element in the spectra is that the coating may have had a defect. Although not seen when the sample was mounted, the fact that the value of the resistance of the coating is low since the first measurement may be the consequence of an already formed defect that allows the penetration of electrolyte since the beginning. As a result, the diffusion of arsenite species towards

the aluminium is not hindered and thus, a Warburg element is not seen in the spectra. Therefore, the diffusion coefficient of arsenites in mastic cannot be calculated in this case. It is important to note that this is only a hypothesis and that the presence of a defect in this sample cannot be proved. However, it is true that this varnish is quite brittle and during the assembly of the EIS cell, there is an O-ring that delimits the exposed area of the sample to the electrolyte that puts pressure on the coating and could lead to the formation of cracks.

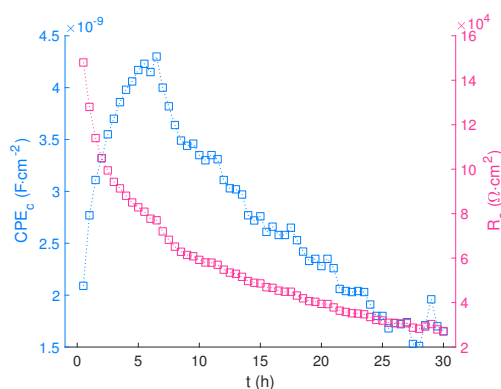


Fig. 6.42: Calculated CPE_c and R_c of mastic in NaAsO_2 .

6.5.4 Arsenates in mastic

The Nyquist and Bode plots of the EIS experiment results of mastic in a Na_2HAsO_4 solution are presented in Fig. 6.40. The thickness of the mastic coating was $30\text{ }\mu\text{m}$. The plots are similar to those obtained for the dammar in the arsenates solution in the sense that a semi-infinite Warburg impedance is observed at low frequencies (below $5 \times 10^{-2}\text{ Hz}$), characterized by the straight line with a slope close to -1 in the Nyquist plot. At higher frequencies, a semi-circle, whose diameter decreases over time, is seen.

In the Bode plot, it is observed that the total impedance of the system decreases with time from approximately 1×10^9 to $3 \times 10^8\text{ }\Omega$. This decrease may be linked either to the water uptake of the coating, to the lost in barrier properties of the coating or more likely, to both, as seen in the water uptake experiment.

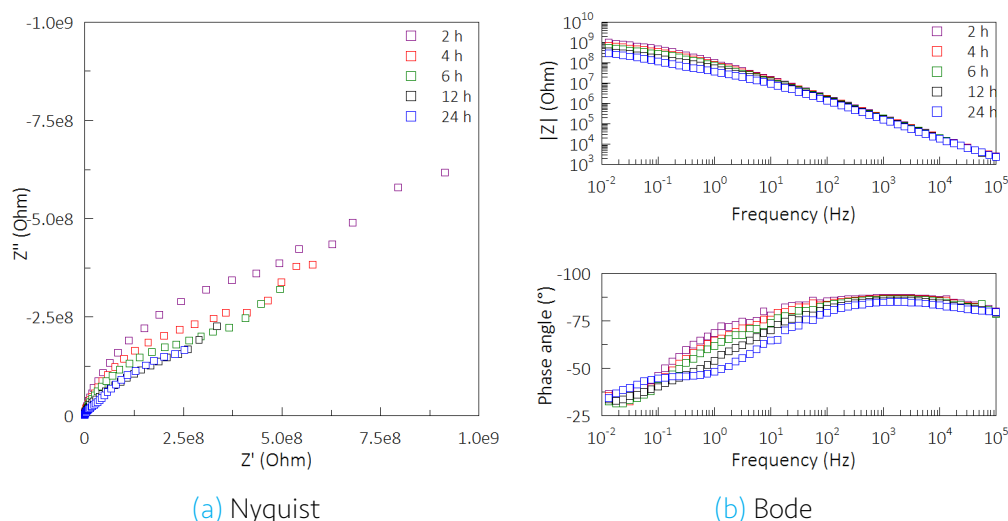


Fig. 6.43: EIS plots of mastic at 2, 4, 6, 12 and 24 h in a Na_2HAsO_4 solution.

The data at all times was fitted with model C (Fig. 6.33) obtaining a fit with a low χ^2 , below 2.5×10^{-3} for all the spectra. As in the diffusion of arsenates experiment in dammar, the Warburg impedance was modelled as a CPE with a coefficient of 0.5. An example of how the model fits the data is shown in Fig. 6.44 and the values for the fitted data taken at 4 hours are presented in Table 6.12.

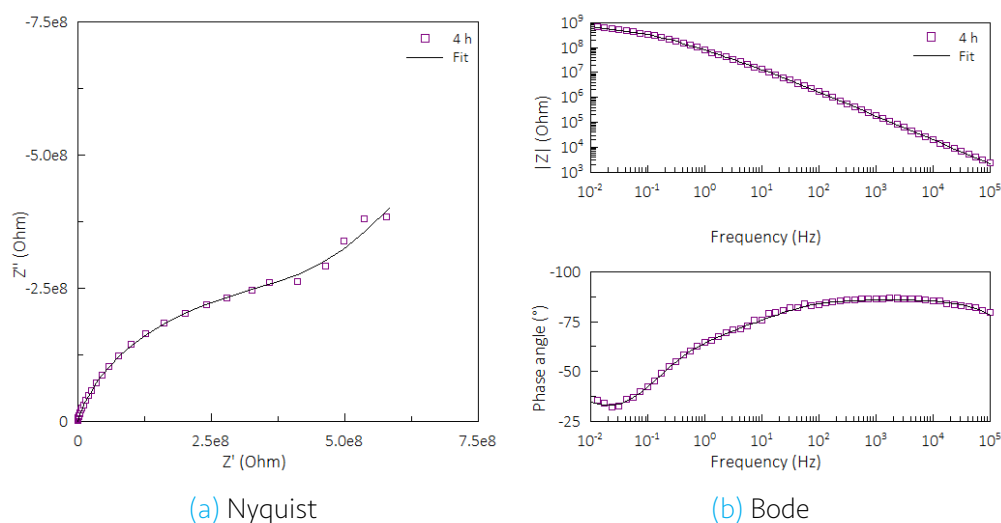


Fig. 6.44: EIS data of mastic in Na_2HAsO_4 taken at 4 hours and fitted curve with model C.

Table 6.12: Fitted parameters of the EIS data of mastic in Na_2HAsO_4 taken at 4 hours calculated with Model C.

Element	Units	Value	Error (%)
χ^2		0.0014	
R_s	(Ω)	307	8.06
R_c	(Ω)	4.06×10^7	8.47
CPE_c	(F)	1.31×10^{-9}	1.22
α_c		0.96	0.13
R_{ct}	(Ω)	3.98×10^8	6.17
CPE_{dl}	(F)	1.71×10^{-9}	4.16
α_{dl}		0.72	3.15
Z_w	(F)	8.12×10^{-9}	2.46

To calculate the diffusion coefficient, the spectra where the low frequency values show a pure controlled mass diffusion process must be used, which are seen in the Nyquist plot as a line with a slope of -1. In this case, the spectra taken at 4 hours had the slope with a value closest to 1 and thus, was used to calculate the diffusion coefficient. Fig. 6.45a shows the fitted line. The slope is -0.82 and the R^2 of 0.88518. This is not a perfect fit as seen in the R^2 value, which may be caused by the interference of other processes taking place in the system. Nevertheless, the diffusion coefficient was estimated from this spectra. The Warburg coefficient σ was calculated from the fitted parameters of the data taken at 4 hours by using equation 6.19 and are shown in Table 6.12. This yields a value of $\sigma = 1.23 \times 10^8 \Omega \text{s}^{-1/2}$. The diffusion coefficient was calculated with equation 6.17 obtaining a value of $3.79 \times 10^{-21} \text{cm}^2 \text{s}^{-1}$.

The diffusion coefficient was additionally calculated by the graphic method explained in Section 6.5.1. Briefly, the Warburg coefficient is equal to the slope of the lines in a Z' and Z'' vs $\omega^{-1/2}$ plot, as shown in Fig. 6.45b. The results are presented in Table 6.13.

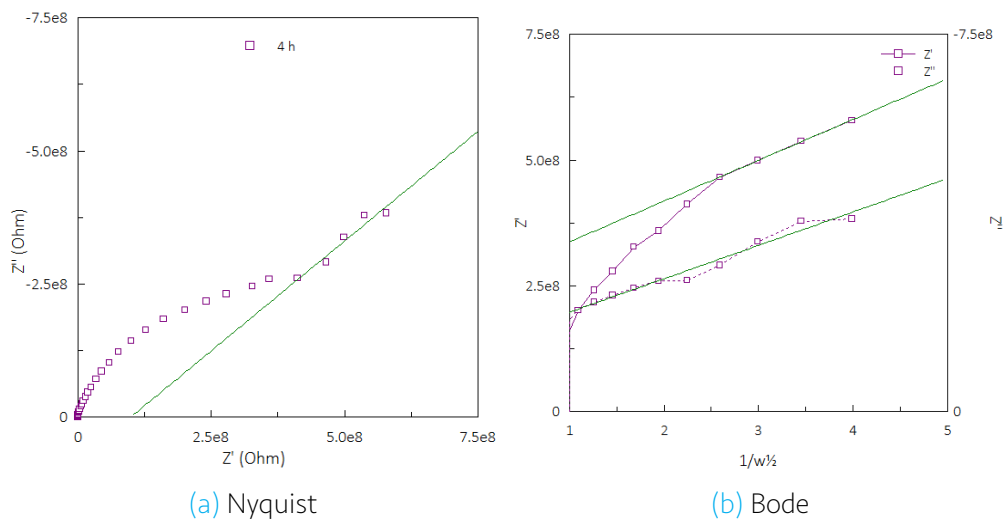


Fig. 6.45: EIS plots of mastic at 4 hours in a Na_2HAsO_4 solution.

Table 6.13: Calculated Warburg coefficients and diffusion coefficients of arsenates in dammar.

Method	σ ($\Omega s^{-1/2}$)	R^2	$D_{As^{5+}}$ ($cm^2 s^{-1}$)
Fitting	1.23×10^8	-	3.79×10^{-21}
Slope Z'	8.89×10^7	0.89797	7.28×10^{-21}
Slope Z''	8.13×10^7	0.83801	8.70×10^{-21}

Unfortunately, the values of the diffusion coefficient of arsenites and arsenates in mastic cannot be compared. However, the diffusion of arsenates in mastic can be compared to the diffusion in dammar. The values found for the diffusion coefficient of arsenates in dammar are between 2.46×10^{-20} and $6.61 \times 10^{-20} cm^2 s^{-1}$. As seen in Table 6.13, the diffusion coefficients in mastic are in the order of $10^{-21} cm^2 s^{-1}$, which means that the diffusion of arsenates in mastic is slower than in dammar.

6.6 Discussion

Water diffusion

A comparison between the water diffusion coefficients in the three coatings obtained by ATR-FTIR spectroscopy and EIS is presented in Table 6.14. Two values calculated with ATR-FTIR spectroscopy, that corresponds to the calculation made from the two water peaks (1200 and 2500 cm^{-1}), are shown. The letters (SC) are indicative that a swelling coefficient was used in the calculation. While it was possible to calculate the diffusion coefficient of water in dammar and oil by the two above mentioned techniques, the diffusion coefficient in mastic could only be calculated with ATR-FTIR spectroscopy and only from the peak located at 2500 cm^{-1} since other peaks of the coating were overlapping the 1200 cm^{-1} peak.

Table 6.14: Calculated water diffusion coefficients for dammar, mastic and oil.

Method	D ($10^{-9}\text{ cm}^2\text{ s}^{-1}$)		
	Dammar	Mastic	Oil
ATR-FTIR (2500 cm^{-1})	0.11	0.23 (SC)	2.72 (SC)
ATR-FTIR (1200 cm^{-1})	0.15	-	2.13 (SC)
EIS	0.32	-	1.12

The diffusion coefficient values of dammar and mastic are comparable. The molecules that constitute these two varnishes are similar and therefore, it is not surprising that the diffusion coefficients are not too far apart. However, there are important differences in the behaviour of these materials. In the ATR-FTIR experiments, a two-step diffusion profile was observed in mastic and three possible explanations were given: swelling of the coating, detachment from the ATR-crystal or a heterogeneous water uptake. However with this technique it is not possible to distinguish the real cause of this phenomena. Nevertheless, it was observed that the introduction of a swelling coefficient (SC) to the fitting equation produced a better fit for the mastic and oil coatings, which suggests that one of the before mentioned phenomenons, or the combination of them, are taking place.

The EIS experiments showed an abnormal behaviour in the capacitance of mastic over time. The expected behaviour, which was seen in dammar, is an increase of the capacitance due to the penetration of water. The capacitance of the coating depends on the permittivity of the medium. Since the permittivity of water is higher than that of the dried coating, there is an increase in the capacitance as water diffuses through. However in mastic, there is an increase of the capacitance of mastic caused by an initial water uptake, followed by a decrease in the capacitance, which was attributed to a decrease in the barrier properties of the coating; in other words, the polymer was losing the ability to restrict the passage of water. This may be produced by a rearrangement in the

coating molecules as water diffuses through, creating paths for an easier diffusion of subsequent water molecules.

Genty-Vincent et al studied the blanching of paint and varnishes in easel paintings. *Blanching* is a term that refers to a change in the appearance of paints and varnishes in which they turn white and opaque. They analysed the blanching phenomena by immersing mock-up samples of mastic and dammar in water. They found that the blanching of mastic was more visible than that of dammar and that it was produced by the scattering of light inside the pores. They observed that the size of the pores in mastic increased with time up to a point that the interconnection of the pores was produced. This made the percentage of solid matter too low to ensure the cohesion of the material. In this thesis, the observed decrease in capacitance and resistance of mastic might be caused by the same principle studied by Genty-Vincent et al. Upon immersion, the porosity of mastic increases facilitating the penetration of water, or as called previously, decreasing its barrier properties. Moreover, their observations coincide with those found in this thesis in the sense that mastic showed more blanching than dammar; and in this thesis, a decrease in the barrier properties was only found in the case of mastic.

Therefore, it is concluded that dammar is a more stable varnish than mastic. The superior properties of dammar are also seen in the works of art. Mastic was a varnished used since antiquity until dammar was introduced, which substituted mastic due to its higher quality [19].

It was observed that the diffusion coefficient of water in oil is one order of magnitude higher than that of mastic and dammar. That means that the water diffusion in oil is faster than in the varnishes. Additionally, the presence of a signal characteristic of carboxylic acids was found in the oil's ATR-FTIR spectra at long immersion times, which is an indication of an oxidation reaction of the ester groups present in the oil molecules. The oil also showed a two-step diffusion profile in the ATR-FTIR spectroscopy experiments. The EIS data did not show any signs of swelling or heterogeneous diffusion. Therefore, the most probable cause for the water intensity increase after saturation seen in the ATR-FTIR spectroscopy experiments is a (partial) detachment of the oil film, which was observed after the experiment finished.

Arsenites and arsenates diffusion

The diffusion coefficients of arsenites and arsenates in dammar and mastic calculated with EIS are presented in [Table 6.15](#). First of all, the diffusion coefficients estimated from the different methods are similar between each other, which indicates that no matter what method is used, they yield similar values. It was not possible to compare the coefficients to other reported values since, to our knowledge, only the diffusion coefficients of arsenites and arsenates in water, and not in other media, are reported. The same holds for similar species, such as phosphates. Nevertheless, the magnitudes of the diffusion coefficients in water are not comparable since the diffusion through a solid material is completely different. However, it is possible to compare the trends and the general behaviour of the species.

Table 6.15: Calculated arsenite and arsenate diffusion coefficients for dammar and mastic in $\text{cm}^2 \text{s}^{-1}$.

Method	Dammar		Mastic
	Arsenite	Arsenate	Arsenate
Fitting	1.17×10^{-16}	2.46×10^{-20}	3.70×10^{-21}
Slope Z'	4.44×10^{-16}	6.61×10^{-20}	7.28×10^{-21}
Slope Z''	5.22×10^{-16}	6.61×10^{-20}	8.70×10^{-21}

The diffusion coefficient of arsenites in dammar is higher than that of arsenates, which is also the case for the diffusion of this species in water [28, 29]. This has to do with the larger size of arsenates caused by a larger hydration layer. The diffusion of arsenates in dammar is faster than in mastic, as suggested by the diffusion coefficients separated by one order of magnitude. This difference may be caused by the different polarity and structure of the two varnishes. While no literature was found about the differences in arrangement of the dammar and mastic structures or their porosity, its composition has been well studied. It has been found that mastic is slightly more polar than dammar [19]. The polar groups inside the coatings have interactions with the diffusing molecules, which reduce the diffusion rate. The more polar groups inside the coating, the more interactions and thus, a slower diffusion. Since mastic is more polar than dammar, the diffusion of arsenates in this varnish is expected to be slower (not taking into account the effect of the porosity), just as is seen in the calculated diffusion coefficients.

Although the magnitude of the diffusion coefficients cannot be proved or compared to a reference, the tendency in the diffusion coefficient values is in accordance with what is known about both the properties of arsenites and arsenates and the properties of the varnishes.

Methodology

EIS and ATR-FTIR spectroscopy proved to be two complementary techniques for this research in the sense that not only they provide different types of information about a system but also because they allow to calculate the same parameter by measuring different properties of the materials. For example, the diffusion coefficient. In one hand, in ATR-FTIR spectroscopy the vibration between the atoms of water molecules are detected once they have crossed the entire thickness of the coating. The change in concentration in the crystal-coating interface is estimated and thus, a diffusion coefficient is calculated. On the other hand, the calculation in EIS is based in how the capacitance of the coating as a whole changes as water enters the coating. The change in capacitance is linked to the water uptake of the coating and therefore, the diffusion coefficient is calculated. The possibility to calculate the coefficient by two different techniques based on different principles, makes the result more reliable.

However, it is not always the case that a technique can provide results for all types of systems since they come with experimental limitations. For example, the water diffusion

coefficient of mastic could not be measured with EIS due to the decrease in its capacitance but it was possible to study it with ATR-FTIR spectroscopy since the measured response of this technique is different. On the other hand, the diffusion of arsenite and arsenate could be studied with EIS since this technique allows to distinguish between the different processes and study them separately, while the interference of the signals in the ATR-FTIR spectra made it impossible. Therefore, the proposed methodology allows the analysis of this type of systems. Sometimes one technique is more suitable to study one system than the other. But undoubtedly, a combination of both techniques allows to have a more complete picture of the system and thus, a better understanding.

ATR-FTIR spectroscopy

Naturally, each of the techniques has inherent limitations and complications. As observed in the ATR-FTIR spectroscopy experiments, the baseline of the spectra is highly sensitive to a number of factors such as the environmental temperature, the detector's temperature and the alignment of the sample inside the cell.

Since the temperature of the lab is not controlled and the period of the experiments was 40 hours, there were changes in the temperature of the environment that affected the measurements. The volumes used in the cell of the ATR-FTIR spectrometer are approximately 3 ml, which during experiments in hot days, completely evaporated. The temperature of the detector is another important factor. It is manually filled with liquid nitrogen to keep the temperature low during the measurements. During these long experiments it is necessary to refill the chamber a couple of times. It was observed that the measurements done before and after refilling the chamber, vary significantly, as can be seen in the water diffusion in mastic experiment. The alignment of the cell is another factor to take care of. The sample must be disassembled after taking the background to coat the ATR-crystal and reassembled to take the measurements. If the alignment of the crystal in the cell is different than that when the background spectra was taken, the baseline of the new measured spectra will be different. In the case of the oil, the change was such that a new background of the already coated sample had to be taken to perform the measurements, which is not ideal since the oil peaks cannot be normalized against the original peaks.

Moreover, the baseline must be corrected in order to have a common baseline for all the spectra and be able to integrate the peaks to create a concentration profile. The software used to control the spectrometer has an option to automatically correct the baseline. However, it does so differently for every spectra. Therefore, it was decided to perform a correction with Matlab to all of the spectra in the same manner. This way, a more accurate quantification of the integrated intensities is done and the different spectra is comparable to each other.

In the arsenic diffusion experiments, the arsenates peak is located in a region of low wavenumbers, which is affected since it is close to the detection limit of the instrument. Also, the interpretation of the spectra becomes complicated when simultaneous processes are taking place at the interface of the crystal and the signals of all the processes

change with time and overlap. In this case, the processes taking place were the penetration of water to the coating, the reaction of the water with the aluminium layer, the diffusion of arsenates through the coating and the coating being detected as a negative intensity against the background. Hence, the diffusion of arsenic species through the coating was not possible.

EIS

EIS is a technique that allows to study simultaneous processes at different depths of the sample from the electrolyte to the metal, involving the coating, double layer, oxide layer or any other intermediate layers. Each of the processes are modelled as an electrical element connected together to form an equivalent circuit. As a consequence, care must be taken when choosing the equivalent circuit that describes the data. A circuit can be built with any number of electrical elements. The more electrical elements, the better the fit of the experimental data; but this does not mean that the equivalent circuit is describing the physical system. Each of the elements must be linked to a process taking place in the sample, which are not always clear and easily identifiable but must always be correctly described by the electrical elements in the circuit. Furthermore, in the ZView software the EIS data is fitted to a chosen equivalent circuit. The initial values given to the fitting parameters (which are the electrical elements) must be carefully chosen to produce a good fit. Sometimes it is recommendable to perform a simulation with the initial values and change those that deviate from the data to be able to produce a fit.

The diffusion of ions, from an experimental point of view, is a complicated and not commonly studied subject. Hence, the literature is scarce, specially the one concerning the Warburg impedance. Also, the fitting of the Warburg impedance is poorly described in the software documentation. The fitting of the Warburg must be chosen according to one of the three Warburg impedance cases: semi-infinite diffusion, finite-length diffusion in a transmissive boundary or finite-length diffusion in a conductive boundary; as the diffusion coefficient calculation highly depends on which case is selected. The selection is made according to the shape of the low frequency region of the EIS data and to the expected behaviour based on previous knowledge.

Chapter 7

Conclusions and recommendations

7.1 Conclusions

In this thesis, the migration of the degradation products of the pigments orpiment and realgar was studied. The thesis comprised two parts with different approaches. First, ex-situ measurements were done in a painting reconstruction trying to imitate the real conditions of a painting. The analysis was performed with imaging techniques and the materials used were the intact pigment and different grounds applied to a canvas. The second approach was based on in-situ measurements to try to understand the migration of already degraded pigments through painting materials. The possibility to study the diffusion of water, arsenites and arsenates in varnishes and oil with EIS and ATR-FTIR spectroscopy was explored.

The cross-sections of painting reconstructions that consist of different grounds (chalk, earth pigment and lead white) and a layer of orpiment on top were analysed by SEM and FTIR microscopy. It was observed that thinner samples contained oxidation products dispersed throughout the orpiment layer, whereas thicker samples presented an oxidation front in the upper part of the sample. This is caused because the inner part of the sample in a thick layer has less access to light, water and oxygen than the upper part and as a consequence, the oxidation process is limited.

By the two imaging methods, it was found that arsenic is confined to the orpiment layer in all the samples. A small amount of arsenic was found in the ground close to the interface between the orpiment and ground. However, it is not a large enough quantity to conclude that migration of arsenic from the orpiment layer into the ground took place. It is therefore recommended to prolong the light ageing process to try to accelerate the migration of arsenic, since within this time it was not observed.

In the in-situ experiments, the diffusion coefficient of water in dammar, mastic and oil was determined by ATR-FTIR spectroscopy. The diffusion coefficients of dammar and oil were confirmed by EIS. The water diffusion in the varnishes proved to be faster than in the oil. Furthermore, the water in mastic and oil showed a non-Fickian diffusion,

which consist in a two-step profile, where first there is a fast increase in the water uptake followed by a slower diffusion. In mastic, this is believed to be caused by a decrease in the barrier properties, which allows more water to penetrate. In oil, it was associated to the (partial) detachment of the film from the crystal, which was confirmed with visual examination.

The diffusion of arsenates and arsenites in dammar, as well as the arsenates in mastic, was quantified with EIS. The values calculated should be regarded as a first estimation of the diffusion coefficients since no reported values were found in the literature. Nonetheless, the relation between the diffusion coefficients of arsenites and arsenates in dammar is the same as the diffusion of these ions in water. The calculated diffusion coefficient of arsenites in dammar is higher than that of arsenates, which indicates a higher mobility of arsenites in the varnish. This is partly caused by the lower size of the hydration layer of arsenites compared to arsenates.

In conclusion, a first approach to the diffusion of arsenic in painting systems was made. The two techniques proved to provide valuable information and complemented each other for a better understanding of the system. As seen in this thesis, the main research question is far more complicated than originally thought and would therefore require further research to be answered. In the next section, recommendations for future work are presented.

7.2 Recommendations

- Since no migration was observed in the painting reconstruction cross sections, it is advised to artificially age the samples further. In some of the cross-sections that had a thick orpiment layer, most of the oxidation products were found in the upper part of the sample, away from the ground. By increasing the time of artificial ageing, the oxidation of the orpiment is ensured in all the layer so the migration of arsenite or arsenate will be enhanced. Moreover, it is recommended to produce layers with the same thickness for all the samples to be able to compare the migration times and the effect of the grounds in the diffusion.
- The analysis of the cross-sections with a technique with a higher resolution, such as synchrotron based techniques like XANES, could more accurately identify the small amounts of arsenic that might have migrated into the layer and differentiate the oxidation states of the compounds. This will allow a better understanding of the oxidation and migration mechanism in the painting reconstructions.
- Due to time constraints, the reproducibility of the experiments was not tested. Therefore, it is recommended to repeat the water diffusion and arsenic diffusion experiments by the two techniques.
- A method to calculate the diffusion coefficient of arsenites and arsenates with the Warburg element was proposed. As already mentioned, the values should be regarded as a first approach since there are no values reported in the literature to

compare with. However, it resulted to be a promising method since it is in accordance with the observed trends of arsenite and arsenate diffusion in water. For its application to other systems, the method should be verified. This may be done by determining the diffusion coefficients calculated with the Warburg element by other techniques such as Raman spectroscopy and compare them.

- One parameter that influences the diffusion of both water and arsenic species is the state of the coating. In this thesis, the varnishes and oil used were fresh. However, these materials also degrade with time. They undergo a process called auto-oxidation in which they react with oxygen from the environment to produce free radicals. These free radicals can react with each other to form smaller molecules, or can react with other triterpenoid molecules (in the varnishes) or other fatty acids (in oil) to form cross-links. Besides changing the structure of the varnish, the number of molecules with oxygen containing functional groups increases, which may lead to a higher water uptake [20, 17].
- A recommendation of future work is to study the effect that adding pigments to the oil has on the arsenic species diffusion. As reported in the painting case studies presented in the introduction, arsenic was found forming compounds with lead particles from the lead white paint layer [1, 2]. Therefore, the transport of arsenic may be influenced by the presence of these particles. The first step would be to study how the diffusion of water changes when adding pigments to the oil and afterwards, analyse the diffusion of arsenite and arsenate through this layer. As seen in this thesis, the diffusion of water may be studied with ATR-FTIR spectroscopy and EIS while the diffusion of arsenic with EIS.

Appendix A

ATR-FTIR spectroscopy D₂O diffusion.

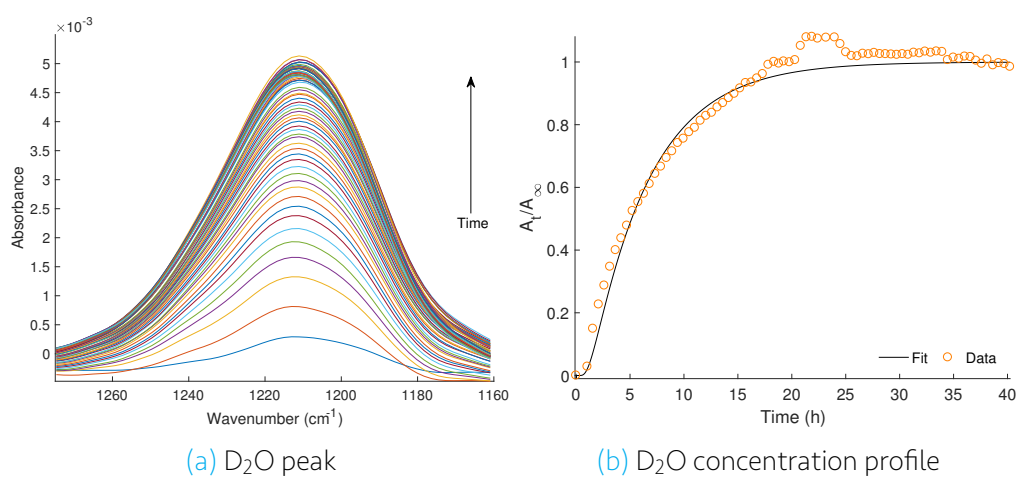


Fig. A.1: (a) ATR-FTIR time resolved spectra of Dammar showing the D₂O peak in the 1200 cm⁻¹ and (b) normalized integrated absorbance of the D₂O peak as a function of time.

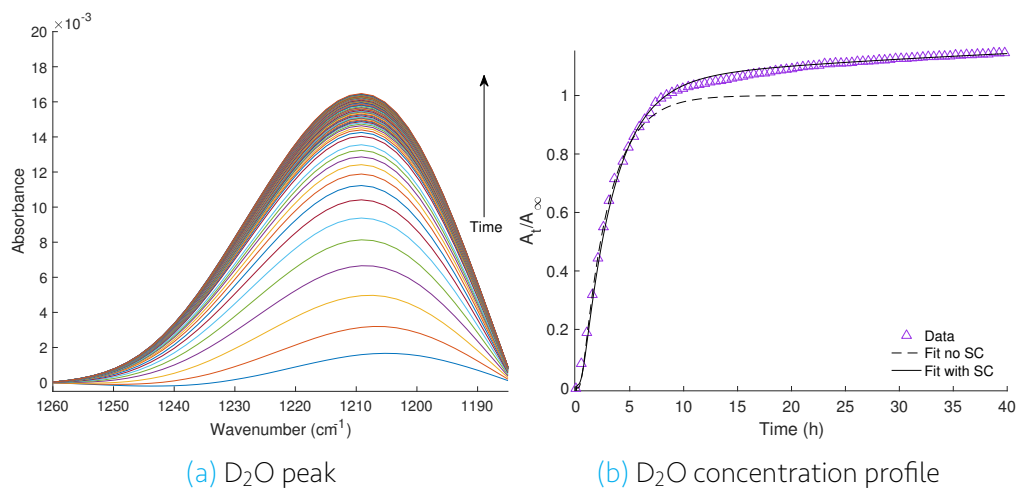


Fig. A.2: (a) ATR-FTIR time resolved spectra of Oil showing the D_2O peak in the 1200 cm^{-1} and (b) normalized integrated absorbance of the D_2O peak as a function of time and fitted curves of Fickian diffusion (dotted) and considering a SC (solid).

Appendix B

EIS water diffusion

Table B.1: EIS data of water diffusion in Dammar.

Time (h)	χ^2	R_s (Ω)	R_s error (%)	R_c ($\cdot 10^6 \Omega$)	R_c error (%)	R_{ct} ($\cdot 10^6 \Omega$)	R_{ct} error (%)	CPE_{dl} (nF)	CPE_{dl} error (%)	α_{dl}	α_{dl} error (%)	CPE_c error (nF)	α_c	α_c error (%)	
0.0	0.0042	1949	42	16.00	31.99	39.30	14.10	4.29	16.71	0.84	8.86	11.00	3.00	0.91	0.38
0.5	0.0023	1976	35	3.93	21.59	29.30	5.28	20.60	4.76	0.62	4.64	14.30	3.23	0.90	0.40
1.0	0.0021	1926	33	2.44	38.89	32.30	4.23	18.90	4.36	0.56	3.60	14.40	4.22	0.90	0.50
1.5	0.0019	1909	33	2.47	42.14	38.60	3.94	16.90	3.89	0.56	3.37	14.20	4.23	0.90	0.49
2.0	0.0022	1917	34	2.70	40.45	41.60	3.93	15.80	3.90	0.58	3.45	13.90	4.26	0.90	0.50
2.5	0.0018	1924	31	3.00	29.50	38.80	3.40	15.90	3.52	0.60	3.06	13.90	3.50	0.90	0.42
3.0	0.0020	1953	32	2.81	30.07	35.80	3.37	15.20	3.63	0.61	3.04	14.00	3.69	0.90	0.44
3.5	0.0021	1968	34	2.59	30.62	31.10	3.47	14.80	3.93	0.62	3.10	14.30	3.94	0.90	0.47
4.0	0.0023	1980	35	2.46	22.60	24.90	3.05	15.10	4.16	0.67	2.89	14.80	3.78	0.89	0.46
4.5	0.0022	1981	34	2.37	18.25	20.70	2.81	15.80	4.19	0.70	2.71	15.40	3.51	0.89	0.43
5.0	0.0024	1992	35	2.28	17.32	17.90	2.91	16.40	4.52	0.72	2.82	15.90	3.61	0.89	0.45
6.0	0.0027	1992	38	1.83	17.51	14.00	3.00	18.60	4.88	0.72	2.91	16.70	4.05	0.88	0.50
7.0	0.0025	1986	37	1.63	16.28	11.80	2.90	19.60	4.89	0.72	2.80	17.20	4.01	0.88	0.49
8.0	0.0030	1990	41	1.56	18.41	11.20	3.32	19.60	5.59	0.72	3.16	17.30	4.52	0.88	0.55
9.0	0.0025	1988	38	1.24	15.41	11.60	2.27	19.80	4.97	0.73	2.37	16.70	4.37	0.88	0.53
10.0	0.0030	1980	42	1.12	17.22	11.70	2.32	19.60	5.68	0.74	2.47	17.10	4.98	0.88	0.60
11.0	0.0024	1964	38	1.13	15.83	12.70	2.07	20.00	4.99	0.73	2.21	17.20	4.52	0.88	0.54
12.0	0.0023	1933	38	0.98	20.71	13.70	2.14	19.10	5.66	0.70	2.22	18.60	5.13	0.87	0.61
13.0	0.0021	1906	38	1.07	24.69	14.80	2.44	18.70	5.71	0.68	2.39	19.80	5.18	0.86	0.62
14.0	0.0021	1898	37	1.09	23.64	15.30	2.35	18.80	5.53	0.68	2.33	19.60	5.04	0.87	0.60
15.0	0.0022	1910	37	1.21	18.53	15.50	2.17	20.20	4.76	0.70	2.25	18.30	4.53	0.87	0.55
16.0	0.0021	1886	36	1.10	19.68	15.70	2.07	19.40	5.03	0.70	2.14	18.60	4.69	0.87	0.56
17.0	0.0019	1845	35	1.25	21.79	15.60	2.39	18.40	5.16	0.69	2.36	19.90	4.51	0.86	0.54
18.0	0.0018	1814	33	1.25	19.01	15.60	2.13	17.60	5.38	0.71	2.20	20.40	4.23	0.86	0.51
19.0	0.0021	1832	35	1.11	16.98	15.50	1.89	19.50	5.03	0.72	2.04	19.00	4.42	0.87	0.53
20.0	0.0019	1810	35	0.90	19.09	15.20	1.76	18.30	5.95	0.72	1.92	19.70	4.90	0.87	0.58
21.0	0.0018	1792	34	0.88	18.66	14.80	1.70	17.50	6.29	0.73	1.88	20.20	4.83	0.86	0.58
22.0	0.0020	1789	35	0.86	19.30	14.70	1.76	18.20	6.23	0.72	1.92	19.90	5.04	0.87	0.60
23.0	0.0020	1774	35	0.83	18.63	14.40	1.71	18.90	6.17	0.72	1.89	20.40	5.03	0.86	0.60
24.0	0.0018	1774	33	0.91	15.14	14.60	1.57	19.90	5.20	0.73	1.75	20.00	4.37	0.87	0.53
40.0	0.0016	1601	31	0.53	19.39	32.50	1.28	19.70	6.55	0.71	1.17	21.40	5.63	0.87	0.65

Table B.2: EIS data of water diffusion in Mastic.

Time (h)	χ^2	R_s (Ω)	R_s error (%)	R_c ($\cdot 10^6 \Omega$)	R_c error (%)	R_{ct} ($\cdot 10^6 \Omega$)	R_{ct} error (%)	CPE_{dl} (nF)	CPE_{dl} error (%)	α_{dl}	α_{dl} error (%)	CPE_c (nF)	CPE_c error (nF)	α_c (%)	α_c error (%)
1	0.00015	286	2.20	1.65	2.56	19.10	3.23	50.20	1.54	0.45	1.10	1.90	0.96	0.78	0.08
2	0.00048	262	4.25	1.69	4.09	15.50	4.88	42.50	2.26	0.49	1.48	1.98	0.96	1.38	0.13
3	0.00070	258	5.28	1.63	5.20	13.10	9.23	37.90	2.25	0.52	1.67	1.99	0.96	1.74	0.17
4	0.00041	261	4.01	1.78	2.97	14.30	5.87	36.80	1.90	0.55	1.13	2.02	0.96	1.23	0.12
5	0.00035	265	3.75	1.54	3.72	13.80	5.24	35.60	1.78	0.52	1.13	1.96	0.96	1.30	0.13
6	0.00020	268	2.83	1.54	2.35	21.10	4.33	37.20	1.22	0.53	0.73	1.97	0.96	0.95	0.09
7	0.00021	265	2.91	1.52	2.52	23.20	4.83	37.00	1.18	0.52	0.72	1.95	0.96	0.98	0.10
8	0.00026	269	3.22	1.48	3.52	23.30	5.17	36.00	1.40	0.50	0.91	1.94	0.96	1.16	0.11
9	0.00010	265	2.00	1.41	2.42	34.40	3.31	35.70	0.85	0.48	0.56	1.91	0.96	0.73	0.07
10	0.00014	276	2.30	1.32	2.85	37.80	3.97	35.40	1.02	0.49	0.64	1.89	0.96	0.89	0.08
11	0.00018	266	2.74	1.36	3.15	38.60	4.91	35.40	1.09	0.49	0.70	1.92	0.96	1.00	0.10
12	0.00018	276	2.64	1.26	3.52	28.20	4.50	35.20	1.15	0.49	0.74	1.88	0.96	1.05	0.10
13	0.00016	272	2.46	1.36	2.82	36.70	4.56	35.70	1.02	0.49	0.64	1.91	0.96	0.92	0.09
14	0.00029	267	3.45	1.07	4.43	28.00	4.32	32.30	1.66	0.51	0.91	1.84	0.96	1.42	0.13
15	0.00012	277	2.14	1.06	4.40	29.60	3.15	31.90	1.00	0.47	0.66	1.85	0.96	0.99	0.09
16	0.00010	272	2.03	0.94	4.51	37.30	2.94	30.30	0.94	0.47	0.59	1.83	0.96	0.97	0.09
17	0.00033	283	3.72	0.67	11.72	41.20	5.94	31.70	1.80	0.45	1.10	1.76	0.96	2.21	0.20
18	0.00016	272	2.65	0.73	6.77	37.50	3.72	31.80	1.12	0.46	0.69	1.80	0.96	1.42	0.13
19	0.00019	269	3.00	0.73	8.53	16.30	4.56	35.20	1.08	0.46	0.93	1.84	0.96	1.64	0.15
20	0.00026	273	3.62	0.50	18.04	31.70	3.94	31.90	1.35	0.44	0.94	1.77	0.96	2.55	0.22
21	0.00023	274	3.40	0.49	20.24	30.80	3.61	32.10	1.31	0.43	0.97	1.80	0.96	2.52	0.22
22	0.00019	262	3.08	0.64	11.14	28.20	3.18	31.90	1.22	0.45	0.83	1.84	0.96	1.81	0.16
23	0.00022	261	3.27	0.61	8.61	29.40	3.48	32.10	1.39	0.47	0.80	1.82	0.96	1.82	0.16

Table B.3: EIS data of water diffusion in Oil.

Time (h)	Chi-Sqr	Rs(±) ohm	Rs(Error%) (%)	Rc 10 kohm	Rc(Error%) (%)	CPE c-T(+) nanofarad	CPE c-T(Error%) (%)	alpha	alpha error (%)
0.0	0.0024	496	5.26	3.90	0.61	1.85	1.37	0.95	0.15
0.9	0.0014	450	4.57	4.05	0.48	1.91	1.07	0.94	0.12
1.7	0.0015	440	4.80	4.31	0.50	1.92	1.08	0.94	0.12
2.6	0.0015	427	4.99	4.38	0.51	1.94	1.08	0.94	0.12
3.4	0.0017	417	5.41	4.35	0.54	1.96	1.15	0.94	0.13
4.1	0.0013	401	5.03	4.63	0.49	2.00	1.01	0.94	0.11
4.7	0.0012	394	4.84	4.69	0.46	2.02	0.95	0.94	0.11
5.4	0.0012	389	5.04	4.63	0.47	2.02	0.98	0.94	0.11
6.1	0.0011	387	4.77	4.64	0.44	2.02	0.93	0.94	0.10
6.8	0.0010	381	4.72	4.66	0.43	2.04	0.90	0.94	0.10
7.4	0.0012	373	5.10	4.67	0.46	2.07	0.95	0.94	0.11
8.1	0.0013	374	5.49	4.65	0.49	2.07	1.02	0.94	0.11
8.8	0.0014	367	5.81	4.62	0.51	2.09	1.06	0.93	0.12
9.4	0.0014	370	5.67	4.59	0.50	2.08	1.05	0.93	0.12
10.1	0.0013	364	5.69	4.58	0.50	2.10	1.03	0.93	0.12
10.8	0.0016	362	6.22	4.53	0.54	2.11	1.12	0.93	0.13
11.5	0.0014	364	5.80	4.50	0.50	2.10	1.05	0.93	0.12
12.2	0.0013	368	5.47	4.48	0.48	2.08	1.01	0.93	0.11
13.1	0.0014	362	5.90	4.45	0.51	2.11	1.07	0.93	0.12
14.0	0.0013	360	5.59	4.39	0.48	2.12	1.01	0.93	0.11
14.9	0.0014	355	5.99	4.37	0.50	2.13	1.06	0.93	0.12
15.7	0.0013	355	5.84	4.31	0.49	2.14	1.04	0.93	0.12
16.7	0.0013	354	5.80	4.29	0.49	2.14	1.03	0.93	0.12
17.5	0.0013	351	5.92	4.20	0.49	2.14	1.05	0.93	0.12
18.3	0.0012	352	5.57	4.10	0.46	2.13	1.00	0.93	0.11
19.1	0.0015	347	6.34	3.98	0.51	2.14	1.12	0.93	0.13
19.9	0.0013	349	5.80	3.93	0.47	2.13	1.04	0.93	0.12
20.7	0.0014	348	6.05	3.86	0.49	2.13	1.08	0.93	0.12
21.4	0.0014	342	6.13	3.78	0.49	2.15	1.08	0.93	0.12
22.0	0.0012	340	5.65	3.72	0.44	2.15	1.00	0.93	0.11
22.6	0.0013	341	6.02	3.64	0.47	2.15	1.07	0.93	0.12
23.1	0.0012	332	5.95	3.62	0.46	2.17	1.03	0.93	0.11
23.6	0.0013	338	5.88	3.58	0.46	2.15	1.04	0.93	0.12
24.1	0.0012	334	5.80	3.56	0.45	2.16	1.01	0.93	0.11
24.7	0.0012	332	5.85	3.52	0.45	2.16	1.02	0.93	0.11
25.2	0.0011	333	5.67	3.51	0.43	2.16	0.99	0.93	0.11
25.7	0.0012	332	5.90	3.47	0.45	2.17	1.03	0.93	0.11
91.1	0.0015	278	7.73	2.45	0.48	2.38	1.22	0.92	0.13
91.6	0.0015	267	8.00	2.42	0.47	2.38	1.21	0.92	0.13

Bibliography

- [1] K. Keune, J. Mass, A. Mehta, J. Church, and F. Meirer. "Analytical imaging studies of the migration of degraded orpiment, realgar, and emerald green pigments in historic paintings and related conservation issues". In: *Heritage Science* 4 (2016), pp. 1–14. ISSN: 2050-7445. DOI: [10.1186/s40494-016-0078-1](https://doi.org/10.1186/s40494-016-0078-1).
- [2] K. Keune, J. Mass, F. Meirer, C. Pottasch, A. v. Loon, A. Hull, J. Church, E. Pouyet, M. Cotte, and A. Mehta. "Tracking the transformation and transport of arsenic sulfide pigments in paints: synchrotron-based X-ray micro-analyses". In: *Journal of Analytical Atomic Spectrometry* 30.3 (2015), pp. 813–827. ISSN: 1364-5544. DOI: [10.1039/C4JA00424H](https://doi.org/10.1039/C4JA00424H).
- [3] W. S. Taft and J. W. Mayer. *The science of paintings*. Springer, 2000. ISBN: 038798722-3.
- [4] B. Murchison. *Points West Online: Is it a fake? An Art Museum Caper*. URL: <https://centerofthewest.org/2015/02/28/points-west-online-fake-art-museum-caper/>.
- [5] *Electromagnetic spectrum*. URL: <http://www.chromacademy.com/lms/sco736/images/Electromagnetic-spectrum.jpg>.
- [6] *What is Wave Absorption? - Definition and Examples*. URL: <http://study.com/academy/lesson/what-is-wave-absorption-definition-examples.html>.
- [7] *Materials database - CAMEO - Museum of fine arts Boston*. URL: http://cameo.mfa.org/wiki/Category:Materials_database.
- [8] C. T.S. R. Eastaugh N Walsh V. "The Pigment Compendium". In: (2004), p. 512. DOI: [10.4324/9780080943596](https://doi.org/10.4324/9780080943596).
- [9] D. Goltz, J. McClelland, A. Schellenberg, M. Attas, E. Cloutis, and C. Collins. "Spectroscopic Studies on the Darkening of Lead White". In: *Applied Spectroscopy* 57.11 (2003), pp. 1393–1398. ISSN: 00037028. DOI: [10.1366/000370203322554563](https://doi.org/10.1366/000370203322554563).
- [10] *Vermeer's Palette: White Lead*. URL: http://www.essentialvermeer.com/palette/palette_white_lead.html#.WetAWWKCwy4.
- [11] E. West Fitzhugh. "Orpiment and realgar". In: *Artists' pigments: a handbook of their history and characteristics, Volume 3*. Washington, DC: National Gallery of Art, 1997, pp. 47–79. ISBN: 9780894682568.

- [12] S. Fendorf, P. S. Nico, B. D. Kocar, Y. Masue, and K. J. Tufano. *Arsenic Chemistry in Soils and Sediments*. Vol. 34. Elsevier Masson SAS, 2010, pp. 357–378. ISBN: 0166-2481. DOI: [10.1016/S0166-2481\(10\)34012-8](https://doi.org/10.1016/S0166-2481(10)34012-8).
- [13] *Orpiment* - ColourLex. URL: <http://colourlex.com/project/orpiment/>.
- [14] *Realgar* - ColourLex. URL: <http://colourlex.com/project/realgar/>.
- [15] V. Horie. *Materials for Conservation*. 2nd ed. Elsevier Ltd, 2010. ISBN: 1098-6596905-4.
- [16] J. Mills and R. White. *The Organic Chemistry of Museum Objects*. 2nd ed. Routledge, 2012. ISBN: 1136000011, 9781136000010.
- [17] M. Lazzari and O. Chiantore. "Drying and oxidative degradation of linseed oil". In: *Polymer Degradation and Stability* 65.2 (1999), pp. 303–313. ISSN: 01413910. DOI: [10.1016/S0141-3910\(99\)00020-8](https://doi.org/10.1016/S0141-3910(99)00020-8).
- [18] *Fatty acids 2*. URL: https://commons.wikimedia.org/wiki/Fatty_acids_2.
- [19] J. H. Stoner and R. Rushfield, eds. *Conservation of easel paintings*. Routledge, 2013. ISBN: 1136000410, 9781136000416.
- [20] G. A. van der Doelen. *Molecular studies of fresh and aged triterpenoid varnishes*. 1999, pp. 1–190. ISBN: 9080170437. DOI: [10.2307/1506734](https://doi.org/10.2307/1506734).
- [21] P. A. O'Day. "Chemistry and mineralogy of arsenic". In: *Elements* 2.2 (2006), pp. 77–83. ISSN: 18115209. DOI: [10.2113/gselements.2.2.77](https://doi.org/10.2113/gselements.2.2.77).
- [22] K. Trentelman, L. Stodulski, and M. Pavlosky. "Characterization of Pararealgar and Other Light-Induced Transformation Products from Realgar by Raman Microspectroscopy". In: *Analytical Chemistry* 68.10 (1996), pp. 1755–1761. ISSN: 0003-2700. DOI: [10.1021/ac951097o](https://doi.org/10.1021/ac951097o).
- [23] A. Kyono. "Experimental study of the effect of light intensity on arsenic sulfide (As₄S₄) alteration". In: *Journal of Photochemistry and Photobiology A: Chemistry* 189.1 (2007), pp. 15–22. ISSN: 10106030. DOI: [10.1016/j.jphotochem.2006.12.043](https://doi.org/10.1016/j.jphotochem.2006.12.043).
- [24] M. F. Lengke and R. N. Tempel. "Reaction rates of natural orpiment oxidation at 25 to 40°C and pH 6.8 to 8.2 and comparison with amorphous As₂S₃ oxidation". In: *Geochimica et Cosmochimica Acta* 66.18 (2002), pp. 3281–3291. ISSN: 00167037. DOI: [10.1016/S0016-7037\(02\)00925-0](https://doi.org/10.1016/S0016-7037(02)00925-0).
- [25] M. Sadiq, T. H. Zaidi, and A. A. Mian. "Environmental behaviour of arsenic in soils: Theoretical". In: *Water, Air and Soil Pollution* 20.1981 (1983), pp. 369–377.
- [26] P. Lu and C. Zhu. "Arsenic Eh-pH diagrams at 25°C and 1 bar". In: *Environmental Earth Sciences* 62.8 (2011), pp. 1673–1683. ISSN: 18666280. DOI: [10.1007/s12665-010-0652-x](https://doi.org/10.1007/s12665-010-0652-x).
- [27] S. Goldberg and C. T. Johnston. "Mechanisms of Arsenic Adsorption on Amorphous Oxides Evaluated Using Macroscopic Measurements, Vibrational Spectroscopy, and Surface Complexation Modeling". In: *Journal of Colloid and Interface Science* 234.1 (2001), pp. 204–216. ISSN: 00219797. DOI: [10.1006/jcis.2000.7295](https://doi.org/10.1006/jcis.2000.7295).

- [28] M. Tanaka, Y. Takahashi, N. Yamaguchi, K. W. Kim, G. Zheng, and M. Sakamitsu. "The difference of diffusion coefficients in water for arsenic compounds at various pH and its dominant factors implied by molecular simulations". In: *Geochimica et Cosmochimica Acta* 105 (2013), pp. 360–371. ISSN: 00167037. DOI: [10.1016/j.gca.2012.12.004](https://doi.org/10.1016/j.gca.2012.12.004).
- [29] Y. Takahashi, M. Sakamitsu, and M. Tanaka. "Diffusion Coefficients of Arsenate and Arsenite in Water at Various pH". In: *Chemistry Letters* 40.10 (2011), pp. 1187–1188. ISSN: 0366-7022. DOI: [10.1246/cl.2011.1187](https://doi.org/10.1246/cl.2011.1187).
- [30] *IR: carboxylic acids*. URL: <http://orgchemboulder.com/Spectroscopy/irtutor/carbacidsir.shtml>.
- [31] B. H. Stuart. *Infrared Spectroscopy: Fundamentals and Applications*. Analytical Techniques in the Sciences. Chichester, UK: John Wiley & Sons, Ltd, 2004. ISBN: 9780470011140. DOI: [10.1002/0470011149](https://doi.org/10.1002/0470011149).
- [32] J. C. d. Silva, A. Queiroz, A. Oliveira, and V. Kartnaller. "Advances in the Application of Spectroscopic Techniques in the Biofuel Area over the Last Few Decades". In: *Frontiers in Bioenergy and Biofuels*. InTech, 2017. DOI: [10.5772/65552](https://doi.org/10.5772/65552).
- [33] *University of Glasgow - ISAAC : Imaging Spectroscopy and Analysis Centre - Services - Scanning Electron Microscopy*. URL: <https://www.gla.ac.uk/schools/ges/researchandimpact/researchfacilities/isaac/services/scanningelectronmicroscopy/>.
- [34] G. Artioli. *Scientific Methods and Cultural Heritage*. Oxford University Press, July 2010. ISBN: 9780199548262. DOI: [10.1093/acprof:oso/9780199548262.001.0001](https://doi.org/10.1093/acprof:oso/9780199548262.001.0001).
- [35] G. Fieldson and T. Barbari. "The use of FTi.r.-a.t.r. spectroscopy to characterize penetrant diffusion in polymers". In: *Polymer* 34.6 (Jan. 1993), pp. 1146–1153. ISSN: 00323861. DOI: [10.1016/0032-3861\(93\)90765-3](https://doi.org/10.1016/0032-3861(93)90765-3).
- [36] D. Loveday, P. Peterson, and B. Rodgers. "Evaluation of Organic Coatings with Electrochemical Impedance Spectroscopy Part 1 : Fundamentals of Electrochemical Impedance Spectroscopy". In: *JCT coatings tech* August (2004), pp. 46–52.
- [37] E. Barsoukov and J. R. Macdonald. *Impedance Spectroscopy Theory, Experiment, and Applications*. Second Edi. John Wiley & Sons, 2005. ISBN: 0-471-64749-7.
- [38] A. J. Bard and L. R. Faulkner. *Electrochemical Methods: Fundamentals and Applications*. Vol. 2. New York, Wiley, 1980. ISBN: 9780471043720. DOI: [10.1016/B978-0-08-098353-0.00003-8](https://doi.org/10.1016/B978-0-08-098353-0.00003-8).
- [39] A. Lasia. *Electrochemical Impedance Spectroscopy and its Applications*. New York, NY: Springer New York, 2014. ISBN: 978-1-4614-8932-0. DOI: [10.1007/978-1-4614-8933-7](https://doi.org/10.1007/978-1-4614-8933-7).
- [40] *Phase Difference and Phase Shift in an AC Circuit. Electronic Tutorials*. URL: <http://www.electronics-tutorials.ws/accircuits/phase-difference.html>.

- [41] G. Bouvet, D. D. Nguyen, S. Mallarino, and S. Touzain. "Analysis of the non-ideal capacitive behaviour for high impedance organic coatings". In: *Progress in Organic Coatings* 77.12 (2014), pp. 2045–2053. ISSN: 03009440. DOI: [10.1016/j.porgcoat.2014.02.008](https://doi.org/10.1016/j.porgcoat.2014.02.008).
- [42] X. Yuan, Z. F. Yue, X. Chen, S. F. Wen, L. Li, and T. Feng. "EIS study of effective capacitance and water uptake behaviors of silicone-epoxy hybrid coatings on mild steel". In: *Progress in Organic Coatings* 86 (2015), pp. 41–48. ISSN: 03009440. DOI: [10.1016/j.porgcoat.2015.04.004](https://doi.org/10.1016/j.porgcoat.2015.04.004).
- [43] B. Hirschorn, M. E. Orazem, B. Tribollet, V. Vivier, I. Frateur, and M. Musiani. "Determination of effective capacitance and film thickness from constant-phase-element parameters". In: *Electrochimica Acta* 55.21 (2010), pp. 6218–6227. ISSN: 00134686. DOI: [10.1016/j.electacta.2009.10.065](https://doi.org/10.1016/j.electacta.2009.10.065).
- [44] E. van Westing, G. Ferrari, and J. de Wit. "The determination of coating performance with impedance measurements—II. Water uptake of coatings". In: *Corrosion Science* 36.6 (June 1994), pp. 957–977. ISSN: 0010938X. DOI: [10.1016/0010-938X\(94\)90197-X](https://doi.org/10.1016/0010-938X(94)90197-X).
- [45] C. Vosgien Lacombe, G. Bouvet, D. Trinh, S. Mallarino, and S. Touzain. "Water uptake in free films and coatings using the Brasher and Kingsbury equation: a possible explanation of the different values obtained by electrochemical Impedance spectroscopy and gravimetry". In: *Electrochimica Acta* 231 (2017), pp. 162–170. ISSN: 00134686. DOI: [10.1016/j.electacta.2017.02.051](https://doi.org/10.1016/j.electacta.2017.02.051).
- [46] V. N. Nguyen, F. X. Perrin, and J. L. Vernet. "Water permeability of organic/inorganic hybrid coatings prepared by sol-gel method: A comparison between gravimetric and capacitance measurements and evaluation of non-Fickian sorption models". In: *Corrosion Science* 47.2 (2005), pp. 397–412. ISSN: 0010938X. DOI: [10.1016/j.corsci.2004.06.028](https://doi.org/10.1016/j.corsci.2004.06.028).
- [47] D. Ciofini, J. Striova, M. Camaiti, and S. Siano. "Photo-oxidative kinetics of solvent and oil-based terpenoid varnishes". In: *Polymer Degradation and Stability* 123 (2016), pp. 47–61. ISSN: 01413910. DOI: [10.1016/j.polymdegradstab.2015.11.002](https://doi.org/10.1016/j.polymdegradstab.2015.11.002).
- [48] C. M. Popescu, C. Vasile, and B. C. Simionescu. *Spectral characterization of natural resins used in conservation*. 2012.
- [49] D. Pellegrini, C. Duce, I. Bonaduce, S. Biagi, L. Ghezzi, M. P. Colombini, M. R. Tinè, and E. Bramanti. "Fourier transform infrared spectroscopic study of rabbit glue/inorganic pigments mixtures in fresh and aged reference paint reconstructions". In: *Microchemical Journal* 124 (2016), pp. 31–35. ISSN: 0026265X. DOI: [10.1016/j.microc.2015.07.018](https://doi.org/10.1016/j.microc.2015.07.018).
- [50] K. Belbachir, R. Noreen, G. Gouspillou, and C. Petibois. "Collagen types analysis and differentiation by FTIR spectroscopy". In: *Analytical and Bioanalytical Chemistry* 395.3 (2009), pp. 829–837. ISSN: 16182642. DOI: [10.1007/s00216-009-3019-y](https://doi.org/10.1007/s00216-009-3019-y).

- [51] L. De Marco, W. Carpenter, H. Liu, R. Biswas, J. M. Bowman, and A. Tokmakoff. "Differences in the Vibrational Dynamics of H₂O and D₂O: Observation of Symmetric and Antisymmetric Stretching Vibrations in Heavy Water". In: *Journal of Physical Chemistry Letters* 7.10 (2016), pp. 1769–1774. ISSN: 19487185. DOI: [10.1021/acs.jpclett.6b00668](https://doi.org/10.1021/acs.jpclett.6b00668).
- [52] A. R. Berens and H. B. Hopfenberg. "Diffusion and relaxation in glassy polymer powders: 2. Separation of diffusion and relaxation parameters". In: *Polymer* 19.5 (1978), pp. 489–496. ISSN: 00323861. DOI: [10.1016/0032-3861\(78\)90269-0](https://doi.org/10.1016/0032-3861(78)90269-0).
- [53] D. Nguyen Dang, B. Peraudeau, S. Cohendoz, S. Mallarino, X. Feaugas, and S. Touzain. "Effect of mechanical stresses on epoxy coating ageing approached by Electrochemical Impedance Spectroscopy measurements". In: *Electrochimica Acta* 124 (2014), pp. 80–89. ISSN: 00134686. DOI: [10.1016/j.electacta.2013.08.111](https://doi.org/10.1016/j.electacta.2013.08.111).
- [54] K. J. van den Berg, A. Burnstock, M. de Keijzer, J. Krueger, T. Learner, A. Tagle de, and G. Heydenreich, eds. *Issues in Contemporary Oil Paint*. Cham: Springer International Publishing, 2014. ISBN: 978-3-319-10099-9. DOI: [10.1007/978-3-319-10100-2](https://doi.org/10.1007/978-3-319-10100-2).
- [55] L. Philippe, C. Sammon, S. B. Lyon, and J. Yarwood. "An FTIR/ATR in situ study of sorption and transport in corrosion protective organic coatings 1. Water sorption and the role of inhibitor anions". In: *Progress in Organic Coatings* 49.4 (2004), pp. 302–314. ISSN: 03009440. DOI: [10.1016/j.porgcoat.2003.07.002](https://doi.org/10.1016/j.porgcoat.2003.07.002).
- [56] C. Sammon, J. Yarwood, and N. Everall. "A FTIR-ATR study of liquid diffusion processes in PET films: Comparison of water with simple alcohols". In: *Polymer* 41.7 (2000), pp. 2521–2534. ISSN: 00323861. DOI: [10.1016/S0032-3861\(99\)00405-X](https://doi.org/10.1016/S0032-3861(99)00405-X).
- [57] C. M. Balik and J. R. Xu. "Simultaneous measurement of water diffusion, swelling, and calcium carbonate removal in a latex paint using FTIR-ATR". In: *Journal of Applied Polymer Science* 52.7 (1994), pp. 975–983. ISSN: 10974628. DOI: [10.1002/app.1994.070520716](https://doi.org/10.1002/app.1994.070520716).
- [58] J. R. Scully, D. C. Silverman, and M. W. Kendig, eds. *Electrochemical impedance: analysis and interpretation*. ASTM, 1993. ISBN: 0803118619.
- [59] F. Deflorian, L. Fedrizzi, S. Rossi, and P. Bonora. "Organic coating capacitance measurement by EIS: ideal and actual trends". In: *Electrochimica Acta* 44.24 (1999), pp. 4243–4249. ISSN: 00134686. DOI: [10.1016/S0013-4686\(99\)00139-5](https://doi.org/10.1016/S0013-4686(99)00139-5).